Numerical modeling of the evolution of stellar wind cavities and supernova remnants

AE van der Schyff

12834858

M.Sc.

Thesis submitted for the degree *Philosophiae Doctor* in Physics at the Potchefstroom Campus of the North-West University

Promoter:	Prof. S.E.S. Ferreira
Co-promoter:	Dr. R.D. Strauss

December 2016

NORTH-WEST UNIVERSITY
YUNIBESITI YA BOKONE-BOPHIRIMA
NOORDWES-UNIVERSITEIT

It all starts here ™

Numerical modeling of the evolution of stellar wind cavities and supernova remnants

Augusts E. van der Schyff M.Sc.

Dissertation submitted in fulfilment of the degree Philosophiae Doctor
in Physics at the North-West University

Supervisor : Prof. S.E.S. Ferreira
Co-Supervisor : Dr. R.D. Strauss
December 2016

Abstract

An astrosphere is a low density cavity that results from an outflowing supersonic wind. Of particular interest in this study is the effect of radiative cooling on the computed evolution of astrospheres created by O and B type stars. These stars are selected because their relatively large cavities results in effective radiative cooling. For this purpose, an existing hydrodynamic numerical model is adapted to include the effects of radiative cooling and magnetic pressure. Numerical calculations are performed, and the results from computations including radiative cooling and those without are compared throughout this work. Radiative cooling is found to have a significant impact on the evolution of astrospheres. It is found that the choice of a cooling function as a parameter in the model is not trivial and can impact the evolution of the computed astrosphere. The interstellar magnetic field is similarly found to be important and results in radiative cooling being less efficient if the magnetic pressure is comparable to the thermal pressure. Also shown is that relative motion results in a more bullet shaped cavity, and the inclusion of radiative cooling results in more compression at the bow shock than corresponding results without radiative cooling. It is also found that for stars with relative motion the magnetic pressure results in radiative cooling less efficient when this pressure is comparable to the thermal pressure. Supernova remnant evolution is also studied for a case with a pre-existing cavity and then compared to the supernova remnant evolution in a uniform and undisturbed interstellar medium. Radiative cooling is found to impact supernova remnant evolution at later stages of evolution. The supernova remnant evolution in a pre-exciting cavity is found to result in reflected and transmitted shocks when the forward shock of the supernova interacts with the outer structures of the pre-existing cavity. This is not the case for evolution in the undisturbed interstellar medium. Lastly, the transport of galactic cosmic rays into these simulated astrospheres is studied using a newly developed stochastic differential equation approach. Radiative cooling is assumed when the original cavity is computed and the modulation of these particles is studied. The effect on the modulation of cosmic rays is shown as this cavity expands into the interstellar medium. The transport of galactic cosmic rays in these simulated astrospheres is found to be dependent on the stellar mean free path, the energy of the particles and the shape of the cavity which can be influenced by radiative cooling.

Keywords: astrospheres, radiative cooling, ISM magnetic field, supernova remnant, galactic cosmic rays, stellar winds, stochastic differential equations.

Opsomming

ʼn Astrosfeer is ʼn lae digtheid holte wat bestaan as gevolg van ʼn uitvloei van ʼn supersoniese wind. Spesifiek van belang in hierdie studie is die effek van stralingsafkoeling op die berekende evolusie van astrosfere van O en B tipe sterre. Hierdie sterre is gekies omdat hulle relatiewe groot holtes effektiewe stralingsafkoeling veroorsaak. Ten doel word ʼn bestaande hidrodinamiese numeriese model aangepas om die effekte van stralingsafkoeling en magnetiese druk in te sluit. In hierdie werk word numeriese berekeninge uitgevoer en die resultate van die berekeninge met stralingsafkoeling word regdeur vergelyk met die resultate sonder dit. Dit is gevind dat stralingsafkoeling ʼn beduidende effek het op die evolusie van astrosfere. Dit is gevind dat die keuse van afkoelingsfunksie as ʼn veranderlike in die model nie triviaal is nie en dalk ʼn beduidende rol speel in die evolusie van berekende astrosfere. Die interstelêre magneetveld is soortgelyk gevind om belangrik te wees en veroorsaak ook dat stralingsafkoeling minder effektief is as die magnetiese druk vergelykbaar is met die termiese druk. Daar word ook gewys dat relatiewe beweging veroorsaak dat die holte ʼn meer koël vormige vorm het en die insluiting van stralingsafkoeling veroorsaak ʼn groter kompressie verhouding by die boog skok as die ooreenstemmende uitslae sonder stralingsafkoeling. Dit is weer gevind dat die magneetveld druk die stralingsafkoeling minder effektief maak wanneer hierdie druk vergelykbaar is met die termiese druk vir sterre met relatiewe beweging. Supernova oorblyfsel evolusie word ook bestudeer vir die geval met ʼn voorafbestaande holte en word dan vergelyk met die van supernova oorblyfsel evolusie in ʼn univorme onversteurde interstelêre medium. Dit is gevind dat stralingsafkoeling ʼn impak het op supernova oorblyfsel evolusie in die latere stadiums van evolusie. Vir supernova oorblyfsel evolusie in ʼn voorafbestaande holte die interaksie van die voorste skok met die buitenste strukture van die holte ʼn refleksie en oordraagbare skok veroorsaak. Dit vind nie plaas in die onversteurde interstelêre medium nie. Laastens word die transport van galaktiese kosmiese strale in hierdie gesimmileerde holtes word bestudeer met ʼn nuutontwikkelde stochasties differensiële vergelyking benadering. Stralingsafkoeling word aangeneem wanneer die oorspronklike holte bereken word en die modulasie op hierdie deeltjies word bestudeer. Die effek op die modulasie van kosmiese strale word gewys soos wat die holte uitsit in die interstelêre medium. Die transport van galaktiese kosmiese strale in hierdie gesimmuleerde astrosfere is gevind om afhanklik te wees van die vryeweglengte en die energie van die deeltjies. Dit is gevind dat die stralingsafkoeling die tydsafhanklikheid van die modulasie van galaktiese kosmiese strale beïnvloed.

Sleutelwoorde: astrosfere, stralingsafkoeling, ISM magneetveld, supernova oorblyfsel, galaktiese kosmiese strale, ster wind, stochastiese differensiële vergelyking.

List of Abbreviations

AP	Astropause
BS	Bow Shock
COAS	Cold Outer Astrosheath
CIE	Collisional Ionisation Equilibrium
Crs	Cosmic Rays
FS	Forward Shock
GCRs	Galactic Cosmic Rays
HP	Heliopause
HOAS	Hot Outer Astrosheath
IR	Infrared
IAS	Inner Astrosphere
ISM	Interstellar Medium
LISM	Local Interstellar Medium
OAS	Outer Astrosphere
pc	parsecs
RS	Reverse Shock
SW	Solar Wind
SL	Sonic Line
SDEs	Stochastic Differential Equations
SNR	Supernova Remnant
TS	Termination Shock
TP	Triple Point

The results from different cooling functions, are denoted as CF0 for no cooling, CF1 for cooling using the Mellema & Lundqvist (2002) cooling function, CF2 for cooling using the function from Schure et al. (2009), and CF3 for cooling using the expression of Siewert et al. (2004). Cosmic rays are referred to as CRs, supernova remnants as SNRs and the interstellar medium as the ISM.

Acknowledgements

I would like to express special appreciation and thanks to the following people:

My advisor, Prof. S.E.S. Ferreira, and my co-supervisor, Dr. R.D. Strauss.

Personnel at the School for Physics, in particular Mrs Petro Sieberhagen for administrative support, and Matthew Hollerman for IT support.

The NRF and the Centre for Space Research at the North-West University for financial support.

My parents for their love and support.

To Jeanie for showing me what is possible in life.

Contents

1 Introduction **3**

2 Astrospheric Cavities **7**

2.1 The Solar/Stellar Wind . . . 7

2.2 The Effect of the Solar and Interstellar Magnetic Field . . . 9

2.3 The Numerical Model . . . 10

2.4 Radiative Cooling of the Interstellar Medium . . . 12

2.4.1 Electron Impact Excitation of C^+ . . . 13

2.4.2 Cooling by Molecular Hydrogen . . . 14

2.5 Radiative Cooling Functions . . . 14

2.6 Shock Waves . . . 16

2.6.1 Rankine-Hugniot Relations in a Fixed Frame of Reference . . . 18

2.6.2 Radiative Shock Waves . . . 19

2.7 Comparison with Other Work . . . 20

3 Simulations of Astrospheres with Radiative Cooling **23**

3.1 Introduction . . . 23

3.2 The Effect of Radiative Cooling on a Hydrodynamic Computed Stellar Wind Cavity/Astrosphere . . . 23

3.2.1 The Effect of Different Cooling Functions on Hydrodynamical Simulations 24

3.2.2 The Effect of the ISM Density on Cavity Evolution . . . 27

3.3 The Effect of Ram Pressure on Cavity Evolution . . . 32

3.4 The Effect of Magnetic Field Pressure on Cavity Evolution . . . 34

3.5 Effect of the ISM Magnetic Field Pressure on Simulations . . . 34

3.6 The Effect of the ISM Density on Cavity Evolution, Including the Interstellar Magnetic Field . . . 35

3.7 Summary and Conclusions . . . 38

4 Astrospheric Evolution Including Relative Motion and Radiative Cooling 43

4.1 Introduction . . . 43

4.2 The Effect of Relative Motion on Cavity Evolution . . . 43

4.3 The Effect of Radiative Cooling in a Relative Motion Scenario . . . 46

4.4 The Effect of the Interstellar Magnetic Field . . . 49

4.5 Summary and Conclusions . . . 55

5 Supernova Remnant Evolution in Astrosphere/Stellar Wind Cavities 57

5.1 Introduction . . . 57

5.2 Supernova Evolution . . . 58

5.2.1 Ejecta Dominated Stage . . . 58

5.2.2 Sedov-Taylor Phase . . . 61

5.2.3 The Snowplow Phase . . . 62

5.3 The Effects of Radiative Cooling on SNR Evolution in an Undisturbed ISM . . . 63

5.4 SNR Evolution in a Pre-Existing Cavity with No ISM Magnetic Field or Relative Motion . . . 65

5.5 SNR Evolution in a Pre-Exiting Cavity with No ISM Magnetic Field or Relative Motion, but with Effects of Radiative Cooling Included . . . 72

5.6 The Effect of an ISM Magnetic Field on SNR Evolution . . . 77

5.7 Effect of the Relative Motion of a Pre-Existing Cavity on SNR Evolution . . . 82

5.8 The Effect of the Relative Motion of a Pre-Existing Cavity on SNR Evolution, Including an ISM Magnetic Field . . . 84

5.9 Summary and Conclusions . . . 85

6 The Modulation of Galactic Cosmic Rays in an Astrosphere 89

6.1 Introduction . . . 89

6.2 The Transport Equation . . . 91

6.3 Stochastic Differential Equations (SDEs) . . . 93

6.4 Diffusion Coefficients 94

6.5 Magnetic Field Dependence 95

6.6 The Effect of the ISM Diffusion Coefficient 97

6.7 The Effect of Varying the Stellar Diffusion Coefficient 97

6.8 Galactic CR Distribution Inside Astrospheres with Radiative Cooling 98

6.9 Energy Dependence of Galactic CRs in an Expanding Astrosphere 101

6.10 Time Dependence of Galactic CRs in an Expanding Astrosphere 104

6.11 Summary and Conclusions 104

7 Summary and Conclusions 107

Bibliography 111

Chapter 1

Introduction

By the early 1970s the hydrodynamic treatment of expanding astrospheres (stellar wind cavities) was well established (e.g. Parker, 1961, Axford et al., 1963, Holzer, 1972, Fahr & Neutsch, 1983). See also the review by Holzer & Axford (1970). More recently, the evolution of stellar winds are calculated in different works (e.g. Dwarkadas, 2007, Arthur, 2007, Preusse et al., 2007, Vidotto et al., 2010, Suzuki, 2011, Vidotto et al., 2011), but none as detailed as for our heliosphere (See e.g. Pauls & Zank, 1996, Scherer & Fahr, 2003, Ferreira & Scherer, 2004, 2006, Pogorelov et al., 2009a, Opher et al., 2011, 2015, for modelling efforts on the heliosphere).

In this work, numerical calculations are performed and the effects of radiative cooling on the evolution of such cavities and their structures are studied. Different in this work, compared to earlier efforts for the heliosphere (e.g. Fahr et al., 2000, Ferreira & Scherer, 2006, Ferreira & de Jager, 2008, Scherer et al., 2016), is that radiative cooling is to be included in the original model used by these authors. Radiative cooling is described in works by Falle (1975a), Weaver et al. (1977), Bertschinger (1986), and Dyson & Williams (1997). As these authors have shown, energy losses through an optically thin medium play an important role in astrophysical gas dynamics and should therefore be considered as a necessary element in numerical simulations. This is especially true for radiative shocks which arise in a wide variety of contexts. It is observed in nova and supernova explosions, bright filaments in old supernova remnants, and accretion flows in protostellar clouds.

The simplest form of radiative cooling is that of an optically thin medium. Here it is assumed that the gas in which the photons are emitted is completely optically thin, such that any photon that is emitted will simply leave the system rather than being absorbed elsewhere. This is a valid approach for astrophysical phenomena, which tend to have low to extremely low densities. This approach is different from the radiative transfer approach, where it is assumed that the gas is not optically thin. The photons emitted through radiative cooling in an optically thick medium are absorbed by the surrounding medium. This will lead to an increase in temperature, which in turn will change the sound speed as well as the shock structures (see e.g. Zel'dovich & Raizer, 1967, Fadeyev & Gillet, 2000).

In this work the effect that radiative cooling has on the evolution of young cavities resulting from stellar winds originating from a hot star (typical O and B type stars) are demonstrated. These stars are selected for this work because their cavities are in the order of a few parsecs (pc), resulting in effective cooling. The effect of radiative cooling on these cavities, their evolution and the resulting structure, is of importance and therefore comparisons between results with radiative cooling and corresponding results without radiative cooling are made. Also included in the model is an ISM magnetic field to study its effect on the evolution of the cavities and the effect of the interstellar medium (ISM) magnetic field on radiative cooling.

According to Toalá et al. (2016), many of these stars move through the ISM at relatively high velocities. Massive stars, with relative motion moving supersonically through the interstellar medium, produce large scale bow shocks. Many such shocks have been detected in optical, infrared (IR) and radio wavelengths. The effect of relative motion on cavity evolution are also included, together with radiative cooling and an ISM magnetic field.

After studying the effect that radiative cooling has on cavity evolution, the focus shifts to the influence that these pre-existing cavities have on supernova remnant (SNR) evolution. Massive stars, typically with mass $M \geq 8M_{\odot}$, end with a sudden release of energy that creates, for a moment, a very bright object in the sky that slowly fades after a couple of months and is known as a supernova. This creates an explosion that releases large amounts of kinetic energy in the form of a blast wave that moves through the interstellar medium (e.g. Franco et al., 1991, Dwarkadas, 2005). The impact of radiative cooling on Supernova Remnant evolution in a uniform, undisturbed ISM, a pre-existing cavity with radiative cooling, relative motion, and an ISM magnetic field are studied and results discussed.

Lastly, the transport of charged particles in an astrospheric cavity is studied. Cosmic rays (CRs) are considered fully ionized nuclei as well as anti-protons, electrons, and positrons that are accelerated by relativistic jets from active galactic nuclei, gamma ray bursts, blazars and supernova remnants (e.g. Bell, 2013, Blandford et al., 2014, Zhang & Li, 2016). Cosmic rays with kinetic energy from the GeV to the 100 TeV range are assumed to be mostly from galactic SNR origin (e.g. Blandford et al., 2014). The transport of these galactic cosmic rays in astrospheric cavities are calculated utilizing a stochastic differential equation (SDE) model (e.g. Yamada et al., 1998, Zhang, 1999, Pei et al., 2010, Strauss et al., 2011b, Kopp et al., 2012, Strauss et al., 2013, Luo et al., 2015, 2016).

The following abbreviations are used in this work: AP refers to the astropause, the bow shock is referred to as BS, the termination shock as TS, the inner astrosheath as the IAS, the outer astrosheath as OAS, the cold outer astrosheath as COAS, and the hot outer astrosheath HOAS. The results from different cooling functions, are denoted as CF0 for no cooling, CF1 for cooling using the Mellema & Lundqvist (2002) cooling function, CF2 for cooling using the function from Schure et al. (2009), and CF3 for cooling using the expression of Siewert et al. (2004). Cosmic rays are referred to as CRs, supernova remnants as SNRs and the interstellar medium as the ISM.

The structure of this thesis is as follows:

Chapter 2: This chapter contains some background on astrospheric cavities, using the heliosphere as an example as well as explaining the impact of the ISM magnetic field. Background is provided on radiative cooling mechanisms and the radiative cooling functions that are used in this work.

Chapter 3: In this chapter the effect that radiative cooling has on the evolution of young cavities resulting from stellar winds originating from a hot star (typical O and B type stars) is demonstrated. Astrospheric evolution is simulated using three different cooling functions from Schure et al. (2009), Siewert et al. (2004), and Mellema & Lundqvist (2002) to show the effect thereof on simulations. The direct comparison of the effects resulting from assuming different cooling functions has not been done before. These simulations are done for a strong ISM magnetic field and a weak ISM magnetic field, and also without a magnetic field, to illustrate the pure hydrodynamic case. For this purpose, the model developed by Fahr et al. (2000), Ferreira & Scherer (2006) and Ferreira & de Jager (2008) is used and adapted to include the effects of radiative cooling similar to Van Marle & Keppens (2011).

Chapter 4: In this chapter the study of astrospheric/stellar wind cavity evolution continues, using the same model as in the previous chapter. New in this chapter is that the effect of relative motion on the evolution of an astrosphere is simulated and results shown. This is done for a pure hydrodynamic case as well as when the ISM magnetic field is included. Again the effect of radiative cooling is included in the model and compared to no-cooling scenarios to illustrate the effect of this process on cavity evolution. Results are also compared to the previous chapter where relative motion was not included.

Chapter 5: The aim of this chapter is to present simulations of stellar wind cavities and SNR evolution in these cavities. The effect of a pre-existing cavity on SNR evolution, as well as SNR evolution inside a uniform ISM, is shown. The effect of including radiative cooling in the model is also investigated and its effect on calculations shown. The same numerical model, as discussed in the previous chapters, is used, including also the pressure of the magnetic field for certain simulations. The effect of relative motion on SNR evolution is also shown. An introduction to the necessary background regarding SNRs is provided in this chapter.

Chapter 6: The modulation of galactic cosmic rays in a stellar wind cavity is investigated in this chapter. For the first time a 1 dimensional version of the transport equation is solved numerically to study the transport of galactic CRs in an astrosphere. The model as used in the previous chapters is used to calculate the cavity in which the particles are transported. Afterwards, a transport model (e.g. Strauss et al., 2011a) is used to calculate CR modulation. The impact of radiative cooling, implemented during cavity evolution, on the transport of galactic cosmic rays is shown. An introduction to the necessary transport theory of cosmic rays is provided in this chapter.

Parts of this work is published in Scherer et al. (2015).

Chapter 2

Astrospheric Cavities

This chapter will introduce the reader to stellar wind cavities, or astrospheres, as they are sometimes called. An example of a thoroughly studied astrosphere, namely the heliospheric structure, is briefly discussed in this chapter. Important features such as the solar/stellar wind, the termination shock, the inner heliosphere/astrosphere, the heliopause/astropause, and the bow shock are discussed. For a thorough review see e.g. Zank et al. (2009). Some of these structures are also discussed in more detail in subsequent chapters. The effect of the interstellar magnetic field on the evolution of cavities is also discussed to show the importance of the magnetic pressure on the evolution of these cavities. Furthermore, the numerical method and the underlying assumptions made in the model, as well as the parameters used in this study, are discussed.

In this work the model of Fahr et al. (2000), Ferreira & Scherer (2004) and Ferreira & de Jager (2008) is used to simulate the astrospheric structure. Because of the importance of radiative cooling, a brief introduction into radiative cooling and the different cooling functions used in this study, is provided. Although not important for the heliosphere, this process does impact the evolution of larger astrospheres expanding in an ISM (e.g. Koo & McKee, 1992). Apart from calculating astrospheric evolution, this model is used in the calculation of supernova remnant (SNR) evolution in Chapter 5. The background regarding SNRs is provided in that chapter. Also studied in this work is cosmic ray propagation in such an astrosphere. This is done in the last chapter and a newly developed stochastic differential equations (SDEs) transport code is used for that purpose. The necessary background on that topic is also provided in that chapter.

2.1 The Solar/Stellar Wind

For the solar corona of the Sun, or the atmosphere of any star, to remain in hydrodynamic equilibrium there has to be a continual expansion of this atmosphere into interstellar space (Parker, 1958). This expansion results in an outflowing wind, and for the Sun this wind has a speed of roughly 400 km s^{-1} in the equatorial regions. This wind has a latitudinal dependence at solar minimum conditions that increases the speed of the wind to 800 km s^{-1} at the poles (e.g. Marsden et al., 1996). The temperature of the outflow is $\sim 10^4$ K (e.g. Zank et al., 2009), but is also dependent on radial distance (e.g. Richardson & Smith, 2003).

Outflow velocities for O and B type stars are in the range of $170 - 3000$ km s^{-1} (e.g. Crowther, 2001) and mass loss rates of $10^{-8} - 10^{-5}$ M$_\odot$ yr^{-1} (see e.g. Crowther, 2001, Shepherd, 2005). These stars are selected for this work because their cavities are in the order of a few pc, resulting in effective cooling. Mass loss rates for O type stars have been reported to be $2.4\times10^{-6}\mathrm{M}_\odot$ yr^{-1}, with outflow velocities of 2250 km s^{-1}. While some stars have been reported with mass loss rates of $1.6 \times 10^{-9}\mathrm{M}_\odot$ yr^{-1} and outflow velocities of 1500 km s^{-1}. See Toalá et al. (2016) and references therein.

The region that is formed as a result of the interaction of the stellar wind or solar wind with the local interstellar medium (LISM) is referred to as the heliosphere or an astrosphere. A representation of the heliosphere is given in Figure 2.1 (here the Sun remains fixed at the origin and the LISM moves from left to right). Due to the relative motion of the Sun with regards to LISM, the heliosphere has a distinctive asymmetrical or bullet shape. This results in the nose being more compressed resulting in a higher density while the tail region is elongated.

Following the out-blowing wind in Figure 2.1, one notes that the solar wind eventually results in a termination shock (TS). The TS forms when the pressure of the stellar wind balances the pressure of the LISM. The TS results in a sudden increase in density and the solar wind is also decelerated to subsonic velocities and its kinetic energy is converted to thermal energy (e.g. Richardson et al., 2008).

As shown in Figure 2.1, the region after the TS where the solar wind kinetic energy has been converted to thermal energy, is known as the inner heliosphere and has an effective temperature of $\approx 10^6$ K (Zank et al., 2009). This region has a much lower velocity after the shock , ≈ 100 km s^{-1} and decreases up to the boundary. The wind in this region is also much hotter as a result of the TS. The region that separates the inner heliosphere from the LISM is known as the heliopause (HP). The HP contains the solar plasma and separates it from the LISM. For pure hydrodynamics, the HP is a contact discontinuity, meaning that there is no particle transport across the HP and the thermal pressure is conserved across the HP.

The expansion of the solar wind cavity into the LISM, as well as the movement of the LISM assuming this process is supersonic, creates a bow shock (BS). The BS will shock the LISM, and like the TS for the solar wind (SW), will result in the LISM becoming subsonic. Again, the kinetic energy of the LISM is converted into thermal energy and causes the shocked LISM to have a larger temperature than the unshocked or upstream LISM. The region between the TS and the HP is defined as the inner heliosheath, while the region between the HP and the BS is defined as the outer heliosheath (Nickeler et al., 2006). Note that for the heliosphere, the bow shock might be rather a bow wave, because of a slower speed through the ISM than previously thought (McComas et al., 2012). For the astrospheric case these structures will be referred to as the inner astrosphere (IAS), the astropause (AP) and the outer astrosphere (OAS).

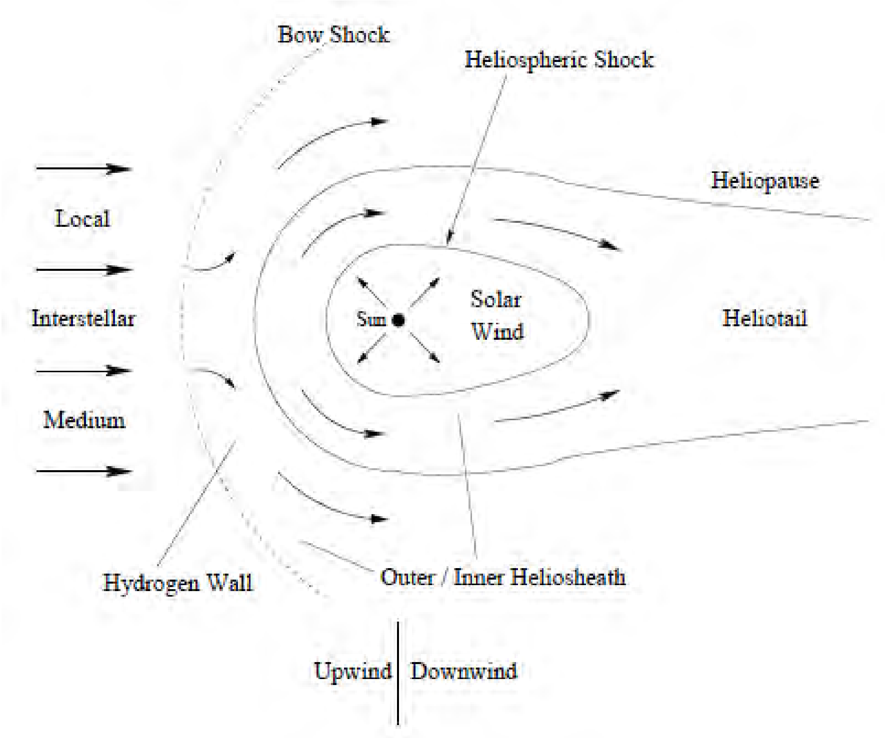

Figure 2.1: A representation of the heliosphere in the rest frame of the Sun (from Nickeler et al., 2006).

The solar wind and the heliospheric bubble as shown in Figure 2.1 is in reality not as simple as described above. Firstly, the velocity of the solar wind is not uniform everywhere, but is influenced by the solar magnetic field close to the Sun which, during solar minimum conditions, develops polar coronal holes at high latitudes that will increase the solar wind at these latitudes (e.g. Marsden et al., 1996). This latitudinal dependence results in a heliospheric elongation towards the poles (e.g. Zank & Pauls, 1996, Scherer & Ferreira, 2005). However, due to a lack of detailed knowledge about stellar wind outflows, it is assumed in this work that the outflow is uniform over all latitudes and does not change over a stellar cycle.

2.2 The Effect of the Solar and Interstellar Magnetic Field

The importance of the solar magnetic field was recently highlighted in Opher et al. (2015), who proposed the existence of heliospheric jets downstream of the TS as shown in Figure 2.2. The authors perform 3D MHD simulations and assume that the solar magnetic field is unipolar while also neglecting the LISM magnetic field to avoid artificial numerical magnetic reconnection. These authors argue, that the magnetic tension force is strong enough to collimate the wind. Meaning that the lobes survive due to the resistance of the solar magnetic field to being stretched. The heliosphere jets are deflected into the tail region by the motion of the Sun trough the LISM.

The effect of the interstellar magnetic field on the heliosphere is also discussed in e.g. Pogorelov

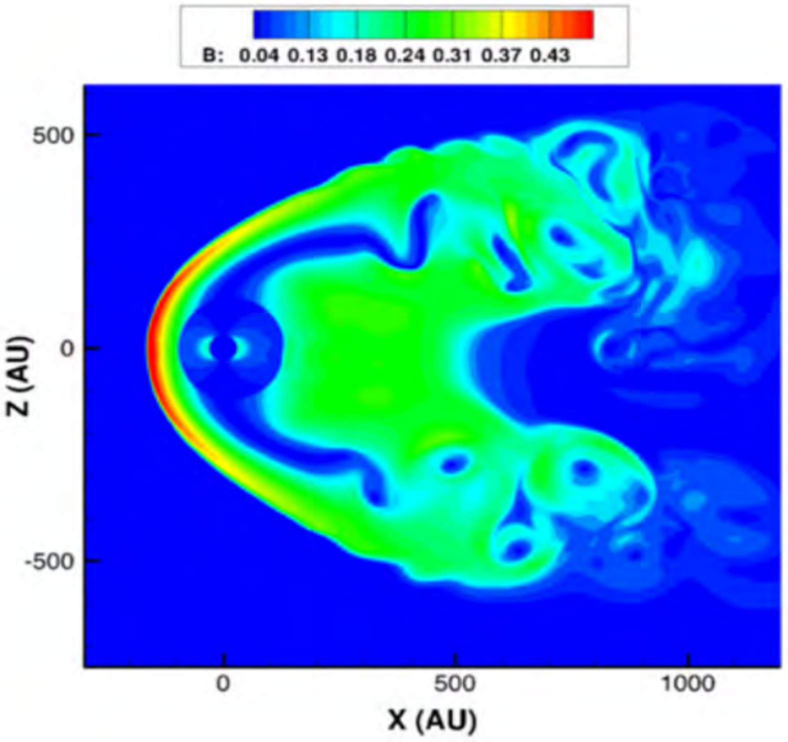

Figure 2.2: Contour plots of the magnetic field showing the two-lobe structure caused by the solar magnetic field. No ISM magnetic field is taken into account for these simulations. Taken from Opher et al. (2015).

et al. (2009b) and Zank et al. (2009). It is found that the LISM magnetic field effects the shape and the position of the HP relative to the Sun. This in turn affects the shape and the symmetry of the TS. However, the inclusion of neutral H in the model reduces this calculated asymmetry.

Figure 2.3 (taken from Pogorelov et al., 2008), shows the asymmetry of the heliosphere when the LISM wind and the LISM magnetic field vector are directed in the southern hemisphere at an angle of 30° to the ecliptic plane with the introduction of neutrals. The LISM magnetic field was taken as 3 μG. This asymmetry is found to be enhanced when neutrals were not included. Altough the magnetic pressure is taken into account in this model, these asymmetries are not studied because of the limitations of a 2D spatial model.

2.3 The Numerical Model

In this work the well known MHD equations (Landau & Lifshitz, 1984)

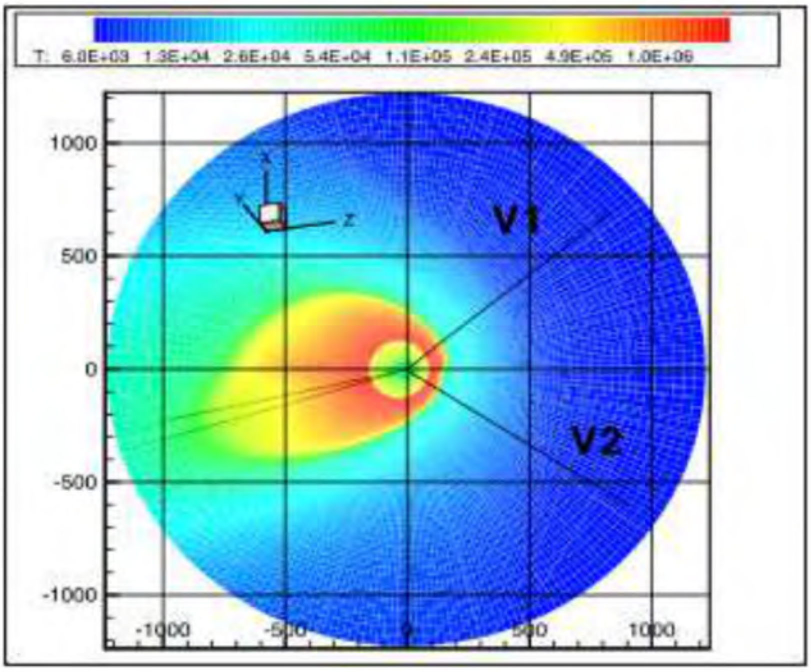

Figure 2.3: Contour plots of the plasma temperature in the V1 (Voyager 1) and V2 (Voyager 2) plane. Taken from Pogorelov et al. (2008).

$$\frac{\partial \rho}{\partial t} + \nabla \cdot (\rho \mathbf{v}) = 0 \tag{2.1}$$

$$\frac{\partial (\rho \mathbf{v})}{\partial t} + \nabla \cdot \left(\rho \mathbf{v} \otimes \mathbf{v} + P^* \mathbf{I} - \frac{1}{4\pi} \mathbf{B} \otimes \mathbf{B} \right) = 0 \tag{2.2}$$

$$\frac{\partial e}{\partial t} + \nabla \cdot \left[(e + P^*) \mathbf{v} - \frac{1}{4\pi} \mathbf{B}(\mathbf{B} \cdot \mathbf{v}) \right] = -n_e n_H \Lambda(T) \tag{2.3}$$

$$\frac{\partial \mathbf{B}}{\partial t} + \nabla \times (\mathbf{B} \times \mathbf{v}) = 0 \tag{2.4}$$

$$\nabla \cdot \mathbf{B} = 0 \tag{2.5}$$

are solved, which describe inviscid flow to calculate astrosphere cavities and supernova remnant evolution. Here ρ is the density, $\mathbf{v}$ the velocity, P the gas pressure, $\mathbf{B}$ is the magnetic field, $P^* = P + \mathbf{B}^2/8\pi$, $\mathbf{I}$ is the unit matrix, and $\otimes$ is the dyadic product. The total energy is given as

$$e = \frac{\rho |\mathbf{v}|^2}{2} + \frac{P}{\gamma - 1} + \frac{\mathbf{B}^2}{8\pi}. \tag{2.6}$$

These equations describe the balance of mass, momentum, energy and induction. Currently, only a one fluid scenario is considered with an adiabatic index of $\gamma = 5/3$. The model is also limited to 2D instead of 3D, to be able to compute evolution over long time scales with limited computational resources. The numerical scheme for the fluid part is discussed in LeVeque (2002) and computes solutions to hyperbolic differential equations using a wave propagation approach. See also Fahr et al. (2000), Ferreira & Scherer (2004), and Ferreira & de Jager (2008) for more details. For the induction equation, the scheme presented by Pen et al. (2003) is used to account for the divergence free requirement of the magnetic field.

Radiative cooling is taken into account in the energy equation with the term $-n_e n_H \Lambda(T)$, where n_e and n_H represent the electron and proton number densities, respectively. This approach is similar to Van Marle & Keppens (2011). The cooling efficiency is represented by the function $\Lambda(T)$ and is discussed below.

For boundary conditions it is noted that the evolution of a star depends on its initial mass, whether it's a solar-like star (with mass $\sim 1\mathrm{M}_{\odot}$) or a massive star with a mass in excess of 20 $\mathrm{M}_{\odot}$. Different mass corresponds to different mass-loss rates (densities) and different outflow speeds, resulting in different sizes of cavities. Furthermore, these boundary conditions also change over time (e.g. Mackey et al., 2014). Dynamic changes in the outflow boundary conditions in this model are not yet implemented. Such changes in the mass-loss rate and outflow speed over time result in different computed cavity geometries and densities as those presented in this work. For this work, the only interest is the geometrical extent of these cavities to illustrate, to the first order, the effect of different cooling functions on computations.

Furthermore, only considered is a fully developed stellar wind, which means the integration boundary is far beyond all critical points of the stellar wind evolution (e.g. Lamers & Cassinelli, 1999). Which in turn, mean that the supersonic stellar wind is no longer accelerated and expands spherically.

2.4 Radiative Cooling of the Interstellar Medium

Radiative cooling of the ISM is thoroughly discussed in e.g. Schwarz et al. (1972), Falle (1975a), Stevens et al. (1992), Frank et al. (1992), Mackey et al. (2013, 2014). Below follows a short summary taken from Dalgarno & McCray (1972) and Dyson & Williams (1997).

A heated partially ionized gas cools through the emission of radiation. During this process the thermal kinetic energy of the gas is converted to radiation by collisional processes. The efficiency of the cooling is a sensitive function of the composition of the gas (Dalgarno & McCray, 1972).

The collision results in the excitation of an atom, ion or molecule. After a time, the excited system will radiate the gained energy away through a photon which, depending on the opacity of the environment, will escape from the environment. This process is described by Dyson & Williams (1997) as

$$A + B \rightarrow A + B^{*} \tag{2.7}$$

where A collides with B resulting in it being excited. The emission of a photon then results as

$$B^* \rightarrow B + h\nu. \tag{2.8}$$

According to Dyson & Williams (1997), the most efficient cooling processes are likely described by the following criteria:

(i) Frequent collisions which implies a high abundance of the colliding pairs.
(ii) The excitation energy must be comparable or less then the thermal kinetic energy.
(iii) There must be a probability of excitation during a collision.
(iv) The photon is normally emitted before a second collision occurs with the excited partner.
(v) The photons emitted are not re-absorbed, meaning that the gas is optically thin so that the photons can escape the environment.

2.4.1 Electron Impact Excitation of C^+

At low temperatures the fine structure excitation of C^+ contributes the most to the cooling and C^+ is the most abundant form of carbon for many regions (e.g. Dalgarno & McCray, 1972). The excitation of C^+ after the collision with an electron is given as

$$e + C^+(^2P_{1/2}) \rightarrow e + C^+(^2P_{3/2}). \tag{2.9}$$

This transition has an energy difference of $\Delta E = 1.3 \times 10^{-14}$ erg $\propto 92$ K and can also result from the collision with H and H_2. This kinetic temperature corresponds closely with the kinetic temperature of many low density clouds of 100 K, and therefore ensures efficient cooling.

A small contribution to the cooling comes from the fine structure transitions that result from the collision between an electron and neutral O. The reaction is

$$e + O(^3P_2) \rightarrow e + O(^3P_{1,0}) \tag{2.10}$$

with a difference in energy of 228 K and 326 K. This reaction can also take place with the collision of H and H_2.

The reaction of Si^+ is also significant at low temperatures with the reaction

$$e + Si^+(^2P_{1/2}) \rightarrow e + Si^+(^2P_{3/2}), \tag{2.11}$$

with an energy difference of $\Delta E = 5.7 \times 10^{-14}$ erg $= 413$ K. Further increases in temperature result in the fine structure of Si^+ and Fe^+ to be more efficient than that of C^+. Above 600 K metastable excitations of Fe^+ are more effective, while above 6000 K metastable excitation of O, N, C^+, Si^+, and S^+ are all effective in cooling.

At temperatures of 10 500 K, the excitation of atomic hydrogen takes place. Hydrogen, being the most abundant element, will completely dominate the cooling above 10 500 K.

At still larger temperatures, the excitation of the already excited levels of atomic hydrogen will become unimportant. The neutral hydrogen disappears, and excitations to metastable and allowed levels of various ionization states of such elements as He, C, O, N, Ne, Si, Fe and Mg that will control the thermal balance over a wide temperature range up to $\approx 10^7$ K take place.

2.4.2 Cooling by Molecular Hydrogen

Since molecular hydrogen is very abundant in the universe it can be effective in cooling the interstellar medium. This is done through the introduction of rotational excitation processes. For molecular hydrogen, the only rotational transitions allowed are $\Delta J = \pm 2$. The transition from $J = 0$ to $J = 2$ takes place at an energy of 510 K. However, the radiation lifetimes are large with 3×10^{10} s for $J = 0$ and 2.1×10^9 s for $J = 3$ (Dalgarno & McCray, 1972, Dyson & Williams, 1997).

This means that the rotational distribution of molecular hydrogen is at thermal equilibrium with a characteristic temperature. The cooling rate is dependent on the particle density. The radiation will leak out slowly from the distribution and will result in only minor perturbations to the populations. This radiation is very unlikely to be re-absorbed by molecular hydrogen elsewhere in the cloud.

Radiative cooling is taken into account in the energy equation of Equation 2.5 with the term $-n_e n_H \Lambda(T)$, where n_e and n_H represent the electron and proton number density, respectively. This approach is similar to Van Marle & Keppens (2011). The cooling efficiency is represented by the function $\Lambda(T)$ and is discussed below.

2.5 Radiative Cooling Functions

In this work, the cooling functions to be used in this model, is shown in Figure 2.4, and are taken from Mellema & Lundqvist (2002) (dashed line), Schure et al. (2009) (dot-dashed line), as well as Siewert et al. (2004) (dot-dot-dot-dashed line). In the next chapter these will be used to illustrate the effect of different cooling efficiencies on cavity evolution. Mellema & Lundqvist (2002) and Schure et al. (2009) assume solar abundances whereas Siewert et al. (2004) use the cooling functions from Dalgarno & McCray (1972). Other cooling functions can be found in Sutherland & Dopita (1993) and Gnat & Sternberg (2007).

Collisional ionisation equilibrium (CIE) is assumed for all functions. CIE assumes that the plasma is in a steady state and that collisional ionization, charge exchange, radiative recombination, and dielectrical recombination are the only processes altering the ionization balance.

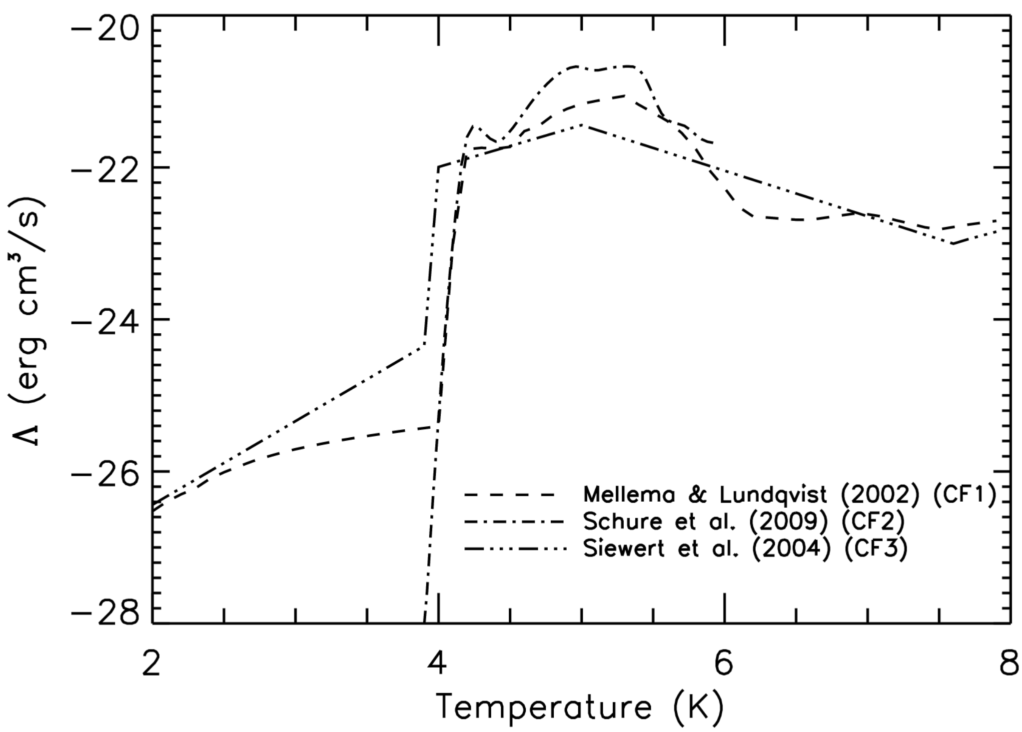

Figure 2.4: Cooling efficiencies, as a function of temperature, that is used in this work. Both axis are on a base-10 logarithmic scale.

This would result in the ionization fractions for each element to depend only on the gas temperature, and to have no dependence on the gas density (e.g. Draine, 2011).

At temperatures above 10^4 K the ionization of hydrogen provides enough free electrons so that collisional excitation of atoms or ions is dominated by electron collisions. However, at low densities every collisional excitation is followed by radiative decay. This results in the cooling function becoming a function of temperature and of the elemental abundances relative to hydrogen.

CIE is a valid assumption if the plasma is optically thin and dominated by collisional processes with cooling timescales that are larger than either the ionisation or recombination timescales. Deviation from CIE can result from additional photo-ionisation, or if non-CIE takes place, i.e. the recombination or ionisation timescales are larger than the cooling or heating timescales. If photo-ionisation takes place, or if the cooling timescale is shorter than the recombination timescale, the cooled plasma will be over ionised (Draine, 2011). The cooling functions used here do not include photo-ionisation.

The cooling rate below $T = 10^4$ K for the cooling curve of Mellema & Lundqvist (2002) is entirely due to CII, since this ion is assumed to never recombine. The cooling curve taken from Schure et al. (2009) is adapted to the X-ray regime, and includes continuum emission, but not line emission for wavelengths more than 2000 Å. This implies that the cooling for temperatures below $T = 10^{4.86}$ K is underestimated.

The elements taken into account by Schure et al. (2009) for low temperature cooling ($< T = 10^4$ K) are O, C, N, Si, Fe, Ne, and S. These cooling efficiencies are calculated by Dalgarno & McCray (1972). The cooling is partially caused by the excitation of singly charged ions with thermal electrons. For low fractional ionisation, collisions with neutral H can substantially contribute to the cooling.

Mellema & Lundqvist (2002) include all ions for H, He, C, N, O, and Ne. Collisional excitation states for higher excitation ionisation states are taken from Gaetz & Salpeter (1983). No element heavier than Ne is taken into account. Cooling resulting from collisional ionisation is not taken into account, and causes cooling for low shock velocities to be underestimated. At higher temperatures the elements included become completely ionized, this could result in heavier elements contributing to the cooling. Therefore the cooling is underestimated in the temperature range of $T = 10^6 - 10^{6.8}$ K, after which free-free interaction will start to dominate. Free-free emission and free-bound emission cooling is included and yields cooling efficiencies up to $T = 10^9$ K (see Gronenschild & Mewe, 1978, Gaetz & Salpeter, 1983).

2.6 Shock Waves

When the velocity of a fluid becomes comparable with or exceeds the speed of sound in that medium, effects due to the compressibility of the fluid become important. Perturbations or information in gasses are transmitted through pressure waves that move at the speed of sound. The flow of gas depends very much on whether it is subsonic or supersonic. Subsonic refers to velocities that are less than the speed of sound, while supersonic refers to velocities larger than the speed of sound. If the flow is supersonic it will result in a shock wave or a compression wave.

The following section is taken from Dyson & Williams (1997). The thickness of a shock is in the order of the mean free path of the particles involved, and can therefore be regarded as a discontinuity. Since the shock can be regarded as a discontinuity, the flow through it is said to be time independent, and the relationship between the fluid on either side of this discontinuity can also be regarded as time independent. A reference frame in which the shock is stationary can then be used to describe the flow on either side of the shock. A description on either side of the shock is given by the Rankine-Hugoniot conditions.

The shock is schematically shown in Figure 2.5 in the rest frame of the shock. A gas with pressure P_0, density ρ_0, and velocity u_0 relative to the shock enters the shock from the right, or upstream region. It emerges from the shock, or downstream of the shock, at pressure P_1, density ρ_1, and velocity u_1. The Rankine-Hugoniot conditions for a fluid with an adiabatic exponent of 5/3 then result in the velocity ratio

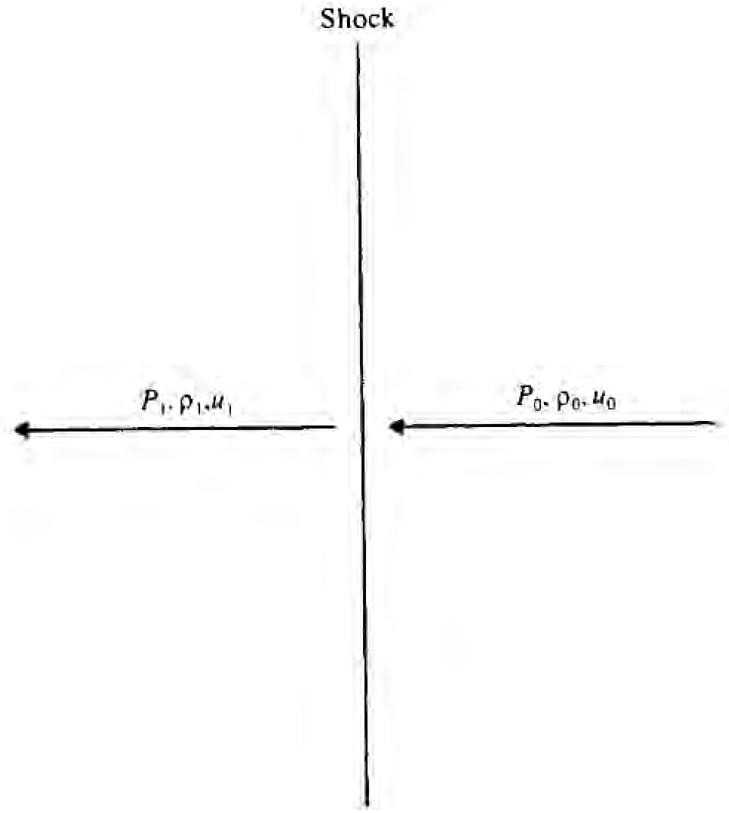

Figure 2.5: Flow variables on either side of the shock. The velocities are given in the rest frame of the shock (taken from Dyson & Williams, 1997).

$$\frac{u_1}{u_0} = \frac{1}{4} \tag{2.12}$$

for a strong shock or large Mach number. The density ratio is

$$\frac{\rho_1}{\rho_0} = \frac{4}{1}. \tag{2.13}$$

The compression is limited to this value, regardless of how large the Mach numbers are, since the change in the kinetic energy goes entirely into the translational energy of the shocked particles, thereby increasing the pressure. This increase in pressure will oppose the compression.

Since the shock is strong (the Mach number is much larger than unity), the pressure ahead of the shock is negligible, and the pressure change across the shock is extremely large. The pressure of the shocked gas is then

$$P_1 = \frac{3}{4}\rho_0 u_0^2. \tag{2.14}$$

Since the gas is a perfect gas it obeys the equation of state

$$P = \frac{\rho k T}{\mu m} \tag{2.15}$$

where μ is the mean molecular weight and m is the particle mass. The shocked temperature is then found as

$$T_1 = \frac{3}{16}\frac{\mu m}{k}u_0^2. \tag{2.16}$$

2.6.1 Rankine-Hugniot Relations in a Fixed Frame of Reference

Until now the results are shown for a reference frame in which the shock is stationary. It is however, often required to give the Rankine-Hugniot relation in a fixed frame of reference, meaning one in which the shock is moving.

The shock is now assumed to move at a velocity of V_s in the fixed frame and let v_0 and v_1 be the velocities upstream and downstream of the shock, respectively, also in a fixed frame. The transformation is now affected by the relative velocity

$$u_0 = v_0 - V_s \tag{2.17}$$

and

$$u_1 = v_1 - V_s. \tag{2.18}$$

The density relation remains unaffected by the change of reference frame. The downstream velocity can now be written as

$$v_1 = \frac{3}{4}V_s. \tag{2.19}$$

This means that the gas behind the shock moves in the same direction as the shock but at three-quarters of the shock speed. The pressure and temperature relations can now be written as

$$P_1 = \frac{3}{4}\rho_0 V_s^2 \tag{2.20}$$

and

$$T_1 = \frac{3\mu m}{16k}V_s^2. \tag{2.21}$$

This shows that the temperature of the shocked gas is highly dependent on the shock velocity, and it is this temperature that will determine the processes at which the shocked gas will radiate. Equation 2.21 is used in subsequent chapters to explain certain findings.

2.6.2 Radiative Shock Waves

When gas goes through a shock it is heated as described by Equation 2.16. Generally, heated gasses radiate and the radiation removes thermal energy from the gas. It is assumed in this work that the post-shock temperatures are high enough to fully ionize the gas. When fully ionized, the shocked gas cools rapidly, if at a high temperature (e.g. Bertschinger, 1986) and is believed to be important in a variety of systems (e.g. Mignone, 2005). The temperature, T_1, after the gas has passed through the shock is given by Equation 2.21, and is dependent on the velocity of the shock, V_s, and the molecular weight, μ. It is this post shock temperature that will determine the physical mechanism at which the gas will radiate, since CIE is assumed.

In this work, the gas is assumed to be completely ionized, both upstream and downstream of the shock, or that the shock speed is high enough that ionization can result from the post-shock temperatures. The post-shock gas consists of a variety of ions, and will radiate through a variety of processes. Since collisional times between particles in the gas are very short compared to the timescales to lose significant thermal energy through radiation, removing energy from one component of the gas is equivalent to cooling the gas as a whole (Dyson & Williams, 1997).

Hydrogen is ionized at 10 500 K and requires a shock velocity of $V_s \gtrsim 50$ km s^{-1}. Shocks with velocities of $\approx 80-2700$ km s^{-1} are common in astrophysical environments (Dyson & Williams, 1997) and therefore implies that the cooling of hydrogen is highly probable. The cooling rate decreases as the temperature increases and is a result of there being fewer ions available for cooling as the temperature increases; this describes what is known as the thermal instability.

The shocked gas moves a distance, L_c, which is the distance that the shocked gas moves before radiating away the thermal energy it gained passing through the shock. This distance is known as the cooling length. Therefore, a radiative shock that has been compressed from equilibrium will find that the incoming shocked gas has not had sufficient time to cool before reaching the back of the shortened cooling region ($< L_c$). Thus the system has too much post-shock thermal energy. At every point where the temperature is higher than the steady state temperature (everywhere in the post-shock region), the pressure is higher as well. This over-pressure drives the shock front forward, expanding the cooling region toward its equilibrium state. Similarly, if the radiative shock is stretched from equilibrium, the post-shock gas will cool before it reaches the back of the cooling region. Therefore, the system will be under pressured with respect to equilibrium, and the shock front will be driven backward towards its steady state position by the ram pressure of the incoming gas (Strickland & Blondin, 1995).

The stability of radiative shocks is analysed in Field (1965), Langer et al. (1981), Chevalier & Imamura (1982) and Imamura (1985). The isobaric condition for the thermal instability is given as (e.g. Schwarz et al., 1972, Sutherland & Dopita, 1993, Sutherland et al., 2003)

$$\frac{dln\Lambda}{dlnT} < 2 \tag{2.22}$$

and is satisfied for a wide range of temperatures for the cooling functions in Figure 2.4, and implies that the radiative cooling instability can be expected to be found in this work under certain conditions.

2.7 Comparison with Other Work

The density profile for a star with an outflow velocity of 1500 km s^{-1}, mass loss rate of $10^{-6}\mathrm{M}_{\odot}$ yr^{-1}, ISM density of $10^{-22.5}$ g cm^{-3} and an ISM temperature of 100 K as simulated by Van Marle & Keppens (2011) is shown in Figure 2.6 (from Van Marle & Keppens, 2011). No relative motion is assumed and magnetic fields are neglected. Radiative cooling is implemented using the cooling function from Mellema & Lundqvist (2002) (shown in Figure 2.4) and adaptive mash refinement is implemented. Here is a typical profile of a cavity showing the low density supersonic outflow, a termination shock and incompressible subsonic flow up to the astropause. As shown by Van Marle & Keppens (2011), radiative cooling is shown to be important at the bow shock, and that high grid resolution is necessary to resolve the fine structure created when implementing radiative cooling. For the highest resolution computations (shown with a dashed line in Figure 2.6), the density of the outer astrosphere reached values of $\sim 10^{-21}$ g cm^{-3}. This results in a compression ratio that is larger than the expected value of 4, and is a direct result of radiative cooling.

The resulting computations from this work with similar parameters used as in Van Marle & Keppens (2011) is shown in Figure 2.7. Here the solid line shows the result with radiative cooling included and the dashed line shows the result with radiative cooling excluded. The positions of the TS, AP and BS are shown for the no-cooling results. The position of the termination shock, astropause, bow shock and outer astrosphere density are in good agreement with those of Van Marle & Keppens (2011) for the result with radiative cooling included (solid line). Note that the position of the TS, AP and BS is different from the no-cooling result. Also different between the result with radiative cooling and the result without, is the compression ratio at the BS. Figure 2.7 is studied in the next chapter where detailed discussions between cooling and no-cooling scenarios are given.

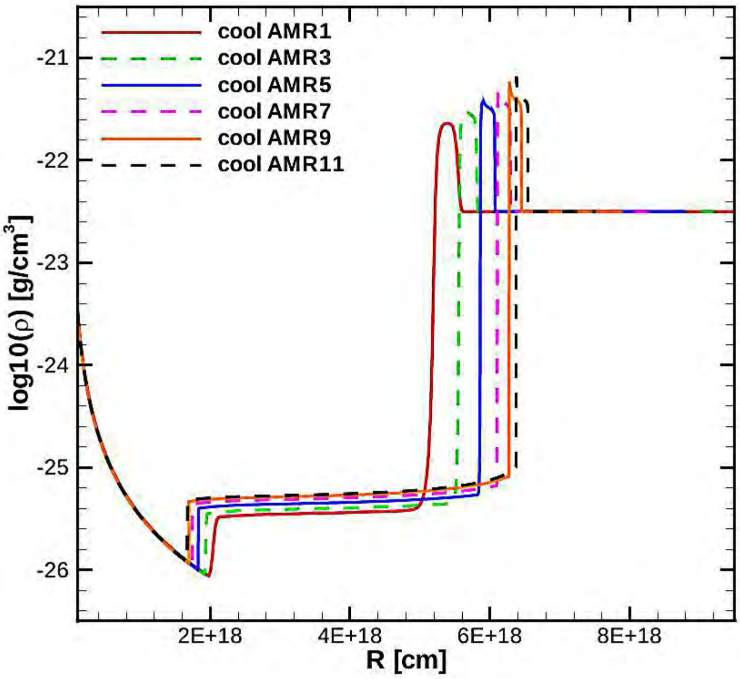

Figure 2.6: Density profiles taken from Van Marle & Keppens (2011) at ≈ 40 kyrs. The different lines correspond to different levels of adaptive mesh refinement.

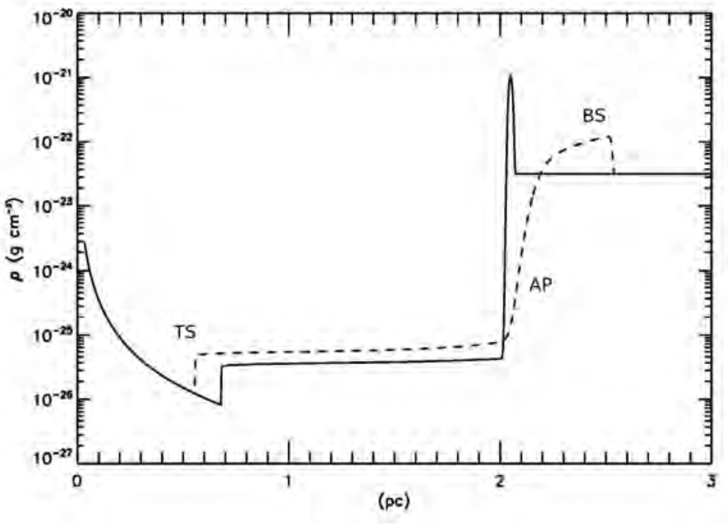

Figure 2.7: Density profile found in this work at 40 kyrs for similar parameters as used in Van Marle & Keppens (2011). The solid line shows the result with radiative cooling while the dashed line shows the result without radiative cooling. The TS, AP, BS is indicated for the no-cooling result.

Chapter 3

Simulations of Astrospheres with Radiative Cooling

3.1 Introduction

As mentioned in the previous chapter, a supersonic stellar wind results in a blown out astrosphere/cavity inside the ISM consisting of four basic structures namely, the unshocked stellar wind, the shocked stellar wind or inner astrosheath (IAS), the outer atrosheath (OAS), and the undisturbed ISM. Each region is separated by discontinuities such as the termination shock, astropause and the bow shock.

In this chapter the effect that radiative cooling has on the evolution of young cavities resulting from stellar winds originating from a hot star (typical O and B type stars) is demonstrated. Astrospheric evolution is simulated using three different cooling functions to show the effect thereof on simulations. The direct comparison of the effects resulting from assuming different cooling functions has not been done before. These simulations are done for a strong ISM field and a weak ISM field, and also without a magnetic field to illustrate the pure hydrodynamic case. The different cooling functions from Schure et al. (2009), Siewert et al. (2004), and Mellema & Lundqvist (2002), as shown in Figure 2.4 in the previous chapter, are used, and the effect of these cooling functions on the cavity structure is presented.

3.2 The Effect of Radiative Cooling on a Hydrodynamic Computed Stellar Wind Cavity/Astrosphere

In this chapter it is assumed for the modeled stellar wind is from a typical O or B type star (e.g. Crowther, 2001, Povich, 2012, Chu, 2008) which has a mass loss rate of $10^{-6}\ \mathrm{M}_{\odot}\ \mathrm{yr}^{-1}$, an outflow velocity $v = 1500\ \mathrm{km\ s}^{-1}$, and an assumed temperature of 10^4 K at an inner boundary of 0.0028 pc. There is no relative motion between the star and the ISM. This is considered in the following chapters. The ISM density is $\rho_{ISM} = 10^{-22.5}\ \mathrm{g\ cm}^{-3}$, with a temperature of

$T_{ISM} = 100$ K. For scenarios assuming a pure hydrodynamic case, the ISM magnetic field is set to $\mathbf{B} = 0$ in the MHD equations.

The fluid contains no neutrals and we assume that the surrounding ISM consists only of protons, implying complete ionization. The effect of neutrals are not included. It is assumed that the ISM surrounding the astrosphere is completely ionized, because the Strömgren spheres around O and B type stars is much larger (> 20 pc) than the radius of the astrosphere (< 10 pc) discussed here. In this model the ISM is assumed to be uniform, and the outflow is spherically symmetric, supersonic and constant in time. The outflow collides with the ISM, pushing it outward, and initially expands freely. A two shock structure arises. The first being an outer shock, or bow shock (BS). Although there is no relative motion considered here, this shock is still referred to as a bow shock. The BS shocks and heats the ISM.

In a wind bubble the relative velocity between the star and the surrounding medium is zero, while for an astrosphere it is not. As long as the outer structure moves supersonically into the ISM, an outer shock or BS will be created. In the end state this motion becomes so slow that it will be subsonic with respect to ISM and thus no BS will exist. This phase is not discussed here since it complicates the boundary conditions. Relatively young cavities are the main focus.

The second shock is a termination shock (TS). This shock forms when the pressure of the ISM balances the pressure of the stellar wind: this is mostly the ram pressure, since the outflow is kinetically dominated. This shock slows the wind to subsonic velocities, and converts the kinetic energy of the wind to thermal energy. This region is referred to as the shocked stellar wind or the inner astrosphere (IAS) and is responsible for the expansion of the astrosphere.

After the formation of the TS, the expansion velocity of the cavity drops. This is because the IAS looses internal energy as it does work on the surrounding medium, and results in a slow moving outer astrosheath. The IAS is separated from the OAS by a tangential discontinuity, known as the astropause (AP).

As mentioned before, in this work the interest is in the influence of different cooling functions on the structure of astrospheres. The cooling functions to be used in this chapter are shown in Figure 2.4. Three different cooling functions namely those proposed by Mellema & Lundqvist (2002), Schure et al. (2009), and the analytic function from Siewert et al. (2004) are used. These cooling functions all assume solar abundances, but differ in the elements taken into account. Different approaches are not discussed here, only the effects on calculations. The different functions are denoted as CF0 for no cooling, CF1 for cooling using the Mellema & Lundqvist (2002) function, CF2 for cooling using the Schure et al. (2009) function, and CF3 for cooling using the function proposed by Siewert et al. (2004) in the model.

3.2.1 The Effect of Different Cooling Functions on Hydrodynamical Simulations

The effects of different cooling functions on numerical simulations are shown in Figure 3.1, and are already apparent after 5 kyrs. Shown here are four computed density profiles cor-

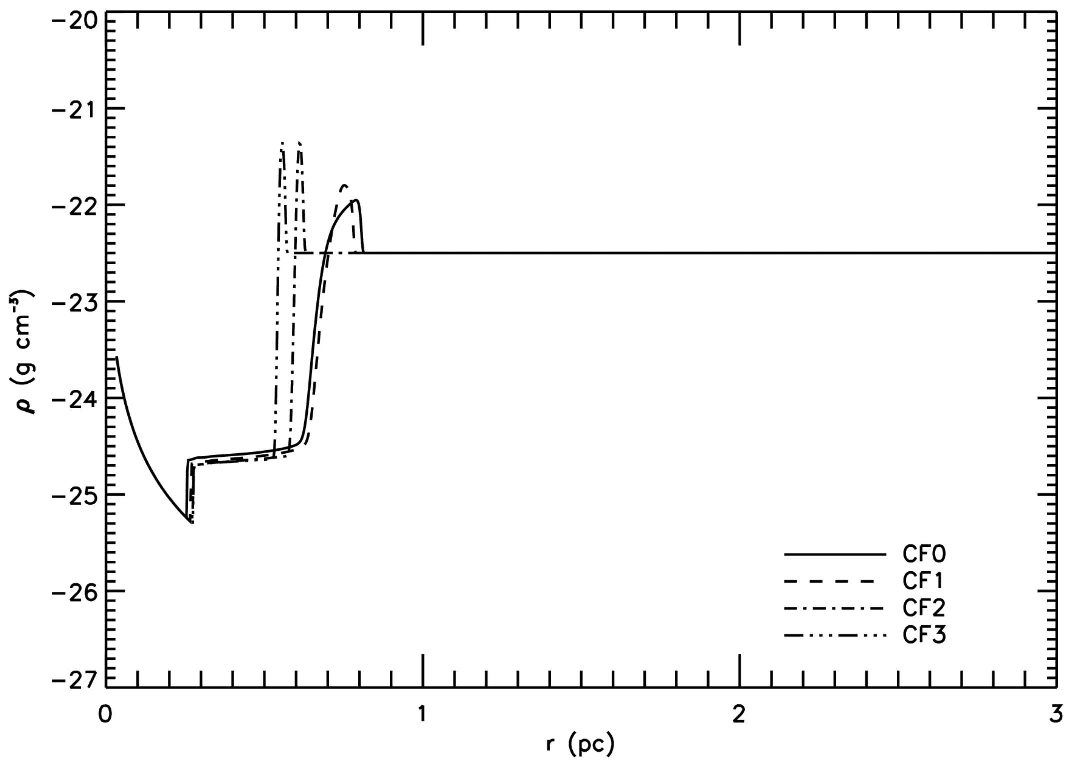

Figure 3.1: The density profiles at 5 kyrs for a pure hydrodynamical model. On the linear x-axis the distance in parsec is shown and on the logarithmic y-axis the density. The four lines correspond to CF0 (solid), CF1 (dashed), CF2 (dot-dashed), and CF3 (dash-dot-dot) line, which are the different cooling functions used in this work.

responding to no cooling (CF0) shown with a solid line, the CF1 scenario uses the Mellema & Lundqvist (2002) cooling function and is shown with a dashed line, the CF2 scenario uses the cooling function found in Schure et al. (2009) and is shown with a dot-dashed line, while the CF3 scenario uses the cooling function from Siewert et al. (2004) and is shown with the dash-dot-dot line. Here it can be seen that after 5 kyrs the effects of CF1 (dashed line) are not very different from the case without cooling (solid line). However, the astropause distance for CF2 (dot-dashed line) and the CF3 (dash-dot-dot line) and the BS are clearly smaller, while TS position remains more or less the same for all cases. The compression ratios, i.e. the ratio of the density before the BS and the density directly after the BS, for CF0 and CF1 are more or less similar, corresponding to a value of 4, which is expected for a strong shock. The CF2 and CF3 density profiles, however, have much larger compression ratios, due to effective radiative cooling at this young simulated age.

In Figure 3.2, the evolution of astrospheres as calculated by the model after 40 kyrs is shown. The CF0 case follows the traditional no cooling description, while the density profiles for CF1, CF2, and CF3 results in much higher compression ratios at the BS. As expected, the no-cooling scenario (CF0) has also resulted in an evolution to larger distances than those with cooling. The compression ratio of CF1 and CF3 is of the same order, while being larger than that of

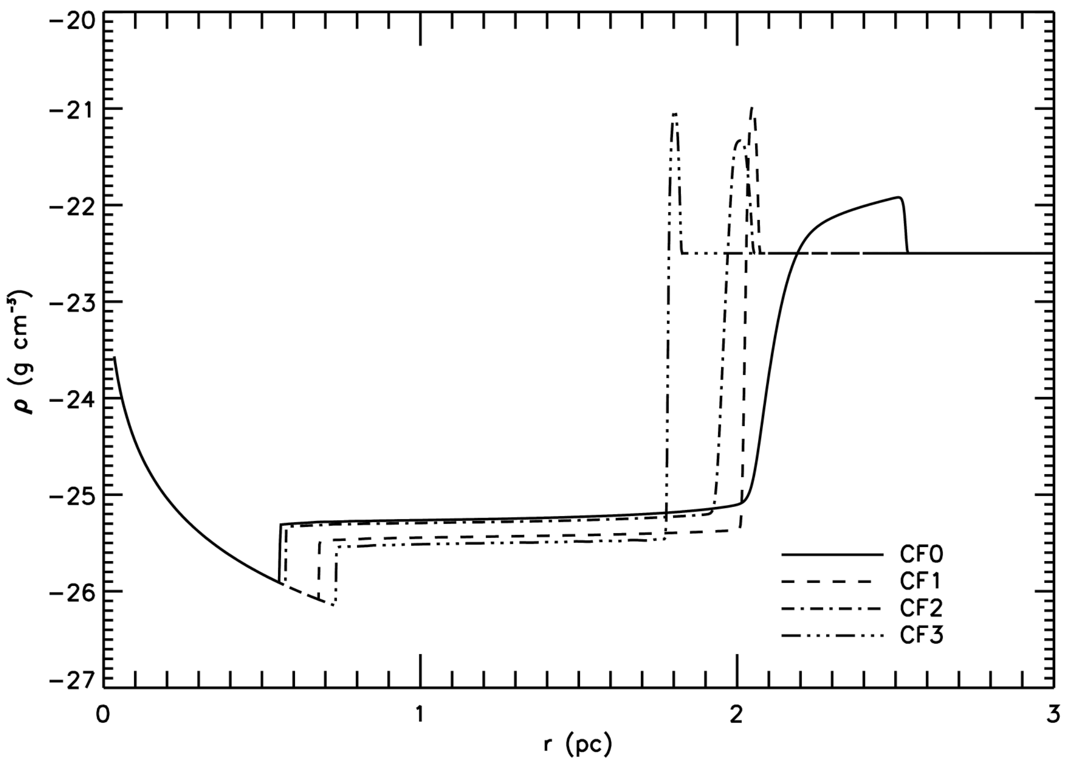

Figure 3.2: Similar to Figure 3.1 but for 40 kyrs.

CF2.

It can be noted in Figure 3.2 that the TS shock distances have evolved differently for all four scenarios, while the compression ratios for all four scenarios at the TS remain more or less the same. The reason for this can be seen in Figure 3.3 in which the the thermal pressure is shown as a function of radial distance for the different scenarios. Again the no cooling (CF0) solution is shown with a solid line, the CF1 scenario uses the Mellema & Lundqvist (2002) cooling function and is shown with a dashed line, the CF2 scenario uses the cooling function found in Schure et al. (2009) and is shown with a dot-dashed line, while the CF3 scenario uses the cooling function from Siewert et al. (2004) and is shown with the dash-dot-dot line. It should be noted that due to the Rankine-Hugoniot relations for high Mach numbers the thermal pressure of the shocked region is equal to three quarters of the ram pressure of the unshocked medium (Dyson & Williams, 1997). The remaining one quarter goes into the ram pressure of the shocked medium. Thus, in Figure 3.2 the thermal pressure seems to be constant, because the remaining one quarter or less cannot be resolved on the logarithmic scale.

Figure 3.3 depicts how the thermal pressure is nearly constant in the IAS and OAS region i.e. the regions between the TS and BS. This is a consequence of momentum conservation, of the MHD equations with $\mathbf{B} = 0$, and is also why the TS distance can be estimated, as described in Scherer et al. (2016).

It can be seen in Figure 3.3, in the absence of radiative cooling, that the thermal pressure for

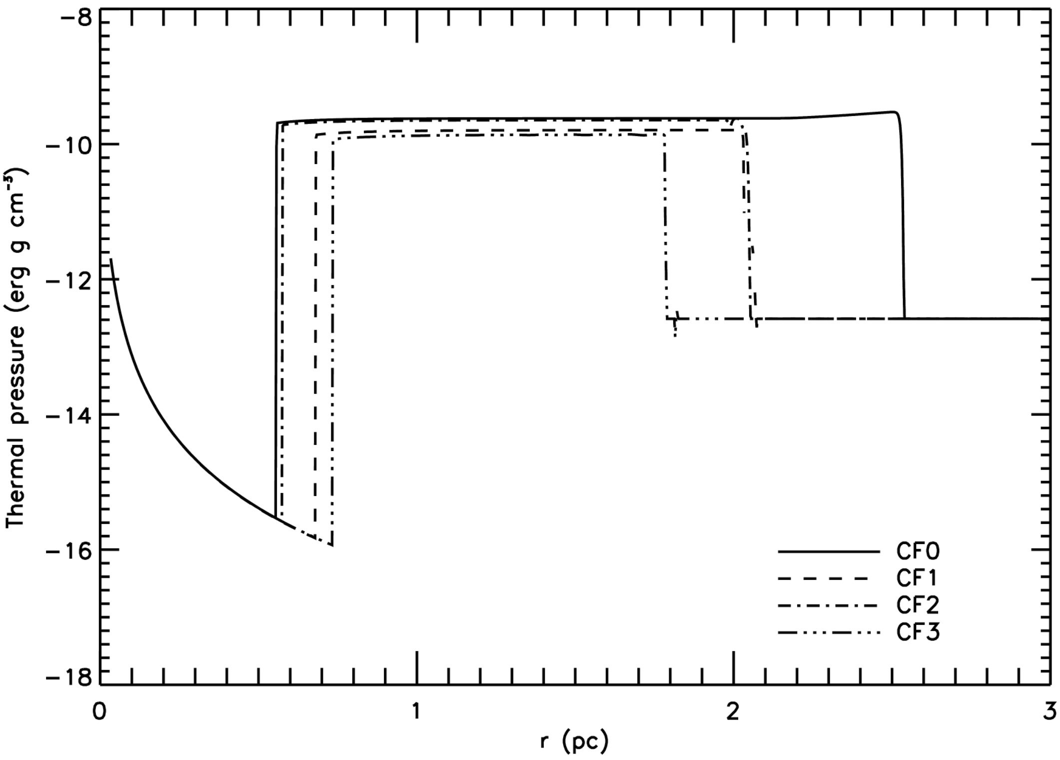

Figure 3.3: The resulting thermal pressure at 40 kyrs for the three cooling functions. Note that these are hydrodynamical simulations i.e. the magnetic field is not present. Again the four lines correspond to CF0 solid, CF1 dashed, CF2 dot-dashed, and CF3 dash-dot-dot line.

the CF0 case is the highest, and thus more work has to be done by the stellar wind to push the TS forward. In the CF2 scenario the thermal pressure in the IAS and OAS regions is almost as high as in the CF0 scenario, but the cooling in the OAS compresses that region, so that the BS distance is smaller compared to the CF0 scenario. In the CF1 scenario the thermal pressure is lower in the IAS and OAS regions and the cooling of the stellar wind is negligible. The cooling reduces the thermal pressure, and in order to balance, the BS has to move inward compared to the no-cooling scenario.

It is important to note that the different cooling functions will have a different dependence on temperature, and the cooling time would therefore have a different velocity dependence. For a supersonic outflow (as simulated here) this would result in a large cooling time, resulting in no cooling after the shock. Furthermore, the small density of the IAS results in a further increase of the cooling time. A further description of the dynamics of fast and slow stellar outflows can be found in Koo & McKee (1992).

3.2.2 The Effect of the ISM Density on Cavity Evolution

A snapshot of different density profiles for scenarios corresponding to different ISM densities is shown in Figure 3.4 for 40 kyrs, using the CF1 cooling function. Shown here is that

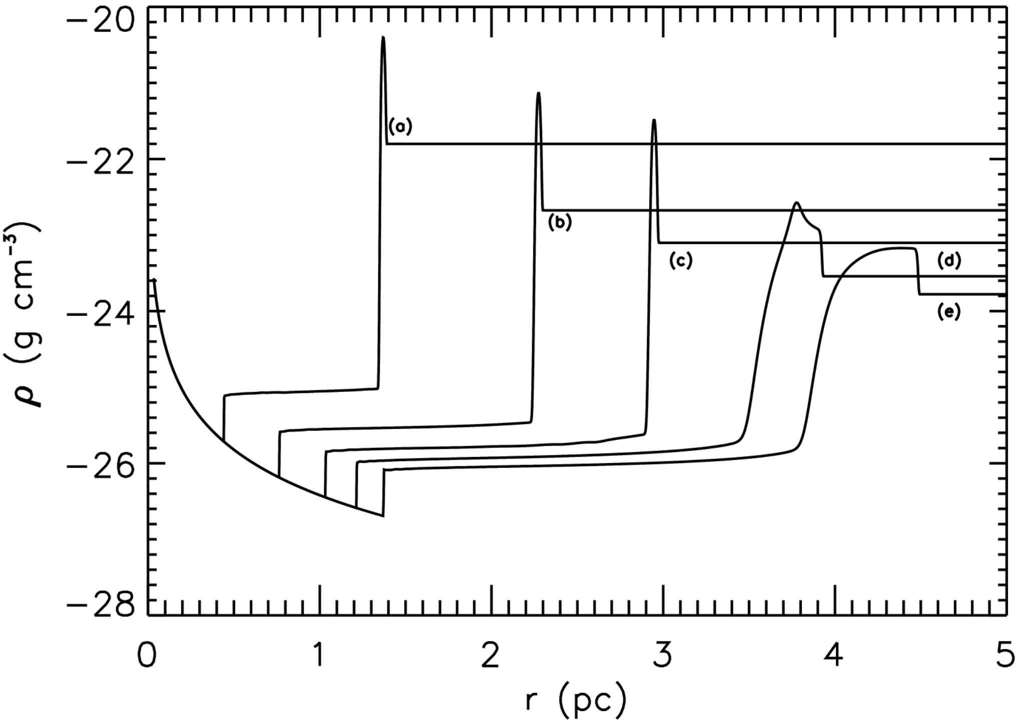

Figure 3.4: Computed density profiles for different ISM densities at 40 kyrs for the CF1 cooling function. (a) has an ISM density of 1.58×10^{-22} $\mathrm{g\,cm^{-3}}$, (b) 2.108×10^{-23} $\mathrm{g\,cm^{-3}}$, (c) 7.90×10^{-24} $\mathrm{g\,cm^{-3}}$, (d) 2.87×10^{-24} $\mathrm{g\,cm^{-3}}$, (e) 1.66×10^{-24} $\mathrm{g\,cm^{-3}}$.

increasing the ISM density increases the pressure from the ISM and results in a smaller astrosphere/cavity. Here it can be seen that after 40 kyrs the shock structure depends strongly on the ISM density. For increasing density, the compression ratio increases and the BS is not able to move out as far. This increase in the compression ratio is a result of radiative cooling with the cooling time directly proportional to density (Koo & McKee, 1992).

For the highest ISM density, scenario (a), the OAS is more compressed, meaning that radiative cooling has been more effective due to the lowering of the cooling time. This means that radiative cooling has been effective and explains the high compression ratio. For lower ISM densities, however, cooling is less effective e.g. as seen in scenario (e), which results in a lower compression ratio (≈ 4).

Scenario (d) further illustrates the complex structure that results from including radiative cooling. This is shown in more detail by the dashed line in Figure 3.5, while the solid line in Figure 3.5 shows the result when radiative cooling is not included. Here the OAS shows a fine structure consisting of HOAS, found directly after the BS, and a COAS found closer to the AP. The COAS is a direct result of radiative cooling, which cools the gas and increases the density. The effect on temperature is shown in the bottom panel of Figure 3.5, where the TS is found at ≈ 1.2 pc, and the AP at ≈ 3.5 pc after which the OAS is found. Here the fine structure of the OAS can be seen in terms of the temperature, where the HOAS results from the BS found at ≈ 4 pc.

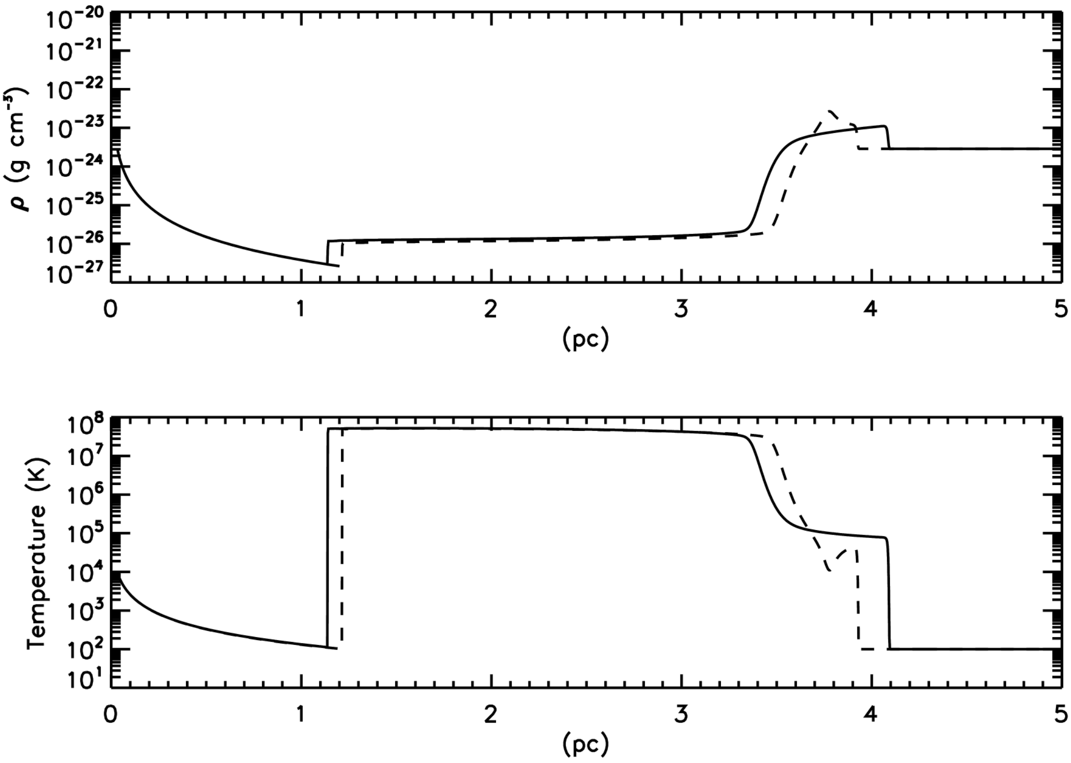

Figure 3.5: The stellar wind density (top panel) and temperature (bottom panel) profile for an ISM density of 2.87×10^{-24} $\mathrm{g\ cm^{-3}}$ for 40 kyrs without radiative cooling. Results without radiative cooling is shown with a solid line, while results with radiative cooling included is shown with a dashed line.

Radiative cooling takes place and the temperature of the HOAS starts to decrease soon after the BS. The COAS is found close to the AP where it can be seen to have a considerably lower temperature then the HOAS found after the BS. The fine structure of the other scenarios cannot be resolved since it would require a higher resolution.

Figure 3.6 shows the time evolution of the lowest density profile in Figure 3.4, from 20 kyrs to 100 kyrs, using the CF1 cooling function for an ISM density of 1.66×10^{-24} $\mathrm{g\ cm^{-3}}$. It can be seen that the cooling time has increased such that the OAS only starts cooling at 40 kyrs, and has significantly cooled at 60 kyrs. This is in contrast to the higher ISM densities where significant cooling in the OAS has already taken place at 40 kyrs (Figure 3.4). The TS moves outward, but is decelerating with increasing time. The motion of the AP and the BS also slows down, and the size of the inner astrosheath increases, while the size of the outer astrosheath decreases to a thin structure. At the earliest stage, the compression ratio is quite low, within the range expected from the Rankine-Hugoniot relations for an ideal gas, but increases with time to much higher values. The reason is that the temperature decreases, and the pressure must balance the unshocked stellar wind ram pressure, and thus the density must increase according to the ideal gas law.

Figure 3.7 shows the compression ratio on a logarithmic scale of the COAS as a function of time in kyrs for an ISM density of 2.87×10^{-24} $\mathrm{g\ cm^{-3}}$ using CF1, shown with a solid line, and CF2,

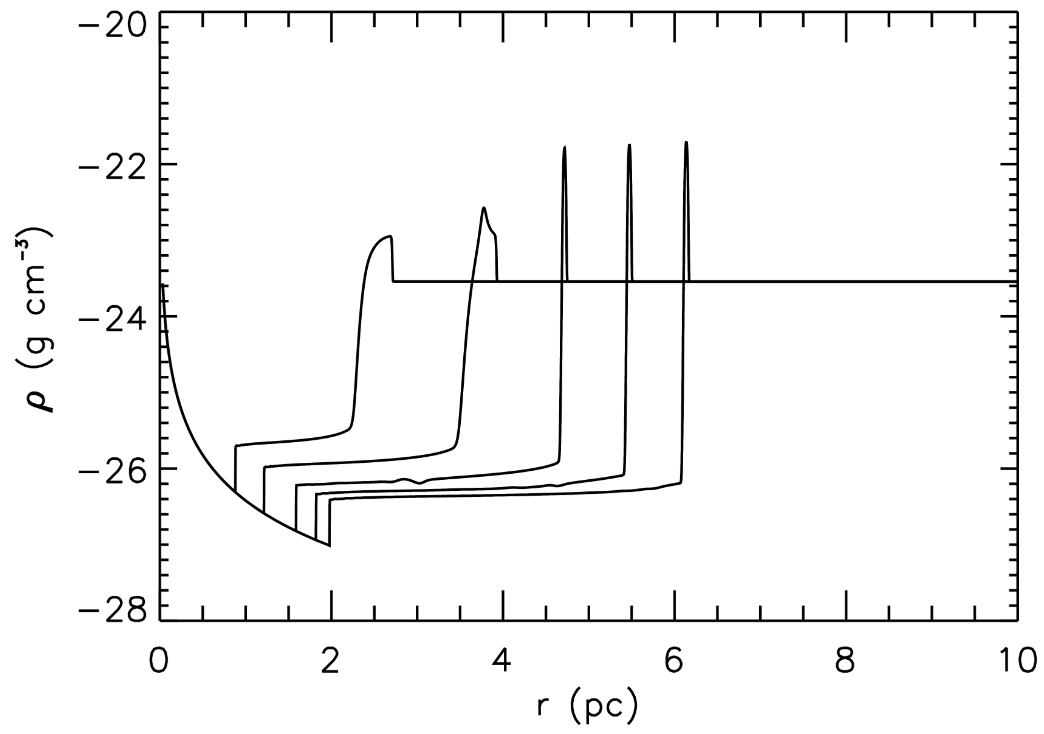

Figure 3.6: Stellar wind density profiles for an ISM density of 2.87×10^{-24} $\mathrm{g\,cm^{-3}}$ for times 20, 40, 60, 80, and 100 kyrs.

shown with a dashed line. The behaviour of the compression ratio can be very different depending on the choice of cooling function, as shown in Figure 3.7. The results using CF1 (solid line) show a slowly increasing compression ratio at early times, $\approx$ 40 kyrs, where the compression ratio is close to 4. However, at around 40 kyrs the compression ratio increases up to around 60. At around 50 kyrs the increase is more gradual, reaching a maximum compression ratio at 100 kyrs of less than 70.

The results are very different when using CF2 (Figure 3.7, dashed line). Here the compression ratio increases at early times up to to 5 kyrs where the compression ratio is almost 20. This indicates a smaller cooling time than for the computations using CF1. At $\approx$ 5 kyrs the increase in compression ratio is more gradual, reaching a maximum of $\approx$ 30. After which the compression ratio decreases gradually, reaching a value of $\approx$ 20 at 100 kyrs. Figure 3.7 shows that the choice of cooling function used in the model is important.

The compression ratio as a function of ISM density at different times at the outer boundary or BS is shown in Figure 3.8, where the the focus is on results from CF1 and CF2. The black lines show the compression ratios for 10 kyrs, while the red lines show the compression ratios for 80 kyrs, where the dashed line shows the results using CF1 and the dashed-dot line the results from CF2 cooling functions. Note that the compression ratios are only shown for those ISM values in Figure 3.4.

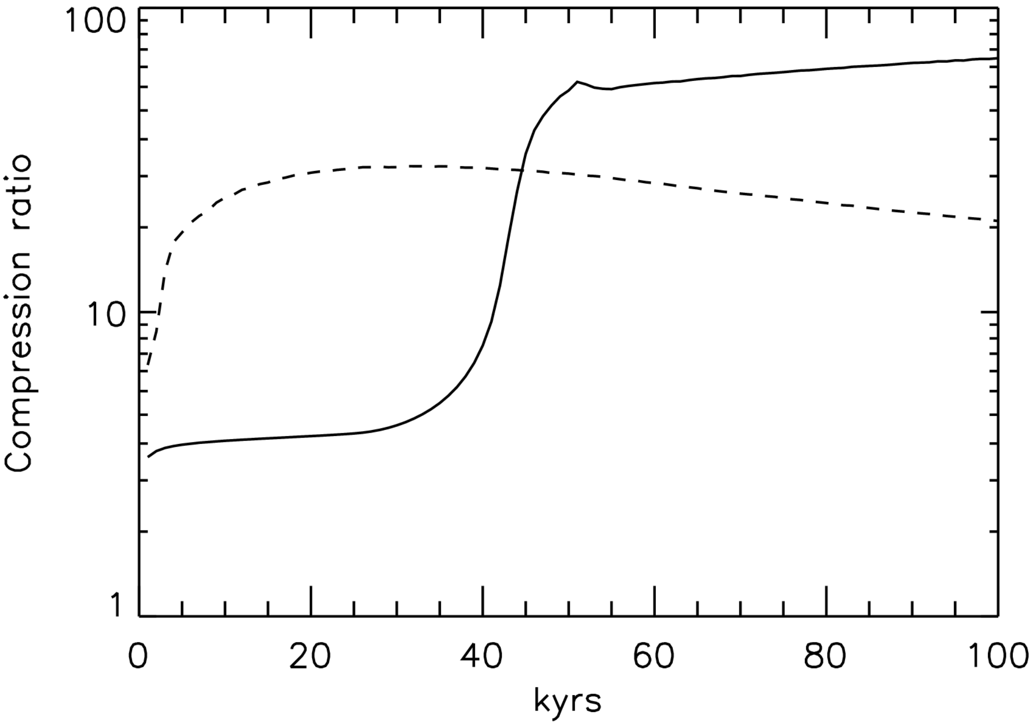

Figure 3.7: The compression ratio of the COAS for an ISM density of 2.87×10^{-24} g cm^{-3} as function of kyrs shown on a log scale. The solid line shows the compression ratios using CF1, while the dashed line shows the results using CF2.

The compression ratio, for 10 kyrs (black lines) and for CF1 at low densities, show the expected value without cooling which is approximately 4, implying that radiative cooling is not effective for low ISM densities, which is consistent with what is previously shown. This implies a larger cooling time for low ISM densities, and since the dynamical time is not larger then the cooling time, no cooling is observed. This is followed by higher compression for higher ISM densities followed again by a decrease in compression for the highest ISM values, indicating a time-dependence in the process for this particular scenario. This is in contrast to the compression ratio calculated using the CF2 cooling efficiencies, which show maximum compression for lowest ISM densities and then decreasing at higher ISM densities.

In Figure 3.8 for 80 kyrs (red lines), the compression ratios resulting from CF1 now follow a similar trend, indicating that the cooling time is indeed high for lower densities. It is also observed that the results using CF1 show more compression than that of CF2 while cooling has taken place for all ISM densities. This again shows that the cooling time is larger for low ISM densities, however, once the cooling starts, the compression ratio is larger for low ISM densities and lower for large ISM densities. The results from CF2 also show less compression over time, with the compression ratio for 10 kyrs (black dash-dot lines) larger than that of the results of 80 kyrs (red dot-dashed lines).

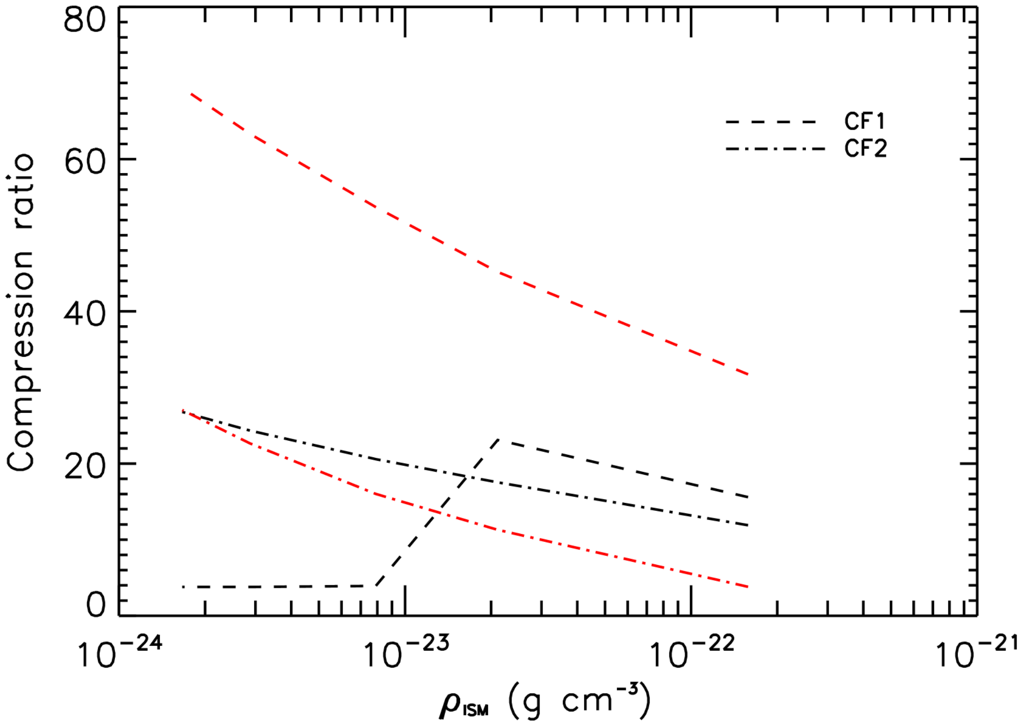

Figure 3.8: The computed compression ratio for 10 kyrs (black lines) and 80 kyrs (red lines) as function of ISM density. The dashed lines show the solutions using CF1, while the dot dash lines show the solution using CF2.

3.3 The Effect of Ram Pressure on Cavity Evolution

In this section, a study will be made to show the effects of varying the ram pressure of the stellar wind outflow on the computed cavities. This is done by changing the mass loss rate in the model. The density at the inner boundary is given by the continuity equation

$$\rho = \frac{\dot{M}}{4\pi r^2 v}, \tag{3.1}$$

where $\dot{M}$ is the mass loss rate of the star, r is the distance, and v is the bulk speed. The ram pressure is given as

$$P_{ram} = \frac{1}{2}\rho v^2. \tag{3.2}$$

From these equations it is clear that changing the mass loss rate also changes the ram pressure. In Figure 3.9 the computed cavities correspond to 3 different scenarios of mass loss rate. These are given in terms of solar mass loss rates: $\mathrm{M}_\odot$, and are 10^{-6} $\mathrm{M}_\odot$ yr^{-1} shown with a solid line, 5×10^{-6} $\mathrm{M}_\odot$ yr^{-1} shown with a dashed line, and 10^{-5} $\mathrm{M}_\odot$ yr^{-1} shown with a dot-dash line.

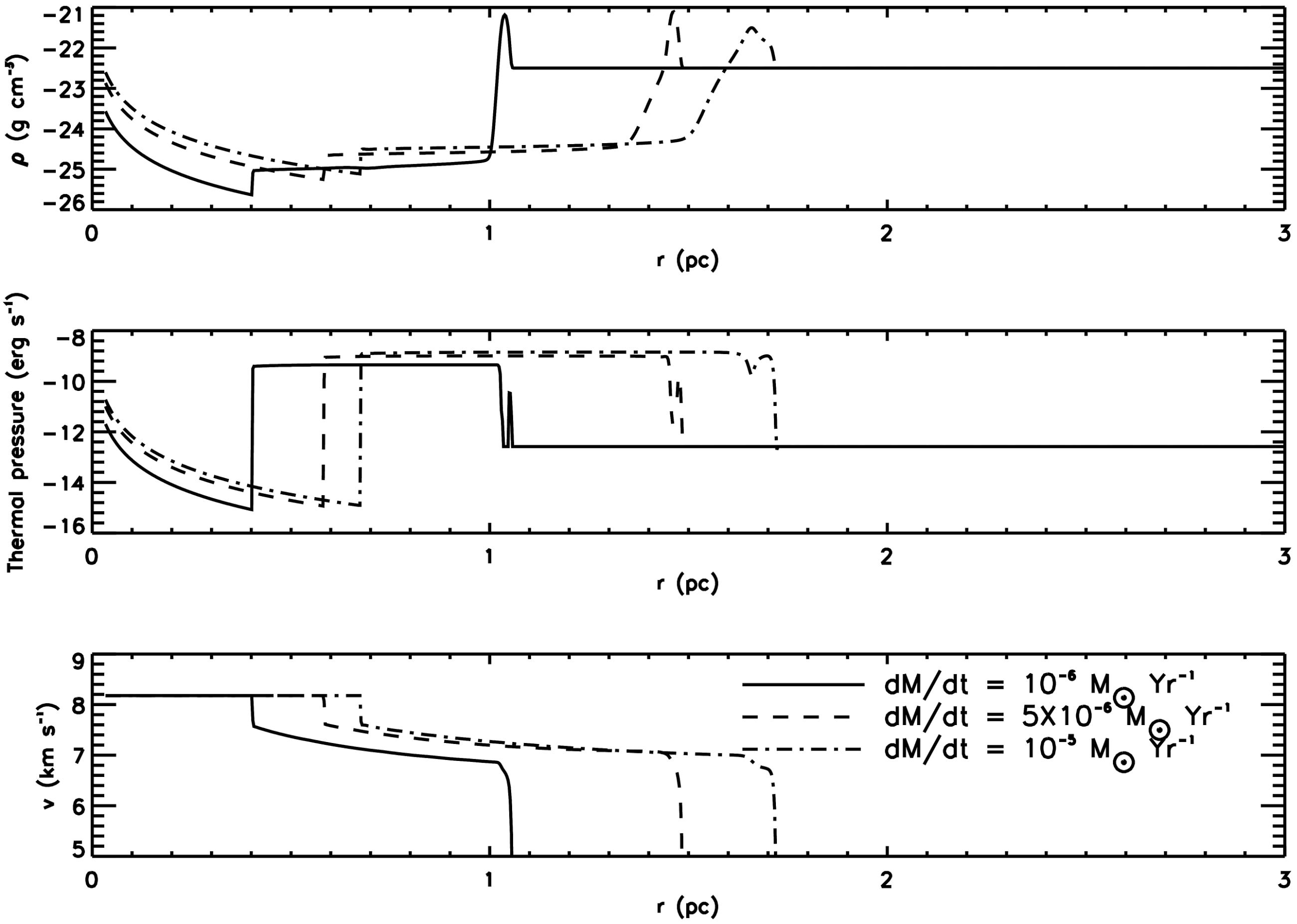

Figure 3.9: The effect of different mass loss rates at 10 kyrs. The 10^{-6} $\mathrm{M_\odot}$ yr^{-1} scenario is shown as a solid line, the 5×10^{-6} $\mathrm{M_\odot}$ yr^{-1} scenario shown as a dashed line, and the 10^{-5} $\mathrm{M_\odot}$ yr^{-1} scenario shown as a dot-dash line. The cooling function from Mellema & Lundqvist (2002) (CF1) is used.

From Figure 3.9 it is clear that the extent of the cavity grows as the mass loss rate is increased. The position of the TS is also further out as a result of the increase in density . The increase in density can be explained with Equation 3.1. This is to be expected, since the increasing ram pressure implies that it can push the stellar outflow out further before it is stopped by the ISM pressure.

The energy available for the expansion of the shocked wind is also larger, hence the increased size of the shocked wind region, as the ram pressure is increased. After the TS, some of the ram pressure is converted to thermal pressure. The increase in ram pressure then results in an increase in the thermal pressure of the shocked wind; this drives the expansion of the shocked region. A quarter of the original ram pressure is still available after the TS, and also drives the expansion of the shocked region.

The density profile of Figure 3.9 also shows differences in the OAS region after the BS. Here the effectiveness of radiative cooling at this particular time can be inferred from the compression ratio. For the highest mass loss rate, 10^{-5} $\mathrm{M_\odot}$ yr^{-1} (dot-dash line) case, it can be seen that the least amount of radiative cooling has taken place, then followed by the 5×10^{-6} $\mathrm{M_\odot\ yr^{-1}}$ scenario (the dashed line), and then the 10^{-6} $\mathrm{M_\odot\ yr^{-1}}$ scenario (solid line), showing an almost completely collapsed OAS. The compression ratio of this region is lowest for the highest ram pressure. This is to be expected, since it was pointed out earlier that the cooling time is sensitive to the shock velocity. Therefore the cooling is less effective for the highest mass loss rate (the dot-dash line).

The BS region of the thermal pressure profile also indicates the hot outersheath and cold outersheath positions. The 10^{-5} $\mathrm{M_\odot\ yr^{-1}}$ scenario (dot-dashed line) is the best example of this. The position where the thermal pressure (just before the BS but after AP) starts to drop would indicate the point where radiative cooling becomes effective. This point then indicates the boundary of the hot outersheath region and the beginning of the cold outersheath region. The lowest thermal pressure in this region would then indicate the position of the radiatively cooled dense plasma. This is in sharp contrast to the thermal pressure of CF0 in Figure 3.3, where no such changes are observed.

3.4 The Effect of Magnetic Field Pressure on Cavity Evolution

In this section the influence of the ISM magnetic field will be studied by adding a 3 μG and a 0.5 μG magnetic field to the model. Note that since these simulations are done only in 2D it is assumed than an azimuthal ISM magnetic field is found around the star. This is, however, not realistic, but it will show maximum effect, since the field is always perpendicular to the outflow. Of interest is mainly the influence of the magnetic field on the radiative cooling results. By adding magnetic pressure, the energy equation has to balance the magnetic field and thermal pressure against the energy losses from the cooling function. Note that the stellar magnetic field falls as $1/r^2$ and, according to van Marle et al. (2015), can be neglected in simulations, as is done in this work. Relative motion is also not be included in this chapter, but is included in a later chapter.

3.5 Effect of the ISM Magnetic Field Pressure on Simulations

Figure 3.10 is similar to Figure 3.1, however, the latter is for an ISM magnetic field of 3 μG. When compared to Figure 3.1, it can be seen that the CF0 and CF1 scenarios are much more similar, while CF2 scenario shows a larger cavity than for the corresponding HD result. The CF3 result also shows a more decompressed OAS when the magnetic field is included.

Figure 3.11 shows the same as Figure 3.2, but with the ISM magnetic field included. Again, the results deviate from the pure HD results. The inclusion of the magnetic fields leads to a much less compressed OAS in all cases. The decompression of the OAS caused by the ISM magnetic field leads to lower density and an increase in the cooling time.

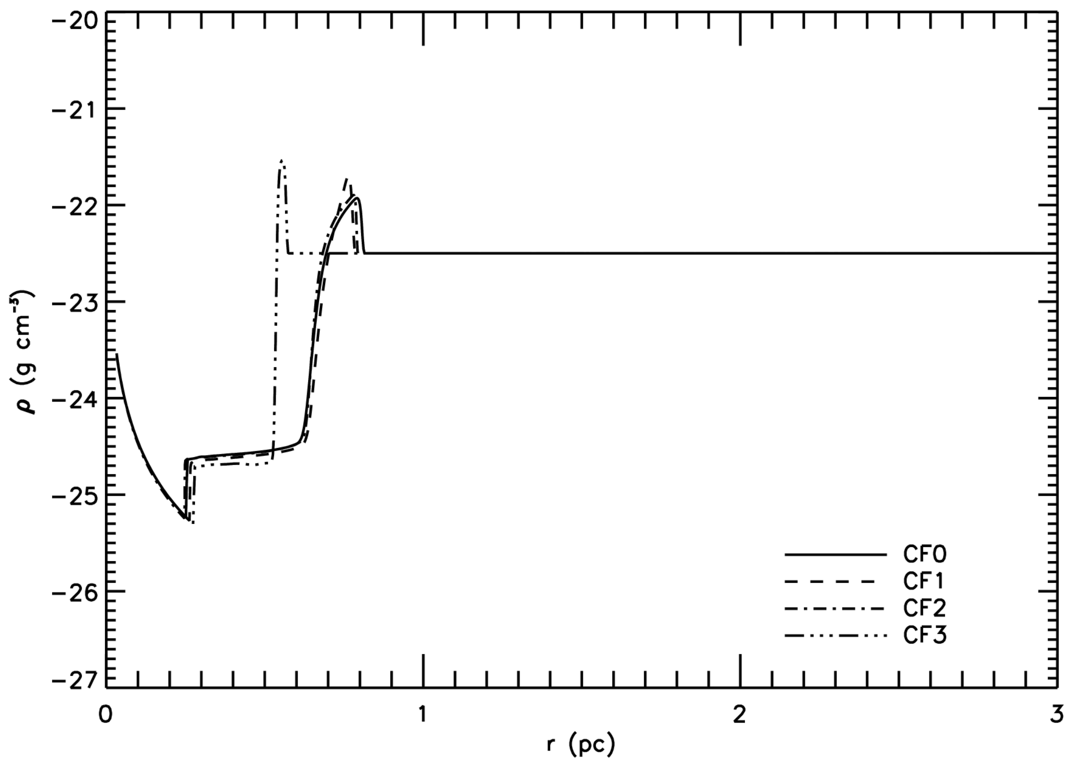

Figure 3.10: The density profiles at 5 kyrs when magnetic field pressure is added. The four lines correspond to CF0 solid, CF1 dashed, CF2 dot-dashed, and CF3 dash-dot-dot line. An ISM magnetic field of 3 μG is also included. The density is again plotted on a logarithmic scale. Note that there is no cooling for the CF2 scenario for this set of parameters; the CF2 results are therefore the same as the CF0 results.

3.6 The Effect of the ISM Density on Cavity Evolution, Including the Interstellar Magnetic Field

The compression ratio of the OAS is shown as a function of time on a logarithmic scale in Figure 3.12. The results using the CF1 cooling function are shown with a solid line, while the results using the CF2 cooling function are shown with a dashed line. The compression ratio is again different for the two different cooling functions used, and is also very different from Figure 3.7, which shows the results without the ISM magnetic field. The results using CF1 (solid line) show a sudden increase in compression ratio up to $\sim$ 5 kyrs, reaching values of more than $\sim$ 8. This is very different from what is found in Figure 3.7, where the compression ratio increases gradually at early times. From $\sim$ 5 kyrs to $\sim$ 20 kyrs, the compression ratio decreases and remains more or less constant at a value of almost 7 up to 40 kyrs, after which the compression values decrease gradually, reaching a value of $\sim$ 5.2 at 100 kyrs.

The calculations using CF2 (dashed line) in Figure 3.12 are also very different from those in Figure 3.7, where the ISM magnetic field is not included. Here the results show a slow monotonical increasing compression ratio up to 80 kyrs, reaching a maximum value of $\sim$ 7, after which the compression ratio decreases gradually, reaching a value of almost $\sim$ 6.2 at 100 kyrs.

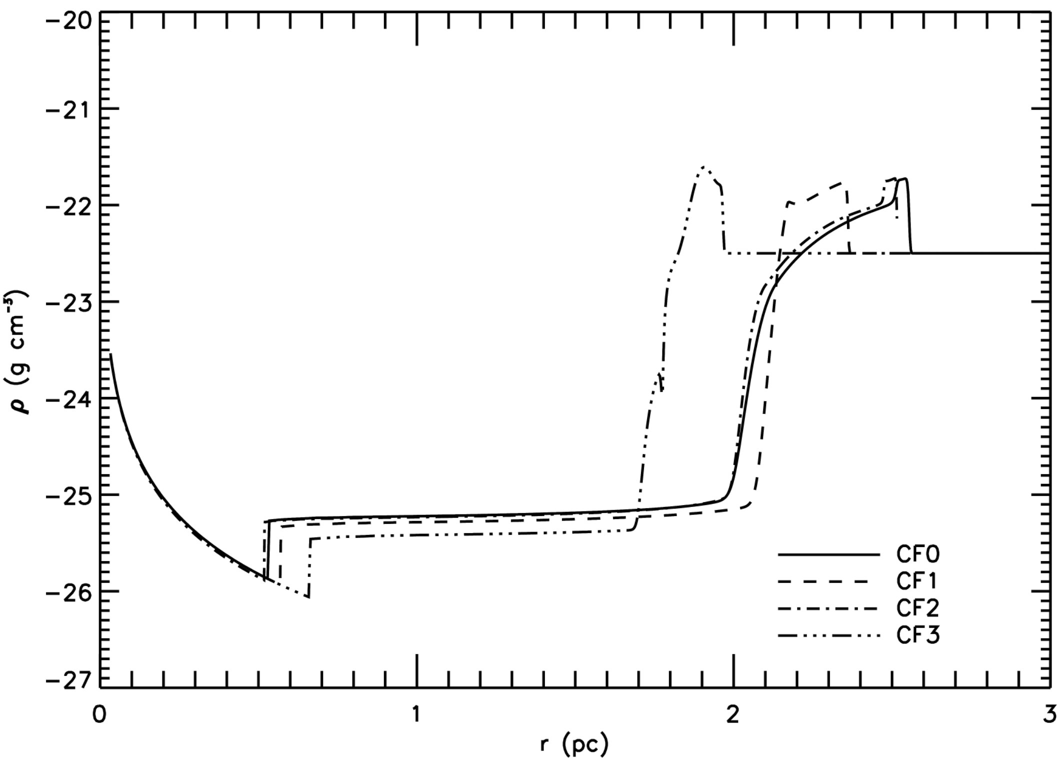

Figure 3.11: The same as in Figure 3.10 but for 40 kyrs, and an ISM magnetic field of 3 μG. Note that there is no cooling for the CF2 scenario for this set of parameters, the CF2 results are therefore the same as the CF0 results.

The compression ratios in Figure 3.12 are generally much less than those of Figure 3.7, and indicate the effects of the ISM magnetic field in reducing the maximum compression ratio.

Figure 3.13 shows the compression ratio for the case with a magnetic field of 3 μG, using the cooling efficiencies of CF1 (dashed lines) and CF2 (dot-dash lines) for 10 kyrs (black lines), and 80 kyrs (red lines). This is similar to Figure 3.8 for the pure hydrodynamic case. Here, the compression ratio increases with increasing ISM density. This is a result of the decreasing importance of the magnetic field pressure for higher ISM densities, making it difficult for the magnetic field pressure to counteract the compression that results from radiative cooling. At higher ISM densities, the thermal pressure becomes increasingly important. In Figure 3.13 it is the cavity that results from the use of the cooling efficiencies of CF1 that cools first, implying a shorter cooling time than those from CF2, as previously explained. It is again seen from the CF1 solution that the compression ratio at 80 kyrs is lower than those from 10 kyrs.

The behaviour of the compression ratio resulting from CF2 at 10 kyrs (black dot-dashed line) is again very different from the result obtained for CF1 in Figure 3.13. Here, an increase in this ratio takes place at low ISM densities, and is then followed by a decline, after reaching a maximum value. For the HD result at 10 kyrs using CF1, it is found that the compression ratio is constant at 4, meaning that no radiative cooling took place. Afterwards, the compression ratio increases rapidly to a maximum, followed by a steady decrease.

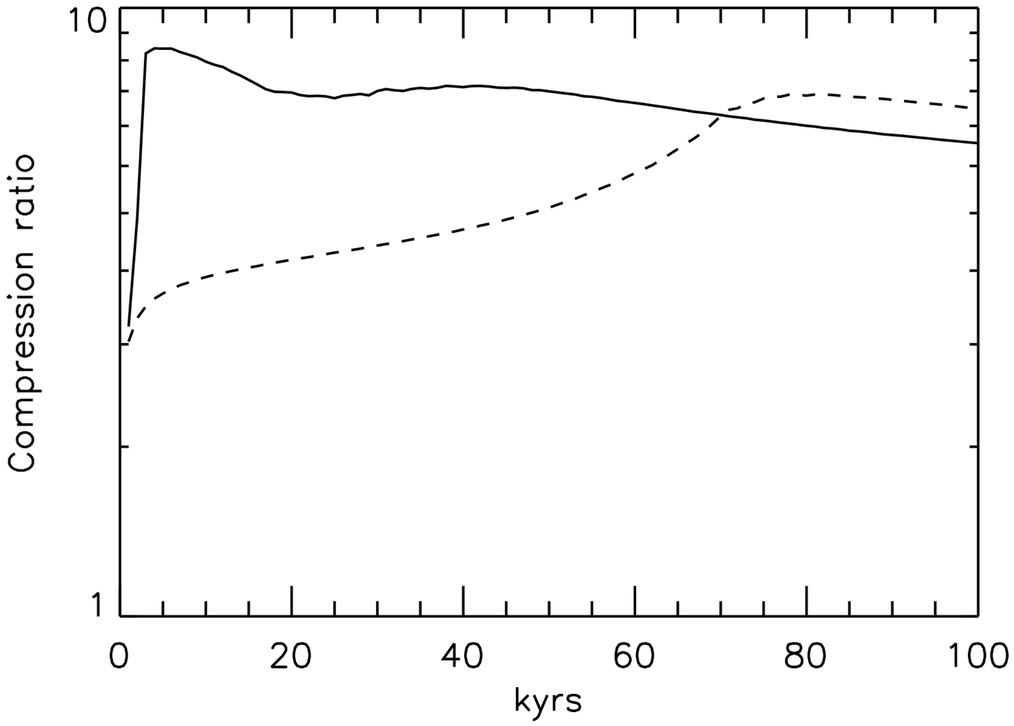

Figure 3.12: The computed compression ratio for an ISM density of 1.58×10^{-22} $\mathrm{g\,cm^{-3}}$ as function of time shown on a logarithmic scale. The solid line shows the compression ratios using CF1, while the dashed line shows the results using CF2. An ISM magnetic field of 3 μG is included.

Figures 3.14 and 3.15 highlight the effects of the ISM magnetic field and radiative cooling on cavity evolution using the cooling function CF1, and are shown as contour plots of density as a function of radial distance and time for $B = 0.5$ μG and $B = 3$ μG, with and without radiative cooling. The position of the TS is indicated with a solid line, and the BS is indicated with a dashed line.

As noted before, radiative cooling results in a drop in pressure, mainly in the OAS. This drop in pressure results in the TS being pushed forward. Since the TS is formed when the thermal pressure and magnetic pressure from the ISM can balance the ram pressure from the stellar wind, the resulting drop in pressure from the OAS that results from radiative cooling causes the termination shock to be pushed out further. The drop in OAS thermal pressure has however the opposite effect on the OAS which is pushed backward. An increasing magnetic field increases the pressure. In this scenario the TS is pushed back, while the shocked ISM is pushed forward.

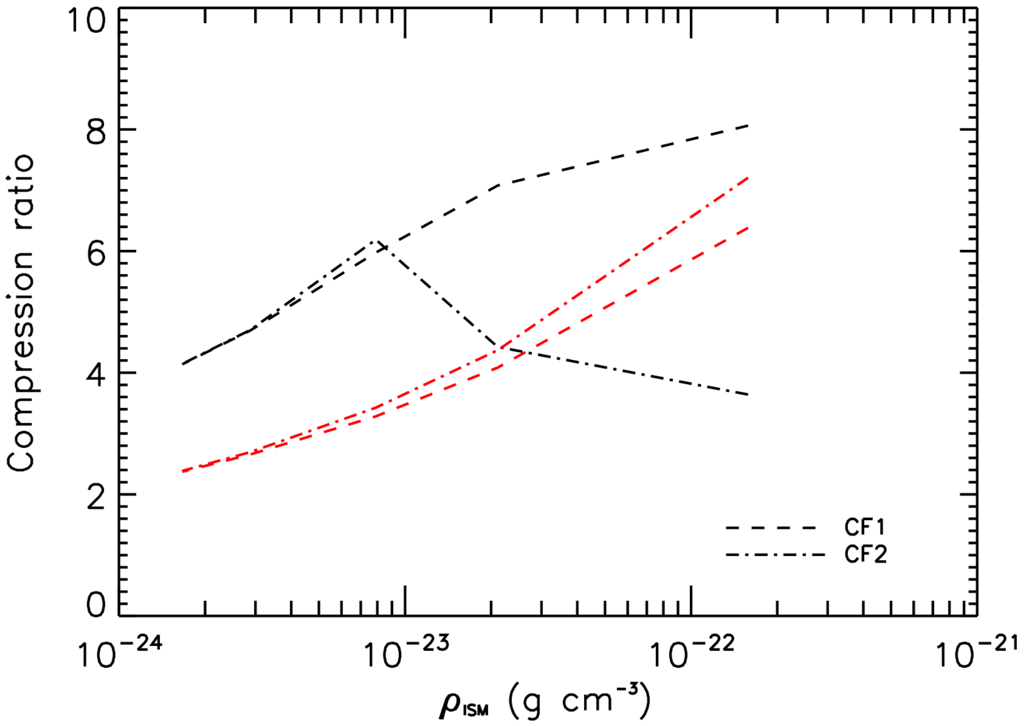

Figure 3.13: The computed compression ratio as function of ISM density for 10 kyrs (black lines) and 80 kyrs (red lines). The dashed lines shows the solutions using CF1 while the dot dash lines shows the solution using CF2. An ISM magnetic field of 3 μG was also included.

3.7 Summary and Conclusions

In this chapter the model, as described in the previous chapter, is applied. As a first step, to illustrate the effect of radiative cooling and computed cavities, it is assumed that the outflow is spherically symmetric, and the ISM is considered uniform with no relative motion.

As shown in Figure 3.1, for a pure hydrodynamical solution, the effects of radiative cooling become important early in the evolution of the cavity for the parameters assumed in that computation. The choice of cooling function is shown to not be trivial, since this choice affects the geometrical extent of the cavity, e.g. the position of the termination shock, bow shock, and astropause. The compression ratio at the bow shock is also shown to vary with the choice of cooling function.

As shown in Figures 3.1 and 3.2, radiative cooling does not affect the compression ratio at the TS, since cooling is not dynamically important at this point. This is a result of the high outflow velocity and low density of the shocked wind. Both these factors result in the increase of the cooling time.

Radiative cooling is also affected by the choice of ISM density, with lower ISM densities increasing the cooling time. This is shown in Figure 3.4. For lower densities, the cooling becomes

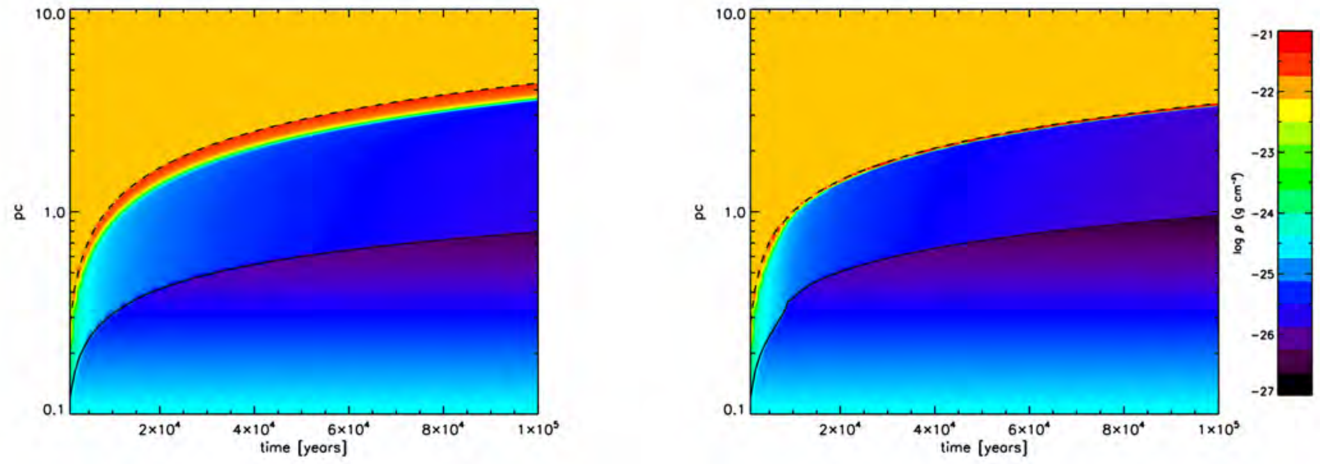

Figure 3.14: Contour plots of density (on a logarithmic scale) as a function radial distance (on a logarithmic scale) and time for $B = 0.5$ μG.

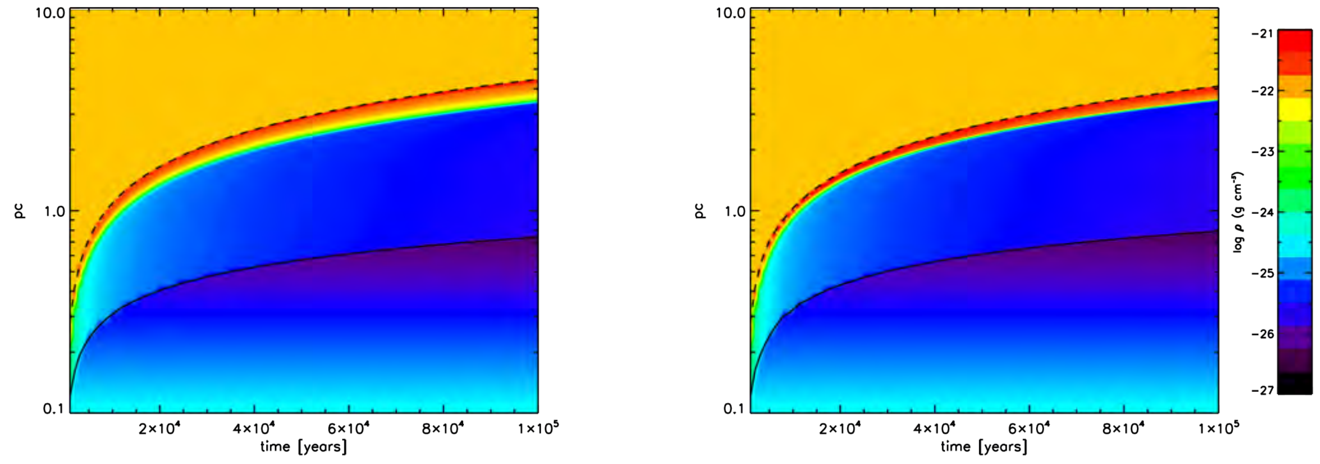

Figure 3.15: Contour plots of density (on a logarithmic scale) as a function radial distance (on a logarithmic scale) and time for $B = 3$ μG.

important at a much later stage.

It is also found that, depending on parameters, including the effects of radiative cooling results in the creation of a fine structure in the outer astrosheath as shown in Figure 3.6. This fine structure can be described as the hot outer astrosheath and the cool outer astrosheath. The hot outer astrosheath is found directly after the BS, while the cool outer astrosheath can be found closer to the AP. This is a result of the hot shocked plasma having sufficient time to cool radiatively resulting in a cool plasma closer to the AP.

The compression ratio is also shown to be a function of ISM density, and varied significantly with the choice of cooling function. In Figure 3.8, the highest maximum compression is found at the lowest ISM density values. This again shows that the choice of cooling function is not trivial. The compression ratio CF2 is found to decrease with time, while a more complex time and ISM density dependent structure is seen for CF1. This indicates the differences in cooling time for the same parameters, but for different cooling functions.

The effect of the ISM magnetic field on the astrosphere, including radiative cooling is done by adding a 3 μG and a 0.5 μG magnetic field. The stellar magnetic field is not taken into account, since it is found that the stellar magnetic field of massive stars is only important close to the surface, and tends to be dominated by the ram pressure of the wind at large distances (see van Marle et al. (2015) and references therein). It is found that the magnetic field prevents the compression of the OAS that results from radiative cooling. This lack of compression lowers the density, making radiative cooling less effective.

The compression ratio is shown as a function of ISM density in Figure 3.13 for the case where including an ISM magnetic field. The results with the magnetic field are found to be very different. Once cooling has set in at all ISM densities, it is found that the compression ratio increases with ISM density. This is the opposite of what is found for the pure hydrodynamic solutions. This is because the magnetic pressure dominates at lower ISM densities and then resits the compression. At higher ISM densities, the thermal pressure dominates, and radiative cooling becomes more effective.

A further deviation from the HD solution is found in that the solutions using the CF1 cooling function cools before those using the CF2 cooling function. This is found to be the opposite of the hydrodynamic solutions. This shows that radiative cooling using different cooling functions can behave very differently when the magnetic field is included.

Figures 3.14 and 3.15 shows the influence of a weaker and stronger magnetic field, with and without radiative cooling on the cavity evolution. Increasing the magnetic field pushes back the TS, while pushing forward the BS. When radiative cooling is included it is found that the TS was pushed forward, while the BS receded, as explained earlier.

In conclusion, it is found that the choice of cooling functions influences the positions of the TS, AP, and BS, as well as the geometric extent of the cavity. This further influences the compression ratio that results from radiative cooling in the cold outer astrosheath. When the ISM magnetic field is included, it reduces the compression ratio of the cold outer astrosheath. Over all it is found that the choice of cooling function is not trivial, and should be considered when including radiative cooling into hydrodynamic or MHD simulations.

Chapter 4

Astrospheric Evolution Including Relative Motion and Radiative Cooling

4.1 Introduction

According to Toalá et al. (2016), runaway stars can move with relative high velocities ($\gtrsim 30\ \mathrm{km\,s^{-1}}$) through the interstellar medium (ISM). These stars move away from stellar associations of which they used to be associated with. Massive stars with relative motion moving supersonically through the interstellar medium produce large scale bow shocks. Many such shocks have been detected in optical, infrared (IR) and radio wavelengths. Two examples of this is shown in Figure 4.1 with, ζ Oph in the left panel, and BD+43° 3654 in the right panel, with a bow shock clearly visible in each example (Toalá et al., 2016).

In this chapter, the study of astrosphere/stellar wind cavity evolution continues, using the same model as in the previous chapter. New in this chapter, is that the effect of relative motion on the evolution of an astrosphere is simulated and results shown. This is done for a pure hydrodynamic case, as well as when the interstellar magnetic field is included. Again the effect of radiative cooling, using the CF1 cooling function, is included in the model and compared to no-cooling scenarios to illustrate the effect of this process on cavity evolution. Results are also compared to the previous chapter, where relative motion is not included. The differences are discussed.

4.2 The Effect of Relative Motion on Cavity Evolution

As mentioned previously, a termination shock (TS) forms when the pressure of a stellar wind (mostly the ram pressure, since the stellar wind is kinetically dominated) balances the pressure of the ISM. However, in this chapter relative motion of the interstellar medium (ISM) is included so that this description becomes more complicated. After the formation of the TS, the stellar wind can no longer stand off the ISM. This implies that the flow of the inner astrosphere (IAS) has to turn around until the streamlines of the shocked wind is parallel with

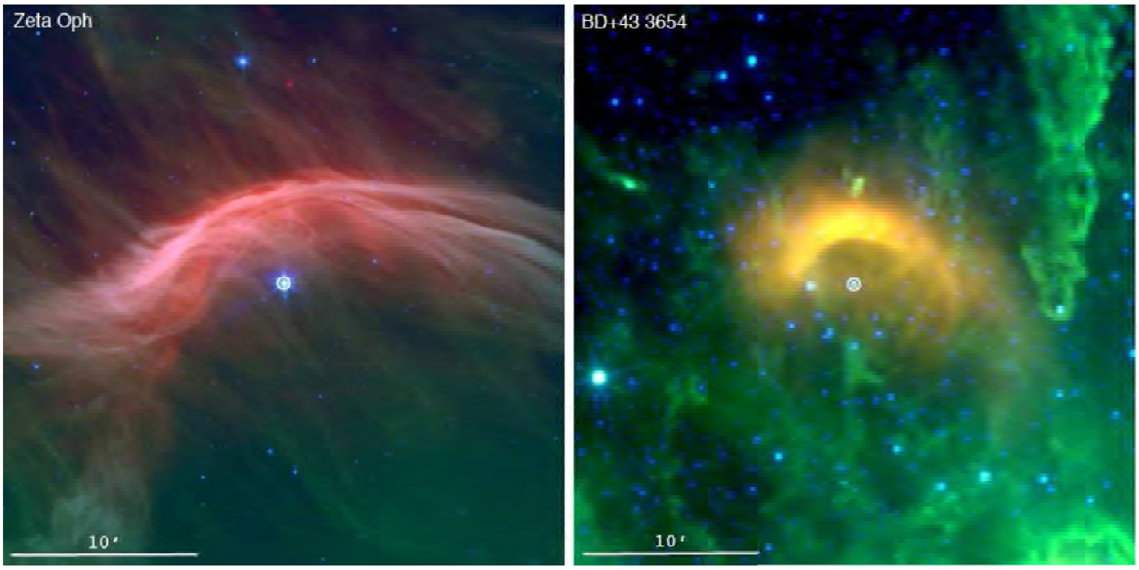

Figure 4.1: Colour-composite mid-IR images of ζ Oph (left panel), and BD+43° 3654 (right panel). Taken from Toalá et al. (2016).

the streamlines of the ISM. This situation is shown in Figure 4.2, and computations is done in spherical coordinates. For this result, a stellar wind with an outflow velocity of 1500 $\mathrm{km\,s^{-1}}$ with a density of $10^{-23.5}$ $\mathrm{g\,cm^{-3}}$ and temperature 10^4 K at an inner boundary of 2.8×10^{-3} pc is assumed for the inner boundary conditions. For the ISM, a density of $10^{-22.5}$ $\mathrm{g\,cm^{-3}}$ and relative speed of 90 $\mathrm{km\,s^{-1}}$, with a temperature of 100 K was assumed. Note that no radiative cooling and no magnetic field is included in this first result. This figure shows the classic result of a pure hydrodynamic model, including relative motion and no radiative cooling. A bullet shaped structure is visible with the nose at 0°, the flanks at 90°, and the tail at 180°.

Since the ISM also has ram pressure, due to relative motion, it is expected that the position of the TS is closer to that of the star (Holzer, 1972) in the nose direction compared to the case where no relative motion is assumed. The results from Figure 4.3 show this to be true, at least for the nose at 0°. This figure shows the computed density profiles for stellar winds without relative motion (shown as the solid line), relative motion of 60 $\mathrm{km\,s^{-1}}$ (shown with a dot-dashed line), and relative motion of 90 $\mathrm{km\,s^{-1}}$ (shown as the dashed line). Results are shown at 40 kyrs. The added ram pressure of the ISM pushes back the TS, and results in a smaller cavity in the nose region. The TS, with relative motion of 90 $\mathrm{km\,s^{-1}}$, is found to be the closest to the star (located at the origin) at $\approx$ 0.2 pc. The TS for a relative velocity of 60 $\mathrm{km\,s^{-1}}$, is found at $\approx$ 0.3 pc, while the TS with no ISM ram pressure, is found to be the furthest from the origin at $\approx$ 0.56 pc.

After the formation of the TS, the kinetic energy of the stellar wind is converted to thermal energy, as discussed in previous chapters. This region is known as the IAS and is responsible for the expansion of the astrosphere, as it does work against the ISM. It is this expansion that creates the BS (as long as it moves supersonically into the ISM). Since it does work against the ISM, increasing the energy of the ISM (in this case adding relative motion or ram pressure)

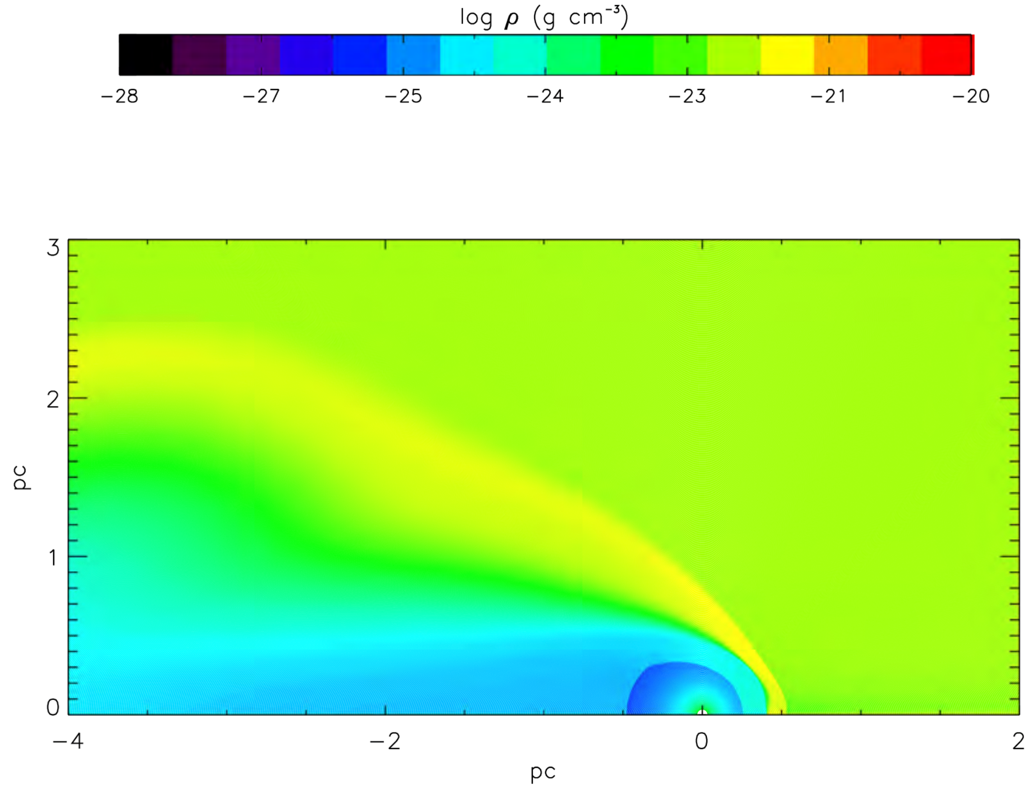

Figure 4.2: A contour plot showing the computed density at 40 kyrs for a pure hydrodynamic model. The effects of radiative cooling is not included, and a relative motion of 90 $\mathrm{km\ s^{-1}}$ is assumed. Note that the model solves in spherical coordinates with an outer boundary at 5 pc radial distance.

would create a more confined IAS, and a BS closer to the origin in the nose direction. This result is also shown in Figure 4.3, with the BS with no relative motion found the furthest from the origin, at ≈ 2.45 pc. For relative motion of 60 $\mathrm{km\ s^{-1}}$, the BS is found at ≈ 0.61 pc, and the relative motion of 90 $\mathrm{km\ s^{-1}}$, closest to the origin at ≈ 0.51 pc. By adding relative motion to the model, the spherical cavity from the previous chapters is now more a bullet-shaped structure. See e.g., Opher et al. (2015), and Pogorelov et al. (2016) for recent simulations of the heliosphere, where the complex 3D structure of the heliosphere is shown.

Since the astropause (AP) separates the region of the stellar wind and the ISM, the system will be decided into two parts. The first is the region of the stellar wind cavity up to the AP. The second is the supersonic ISM that has to navigate past the created cavity. The resulting structure is shown in Figure 4.4 and is taken from Scherer et al. (2016). Earlier work can also be found in e.g. Wallis & Dryer (1976), Liepmann & Roshko (1957) and Ben-Dor (2007).

Figure 4.4 shows a detailed sketch of what structure is to be expected in a astrosphere/stellar wind cavity. Shown here is the ISM with a Mach number larger than one, and relative flow from right to left, resulting in a bow shock. Close to the stagnation line the bow shock (BS) is a perpendicular shock and deaccelerates the ISM to subsonic velocities. Away from the stagnation line the shock becomes oblique, until above what can be called a sonic line (SL), where the shock is weak and the ISM remains supersonic after passing trough the BS.

Now concerning the stellar wind, on the stagnation line, the TS forms a perpendicular shock and deaccelerates the stellar wind to subsonic velocities. Away from the stagnation line, the TS, like the BS, becomes an oblique shock. Above the SL, the oblique shock is also a weak shock, and the stellar wind remains supersonic.

Under certain conditions, a Mach disk (MD) is formed. Together with the Mach disk, a reflected shock (RS) is formed at the triple point (TP), as shown in Figure 4.4. A slipstream extends downstream from the triple point. The reflected shock forms to equalize the pressures on the two sides of the slipstream, which is also a tangential discontinuity.

4.3 The Effect of Radiative Cooling in a Relative Motion Scenario

The result when radiative cooling is included in the model is shown in Figure 4.5 and should be compared to Figure 4.2. All parameters are the same, the only difference being that radiative cooling is included. As discussed in previous chapters, the astrosphere is somewhat smaller when compared to Figure 4.2, when cooling is included. The outer astrosheath (OAS) cools and becomes a thin, highly compressed shell. The IAS and stellar wind does not cool and can expand further, resulting in the position of the TS to be further away from the star.

These results are now more quantitative compared to Figure 4.6, which shows the computed radial density profile for cooling and no-cooling scenarios. The density profiles for 0° (on the stagnation line or in the nose) is shown with a dot-dash line when radiative cooling is included, and a dashed line when it is not. The density profile for 180° (tail) is shown as a solid line when radiative cooling is included, and a dot-dot-dot-dashed line when it is not. As shown, the relative motion results in an asymmetry in TS and AP distance.

The solid and dot-dashed line in Figure 4.6 show the results when radiative cooling is included. On the stagnation line (dot dash-line) the expected thin, compressed OAS is found with a compression ratio much larger then 4. This result corresponds with what is found in previous chapters. The solid line (for 180°) differs from that of dot-dot-dot-dashed line (without radiative cooling). The downstream TS is pushed further away from the star, compared to the corresponding result without radiative cooling. The TS for the downstream result is found at $\approx$ 0.5 pc, while the corresponding result with radiative cooling included is found at $\approx$ 1.1 pc.

Shown in Figures 4.7 and 4.8 are contour plots of the computed density as function of time and distance, showing the evolution of the AP and TS. Relative motion of $30\ \mathrm{km\ s^{-1}}$ is included. Figure 4.7 shows the results without considering the effect of radiative cooling, while Figure 4.8 shows the results when radiative cooling is considered. The results are only shown along the nose of the cavity.

The TS for the case without radiative cooling (Figure 4.7) reaches a maximum distance of just over 0.6 pc at 100 kyrs. The BS reaches a maximum distance of $\approx$ 1.5 pc at a time of 100 kyrs.

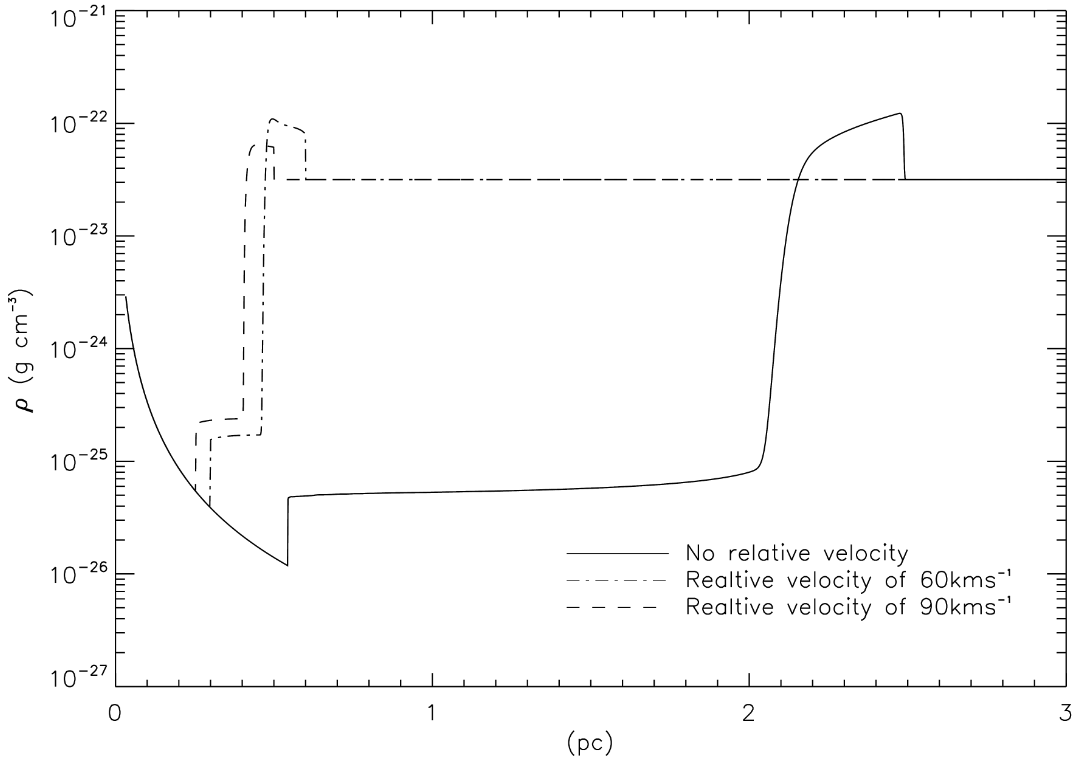

Figure 4.3: The computed radial density profiles in the nose or 0^o direction at 40 kyrs for the pure HD model. The scenario without relative motion is shown with a solid line, relative motion of $60\ \mathrm{km\,s^{-1}}$ is shown with a dot-dashed line, and relative motion of $90\ \mathrm{km\,s^{-1}}$ shown with dashed line. Radiative cooling is not included.

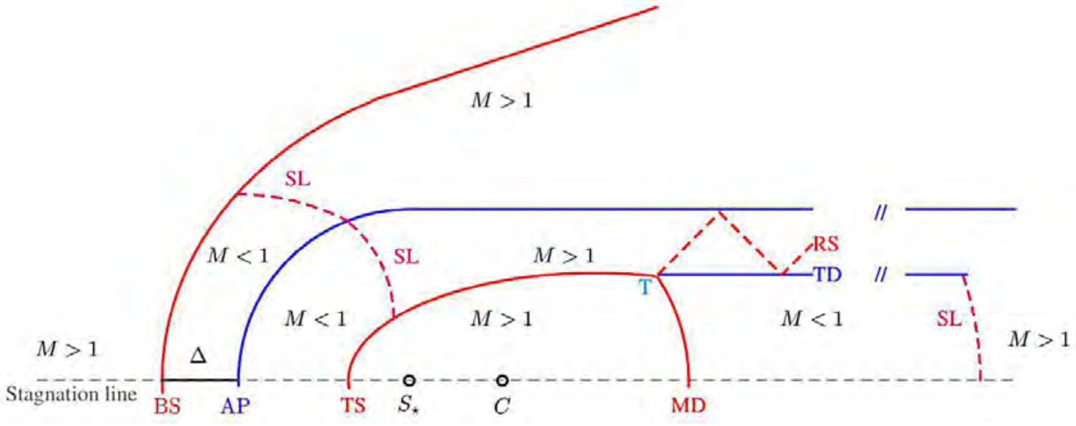

Figure 4.4: The resulting structure of an astrosphere/stellar wind. Taken from Scherer et al. (2016).

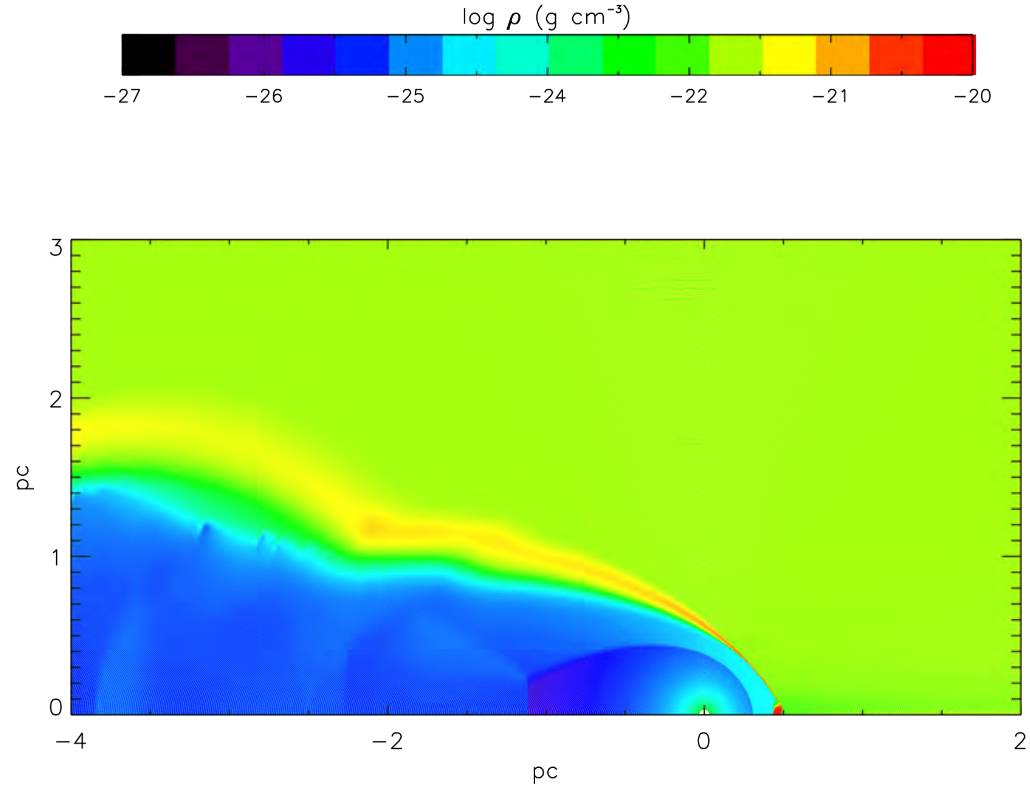

Figure 4.5: The computed density contour at 40 kyrs for the HD model. The effects of radiative cooling, using the cooling function from Mellema & Lundqvist (2002), is now included with a relative motion of $90\ \mathrm{km\ s^{-1}}$ assumed.

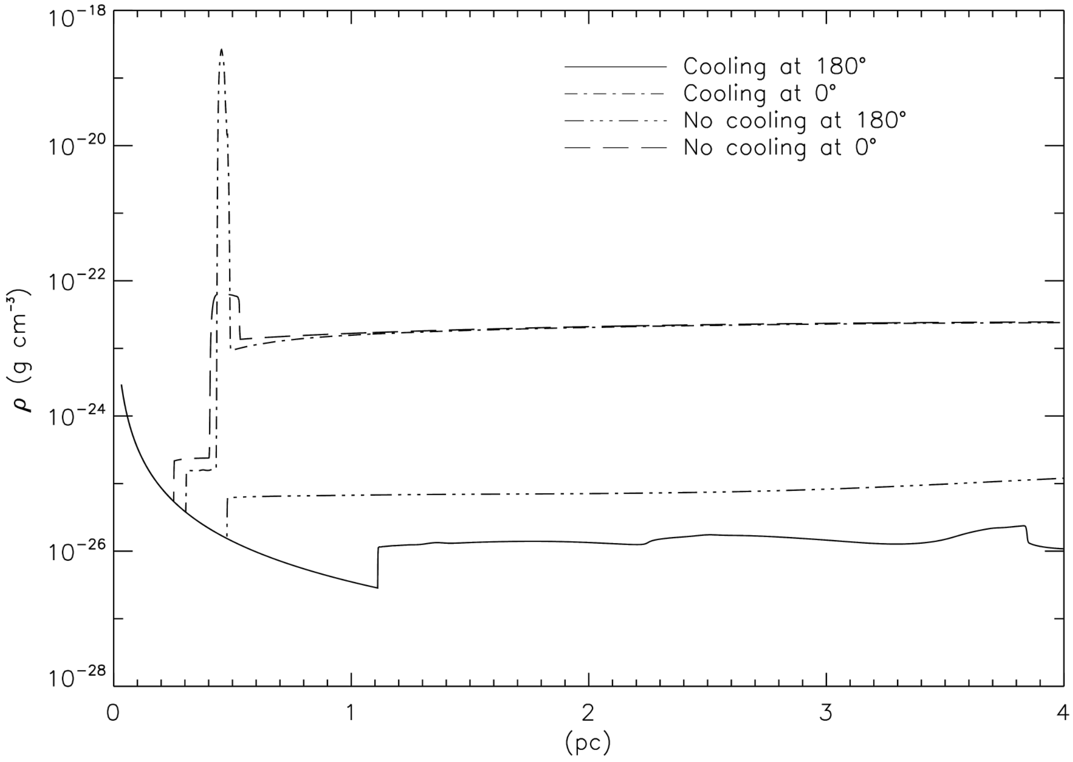

Figure 4.6: The computed radial density profiles at 40 kyrs for the pure hydrodynamic model with relative motion of $90\ \mathrm{km\ s^{-1}}$ assumed in the model. Results are shown for 0° (on the stagnation line) and is shown with a dot-dash line when radiative cooling is included, and a dashed line when it is not. The density profile for 180° (downstream) is shown as a solid line when radiative cooling is included, and a dot-dot-dot-dashed line when it is not.

When radiative cooling is taken into account in Figure 4.8, the TS is found at a maximum distance closer to 0.7 pc. The OAS, however, shows some dramatic effects. The OAS is much more compressed and extends only to just over 1 pc, when radiative cooling is included. This indicates that the BS is extremely radiative, probably as a result of it being slowed down considerably by the relative motion.

4.4 The Effect of the Interstellar Magnetic Field

To illustrate the effect of an ISM magnetic field on computations a magnetic field of 3 μG is now included in the model. The effect of radiative cooling is also included and results are also shown without. Note that since these simulations are done only in 2D, it is assumed than an azimuthal ISM magnetic field is found around the star. This is, however, not realistic, but it shows maximum effects, since the field is always perpendicular to the outflow.

Figure 4.9 shows the computed density contour with an ISM magnetic field of 3 μG and relative motion of $90\ \mathrm{km\,s^{-1}}$, when no radiative cooling is included. When compared to the result without a magnetic field (Figure 4.2), it is seen that the extent of the IAS is slightly less than that of Figure 4.2, while the opposite is true for the OAS. This is the result of the ISM magnetic field pressure, as explained in Chapter 3.

Figure 4.10 shows the corresponding computed radial density profiles for 0° (on the stagnation line), and 180° (downstream) for results with and without radiative cooling. The solid line shows the result with radiative cooling included at 180°, while the dot-dot-dot-dashed line show the result for when it is not. The result with radiative cooling at 0° (stagnation line) is shown with dot-dashed line, while the dashed line shows the result without radiative cooling.

Comparison of the cooled downstream density profile (solid line) of Figure 4.10 (with the ISM magnetic field included), with that corresponding to Figure 4.6 (without the ISM magnetic field), shows that the OAS of the former is thicker (when the ISM magnetic field is taken into account) and less dense than that of the last mentioned. Furthermore, the TS is closer to the star. This is the influence of the ISM magnetic field, where the magnetic pressure works against the expansion of the SW and the IAS. It, however, assists in the expansion of the OAS, as described in Chapter 3. As stated earlier, when cooling is implemented, the magnetic field counteracts the compression. This counter-action decreases the density, making the cooling less effective, assuming that the magnetic pressure is larger then the thermal pressure.

In the downstream region the results with radiative (solid line) cooling show the TS to be further away from the star compared to the result without radiative cooling (dot-dot-dot-dashed line). This is the result of the drop in thermal pressure of the BS, resulting from radiative cooling, as explained before, as well as the inclusion of relative motion sweeping the structure downstream. Here, as in Figure 4.6 when radiative cooling is included, a SL forms in the downstream region (see Figure 4.4), which is not yet present in the results without radiative

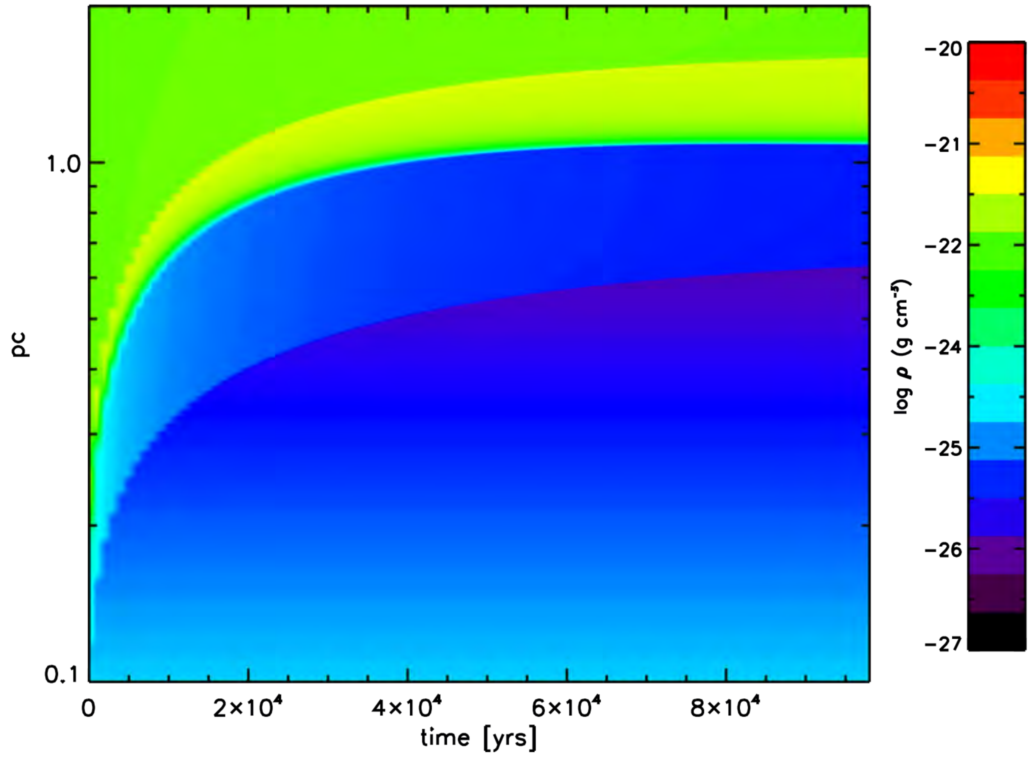

Figure 4.7: Contour plot showing the evolution of an astrosphere in terms of density as function of time and distance. Results are shown are shown at 0^o, along the stagnation line in the nose direction, and shows the evolution of the AP and TS. Relative velocity of 30 km s^{-1} is assumed in the model, while radiative cooling is not included. The results are only considered in the nose of the cavity.

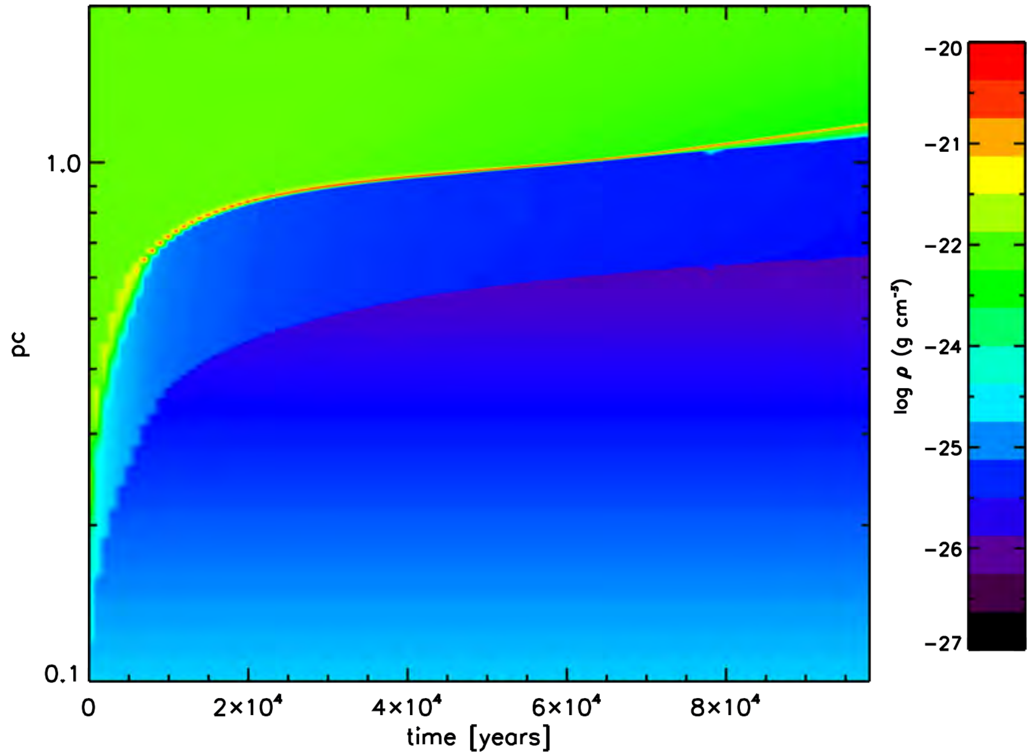

Figure 4.8: The same as Figure 4.7, but with radiative cooling included.

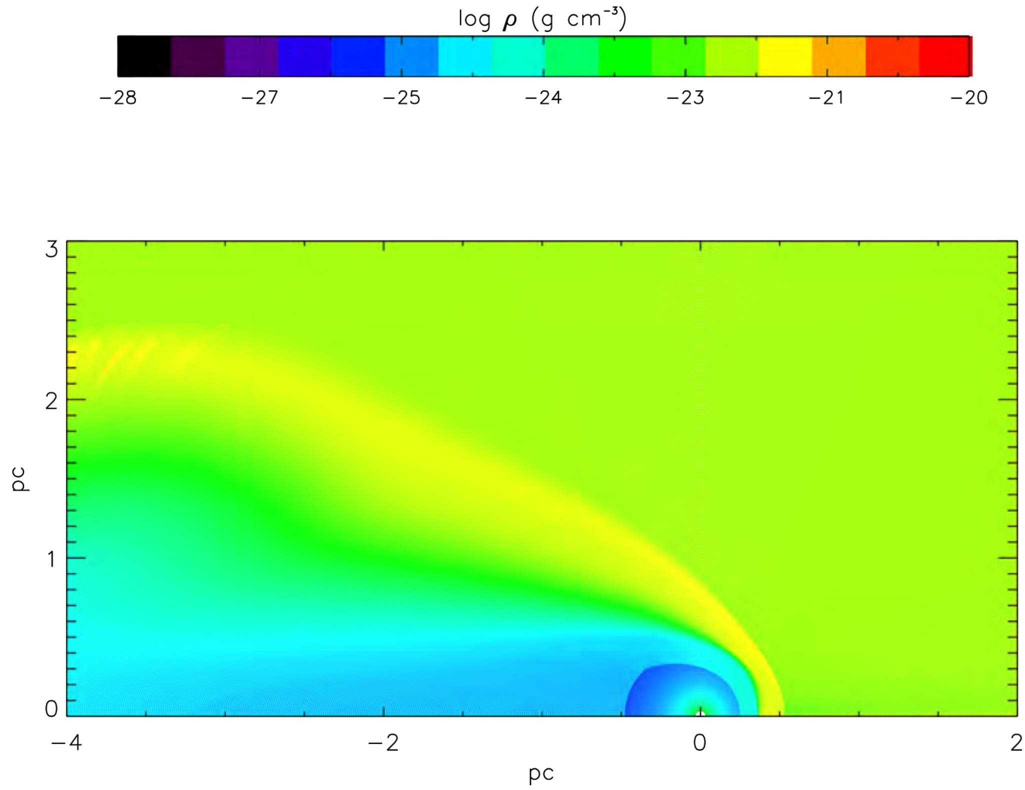

Figure 4.9: The computed density contours at 40 kyrs with a magnetic field of 3 μG assumed in the model. The effects of radiative cooling is not included, and relative motion of 90 km s^{-1} is assumed.

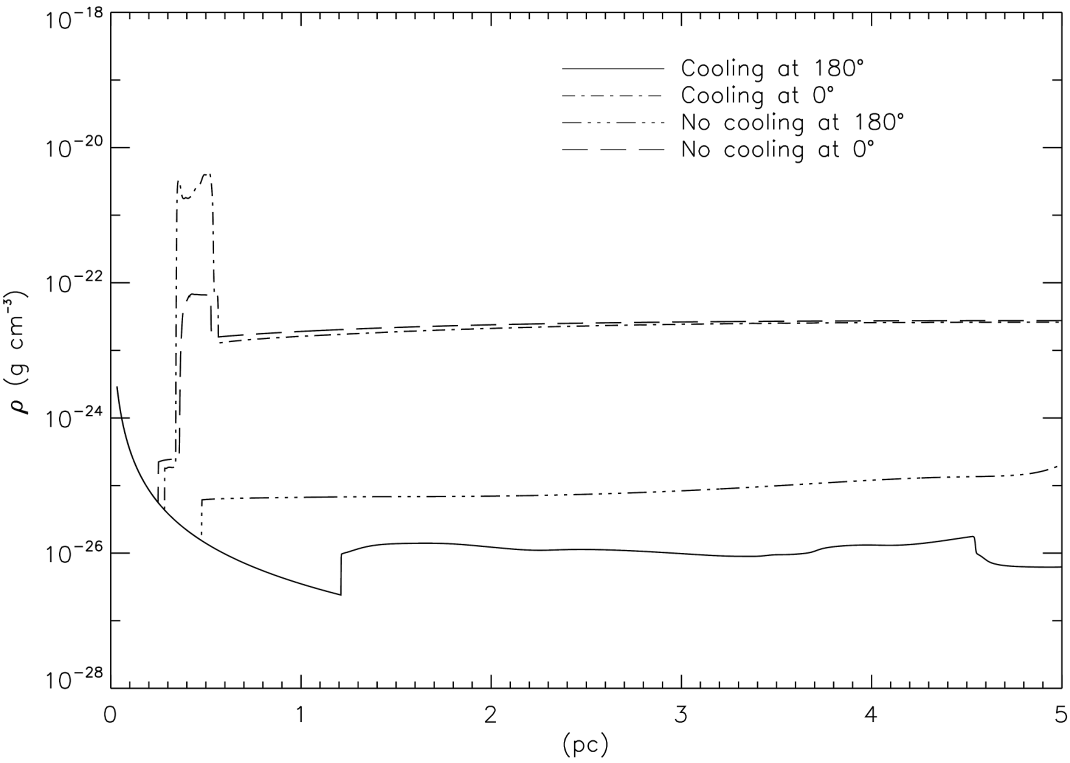

Figure 4.10: The same as Figure 4.6, with a 3 μG ISM magnetic field included.

cooling. After the SL the density drops. This is not seen in the corresponding result when radiative cooling is not included; instead the density remains constant after the formation of the TS.

Figure 4.11 shows the computed radial density profiles, with no relative motion shown with a solid line, relative velocity of 60 $\mathrm{km\,s^{-1}}$ shown with a dash-dot line, and relative velocity of 90 $\mathrm{km\,s^{-1}}$ shown with a dashed line. An ISM magnetic field of 3 μG is also included while radiative cooling is not taken into account. When compared to Figure 4.3, clear differences can be seen. In Figure 4.11, for the case with no relative motion, the solid line, shows that density pile up has occurred in the nose along the BS, while the TS shock has been pushed slightly back. This is a result of the added ISM magnetic field, adding magnetic pressure to the ISM, forcing the stellar wind to be shocked earlier when it has higher ram pressure to balance the ISM pressure.

The OAS for the cases with relative motion in Figure 4.11 is slightly less dense than the corresponding results of Figure 4.3. This is a result of the ISM magnetic field resisting the compression of the BS. The pile up found in the BS, as shown in Figure 4.11, for the case without relative motion (solid line), shows an increase in the OAS density. The OAS region of the results with the ISM magnetic field is also larger than the corresponding result without; this is the result of the ISM magnetic pressure that expands the OAS, resulting in a decrease in density while pushing out the BS. The OAS of the results with relative motion in Figure 4.3 is also found to be closer to the origin, whereas, in Figure 4.11, with the ISM magnetic field included, the OAS is found further outward.

Figure 4.12 shows the computed radial density profiles with radiative cooling and a 3 μG ISM magnetic field with relative motion. Here the OAS of the density profile with relative motion of 90 $\mathrm{km\,s^{-1}}$ is found to be thicker than the OAS with relative motion of 60 $\mathrm{km\,s^{-1}}$. It is possible that the result with relative motion of 90 $\mathrm{km\,s^{-1}}$ has already cooled, due to the slower velocity of the BS lowering the cooling time; allowing the magnetic pressure to dominate and expanding the OAS. The velocity dependence of the cooling time is demonstrated in Chapter 3, while the effects of the ISM magnetic field is shown in Chapter 3. The densities of the OAS from the results with radiative cooling, Figure 4.12, are much higher than those from the results with radiative cooling not considered. This corresponds with what was found from previous chapters.

The OAS region of the three density profiles are smaller than the corresponding results of Figure 4.11, which is a result of the drop in thermal pressure from radiative cooling. The TS from the result without relative motion, together with relative motion of 90 $\mathrm{km\,s^{-1}}$ of Figure 4.12, are found to be further out than the corresponding results from Figure 4.11. This is to be expected, since the drop in thermal pressure resulting from radiative cooling in the OAS reduces the pressure the TS has to push back, and can therefore move further out. This result agrees with those from previous chapters.

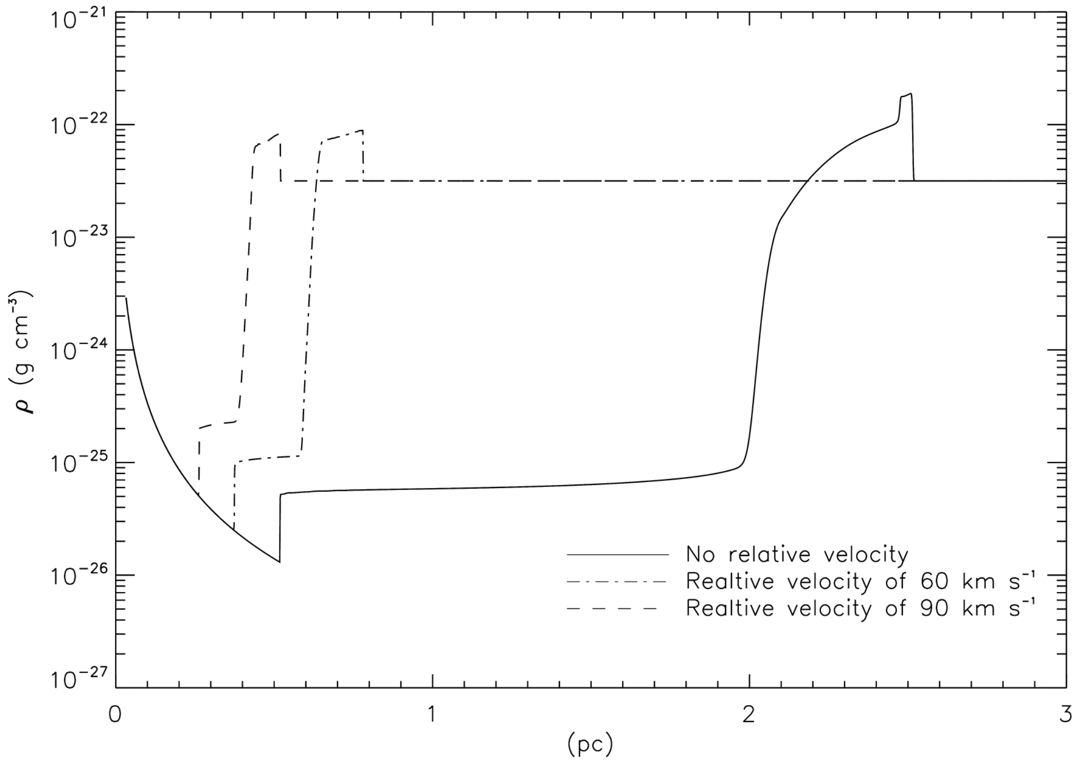

Figure 4.11: The computed radial density profiles at 40 kyrs for a model with an ISM magnetic field of 3 μG, without radiative cooling. The result without relative velocity is shown with a solid line, a relative velocity of $60\ \mathrm{km\ s^{-1}}$ is shown with a dot-dashed line, and the result with a relative velocity of $90\ \mathrm{km\ s^{-1}}$ is shown with a dashed line.

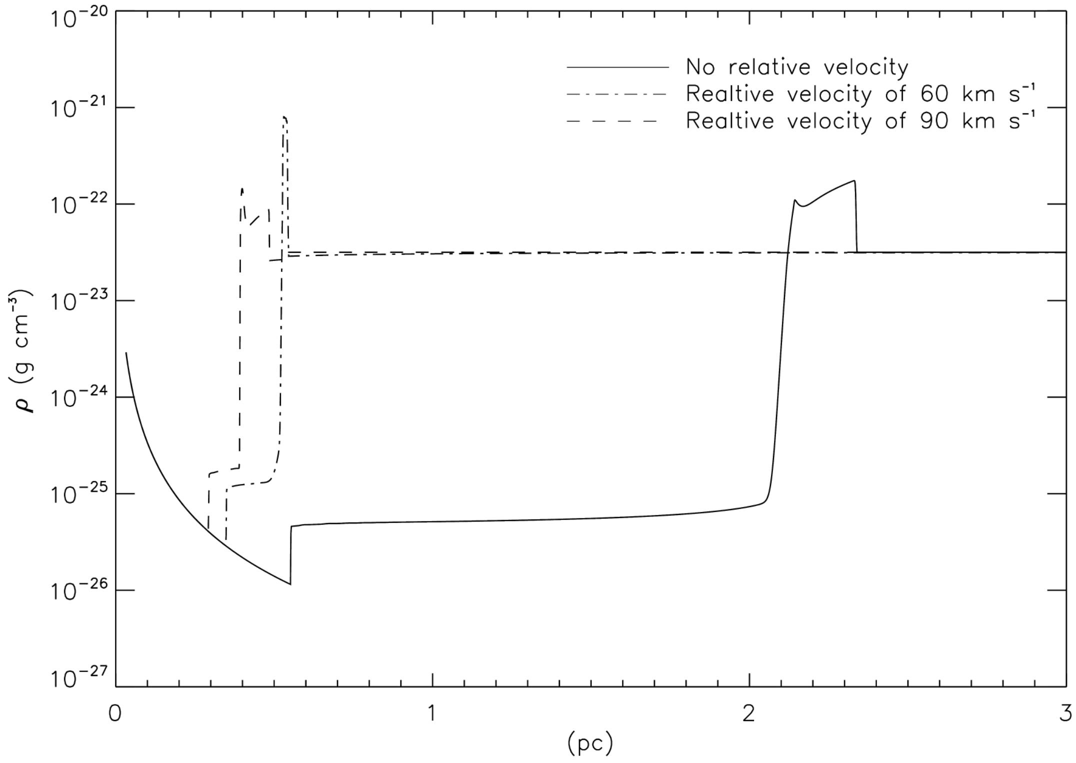

Figure 4.12: The same as Figure 4.11, but with radiative cooling included.

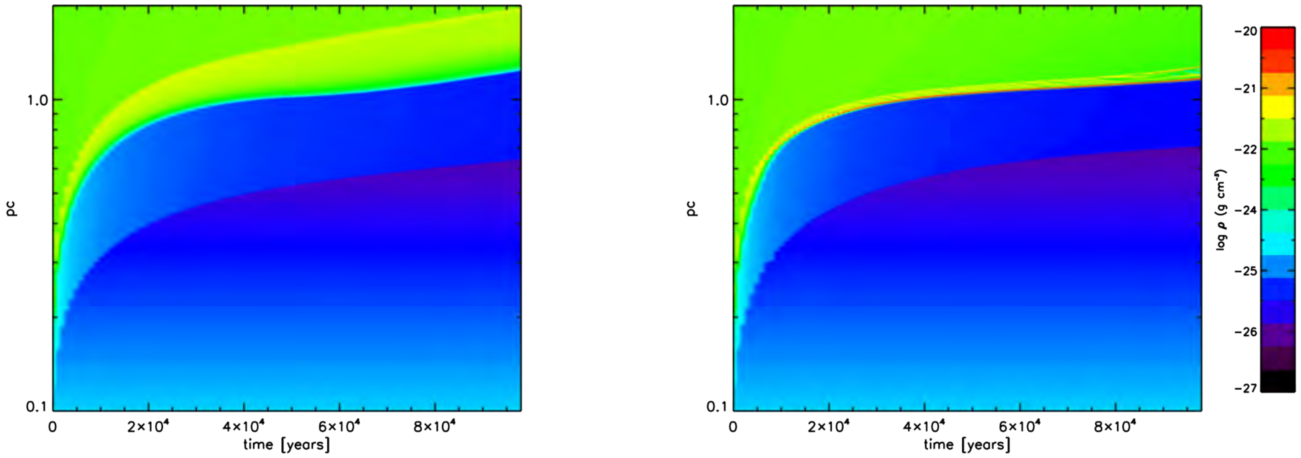

Figure 4.13: Contour plots of density as a function of time and distance, showing the evolution of the TS and AP. A relative velocity of $30\ \mathrm{km\ s^{-1}}$ is included, while radiative cooling is not included in the left pane. The results with radiative cooling, included in the calculations, is shown on the panel on the right. An ISM magnetic field of 3 μG is included. The results are shown along the nose of the cavity.

Figure 4.13 shows contour plots of density as a function of time and distance in the nose direction, showing the evolution of the AP and TS. Relative motion of $30\ \mathrm{km\ s^{-1}}$ is included, as well as an ISM magnetic field of 3 μG. The panel on the left shows the computed results without radiative cooling, while the panel on the left shows the results when radiative cooling is included.

The left panel of Figure 4.13 (the results without radiative cooling) shows that the TS reaches a maximum distance of just over 0.6 pc at the maximum time of 100 kyrs. The BS is found at 2 pc at the maximum time of 100 kyrs.

When radiative cooling is included, the panel on the right of Figure 4.13, the TS is found at 0.7 pc at 100 kyrs. The BS is found at just over 1 pc, and is similar to Figure 4.8, more compressed. This is again due to the BS being extremely radiative, due to its decreased velocity, which in turn is a result of the relative motion. The OAS is in both cases not as compressed as it is in Figure 4.8, and is again a result of the ISM magnetic field, as explained in earlier chapters.

The effect of radiative cooling and the ISM magnetic pressure is summarized in Figure 4.14. This figure shows the computed compression ratio of the BS as a function of time for the cases of relative motion of $30\ \mathrm{km\ s^{-1}}$. The compression ratio for the result without radiative cooling is shown with a solid line, while the result with radiative cooling included is shown with a dashed line. The case with radiative cooling and an ISM magnetic field of 3 μG is shown with a dot-dashed line.

For the case with relative motion of 30 km s^{-1}, and without radiative cooling, or an ISM magnetic field (solid line), shows that the compression ratio remains at a value of ≈ 4. This is the expected result for an adiabatic index of $5/3$. When radiative cooling is included (dashed line) the compression ratio increases suddenly to ≈ 20 at about 10 kyrs. The compression ratio then

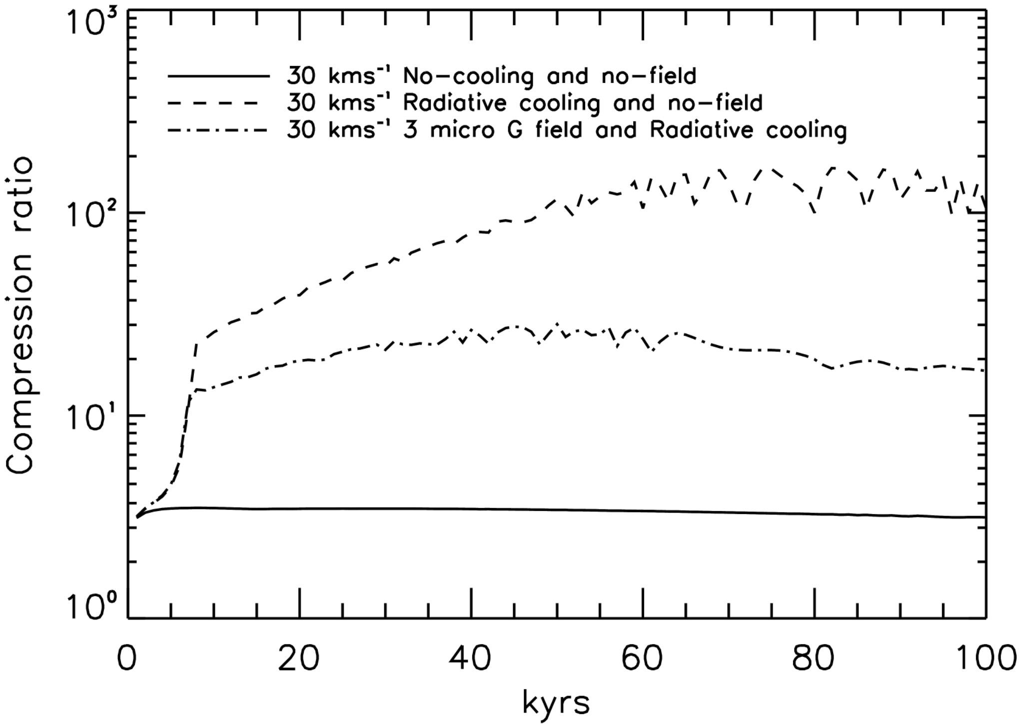

Figure 4.14: The computed compression ratio of the OAS for relative motion of 30 $\mathrm{km\,s^{-1}}$. The compression without the inclusion of radiative cooling, or magnetic pressure, is shown with a solid line. The compression ratio with the inclusion of radiative cooling and no magnetic pressure is shown with a dashed line, while the results for an ISM magnetic field of 3 μG with radiative cooling is shown with a dot-dashed line. All the results are shown for the nose region.

increases steadily to a maximum value of almost $\approx$ 110 at around 70 kyrs, before dropping to a value of $\approx$ 100 at 100 kyrs. The compression ratio also becomes unstable at $\approx$ 40 kyrs, possibly due to the cooling instability.

For the result with the 3 μG ISM magnetic field and radiative cooling (dot-dashed line), it is found that the early behaviour is similar to that of the result with radiative cooling (dashed line). However, the compression ratio reaches a maximum of over $\approx$ 20 and decreases slowly thereafter. Figure 4.14 illustrates the importance of including radiative cooling and ISM magnetic pressure in a model. The compression ratio when the magnetic field is included is also considerably less than for results with no magnetic field (dashed line). This is consistent with what is found previously namely, that the magnetic field resists the compression caused by radiative cooling.

4.5 Summary and Conclusions

The inclusion of relative motion of a star results in a bullet shaped structure of its cavity, as shown in Figure 4.2. The addition of ram pressure of relative motion pushes back the termination shock (TS) and astropause (AP). The bullet shaped cavity can be devided into two parts. The first part is the free expanding supersonic stellar wind. This wind is shocked at the TS, resulting in the IAS that expands adiabatically into the ISM. Depending on background parameters this expansion creates a BS, if it expands supersonically into the ISM. The BS creates the OAS, consisting of shocked ISM material.

A complex structure is created downwind of the star, known as the astrotail. The ISM has to navigate past the cavity created by the stellar wind, and if it moves supersonically, it will create a BS. Including radiative cooling with relative motion, results in the Mach disk (MD) being able to move further downstream. This is caused by the drop in thermal pressure of the OAS when radiative cooling is included.

Including an ISM magnetic field, increases the extent of the OAS, and is caused by the additional magnetic pressure. The TS is closer to the star, again a result from the added magnetic pressure. When radiative cooling is included, the TS moves further away from the star, and the OAS thickness is also reduced. This is again a result of the drop in the thermal pressure of the OAS, caused by radiative cooling.

Adding relative motion with the ISM magnetic field could decrease the shock velocity, decreasing the cooling time, and resulting in more cooling. When the magnetic pressure of the OAS starts to dominate, the OAS will expand.

The long term behaviour of the compression ratio, and a summary of the results when relative motion (of 30 km s^{-1}) is included in the model is shown in Figure 4.14. As shown, the compression ratio remains constant when there is no radiative cooling and no ISM magnetic field. The compression ratio increases when radiative cooling is included, reaching a value of ≈ 120 at 70 kyrs, before decreasing slowly to ≈ 100 at 100 kyrs. When the ISM magnetic field is included with radiative cooling, it is found that the compression ratio is considerably less, reaching values of ≈ 20, indicating that the ISM magnetic field reduces the efficiency of radiative cooling. This could be, as found previously, because the magnetic field resists the compression caused by radiative cooling.

Chapter 5

Supernova Remnant Evolution in Astrosphere/Stellar Wind Cavities

5.1 Introduction

The end of a massive star, typically with mass $M \geq 8M_{\odot}$ (e.g. Cho & Kang, 2008), is marked by a sudden release of energy that creates, for a moment, a very bright object in the sky that slowly fades after a couple of months. This is known as a supernova and is a result of core collapse. This creates an explosion that typically releases about 10^{51} ergs of kinetic energy in the form of a blast wave that moves trough the interstellar medium (ISM), and is known as a Super Nova Remnant (SNR) (e.g. Franco et al., 1991, Dwarkadas, 2005).

A supernova chemically enriches the surrounding ISM, while supernova remnants (SNRs) are considered to be the main contributors of galactic cosmic rays up to $\approx 10^{15}$ eV (e.g. Falle, 1981, Bell, 2013, Broersen et al., 2014). A review of astrophysical blast waves is given by Sedov (1977) and Ostriker & McKee (1988). An example of a SNR is shown in Figure 5.1 which is taken from Broersen et al. (2014). The SNR is located close to a cluster of B type stars, and it is speculated by Williams et al. (2011) that this particular SNR is a result of type 1a explosion (supernova occurring in a binary system consisting of a white dwarf and a second object ranging from a white dwarf to a giant star) . The spherical structure of the SNR is clearly visible.

The aim of this chapter is to present simulations of stellar wind cavities and SNR evolution in these and beyond. The effect of a pre-existing cavity on SNR evolution, as well as SNR evolution inside a uniform ISM is shown. The effect of including radiative cooling using the CF1 cooling function in the model is also investigated and its effect on calculations shown. The same numerical model, as discussed in the previous chapters is used, including the pressure of the magnetic field for certain simulations.

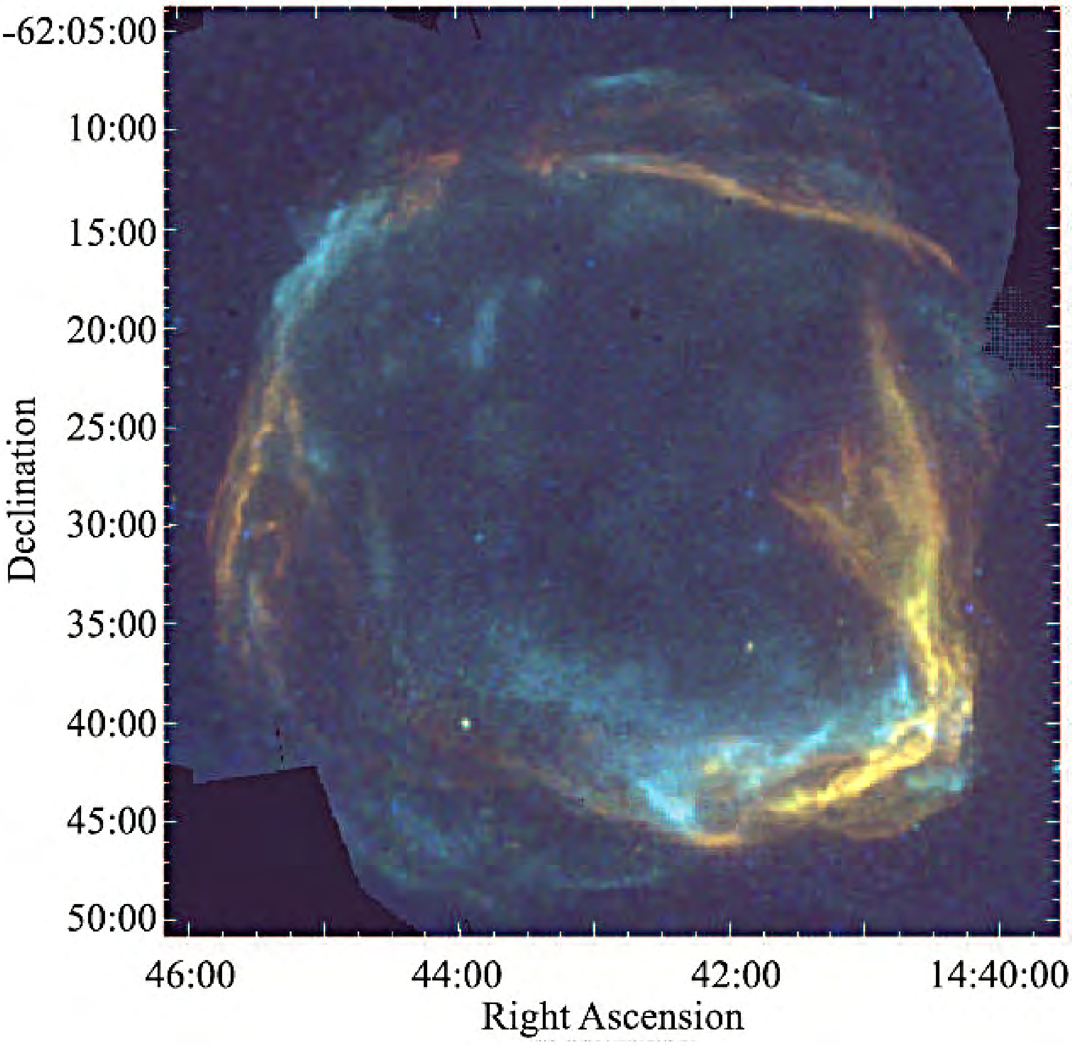

Figure 5.1: A three colour image of RCW 86. The red, green, and blue colours denote $0.5 - 1.0$ keV, 1.0 -1.95 keV, and 2.0-5.0 keV, respectively. Taken from Broersen et al. (2014).

5.2 Supernova Evolution

A description of the evolution of SNRs can be found in Woltjer (1972) and is briefly discussed here. It is assumed, for now in the model, that there does not exist a blown out cavity caused by the progenitors. The SNR blast wave moves into the undisturbed and uniform ISM. The effects of relativistic particles and magnetic fields are also neglected. In the evolution of a SNR, different stages can be identified as the ejecta dominated phase, Sedov-Taylor phase, and lastly the snowplow phase. These stages are briefly discussed below.

5.2.1 Ejecta Dominated Stage

In this stage, the swept-up matter is of little importance, or

$$M_{ej} >> \frac{4\pi\rho_0 R^3}{3}, \tag{5.1}$$

where M_{ej} is the mass being injected into the ISM with density ρ_0. Here the evolution of the explosion is dependent on the initial assumptions (e.g. van der Swaluw et al., 2001, Ferreira & de Jager, 2008). For modelling purposes, one can assume as boundary conditions for this ejecta dominated early stage, a spherical region with radius r_{ej}, and high constant density ρ_{ej} with a radially increasing velocity profile (e.g. van der Swaluw et al., 2001, Ferreira & de Jager, 2008)

$$v = \frac{r}{t} = \frac{v_{ej} r}{r_{ej}}, \tag{5.2}$$

where r_{ej} is assumed to be 4.85×10^{-4} pc and v_{ej}

$$v_{ej} = \sqrt{\frac{10E_{ej}}{3M_{ej}}}. \tag{5.3}$$

For the density

$$\rho_{ej} = \frac{3M_{ej}}{4\pi r_{ej}^3}. \tag{5.4}$$

Here E_{ej} is given as the typical value of 10^{51} ergs, while in this work $M_{ej} = 20M_{\odot}$, making it a type II supernova, resulting from core collapse of a massive star. See Ferreira & de Jager (2008) and references therein for SNR simulations corresponding to different values of ρ_{ej}, v_{ej}, and M_{ej}.

In the ejecta dominated stage the density of the ejecta is much larger than that of the ISM and the SNR is freely expanding. Initially the only shock that has formed is the forward shock (FS). The density is proportional to t^{-3} as the ejecta expands adiabatically (e.g. McKee, 1974, McKee & Truelove, 1995). After some time the thermal pressure of the shocked ISM becomes greater than that of the ejecta. This results in a second shock, known as the reverse shock (RS), which is driven back into the ejecta (McKee & Truelove, 1995). This RS decelerates and heats the ejecta and drives mass back into the remnant.

Figure 5.2 (from Ferreira & de Jager, 2008) shows a typical example of the evolution of a SNR at different stages using $E_{ej} = 10^{51}$ erg, $M_{ej} = 3M_{\odot} = 6 \times 10^{33}$ g and an ISM density of 0.9×10^{-24} g cm^{-3}, without including radiative cooling. The top panel shows the ISM magnetic field (perpendicular to the flow) which gets compressed by the FS by factor of ≈ 4.

The second panel in Figure 5.2 shows the density. Here the RS, the contact discontinuity between the ejected and shocked ISM, and the blast wave or FS can be seen. The FS, propagating into the undisturbed ISM, can also be seen. The RS and FS positions are indicated by vertical dashed lines in the density profile. It is shown that, for the parameters used in Ferreira & de

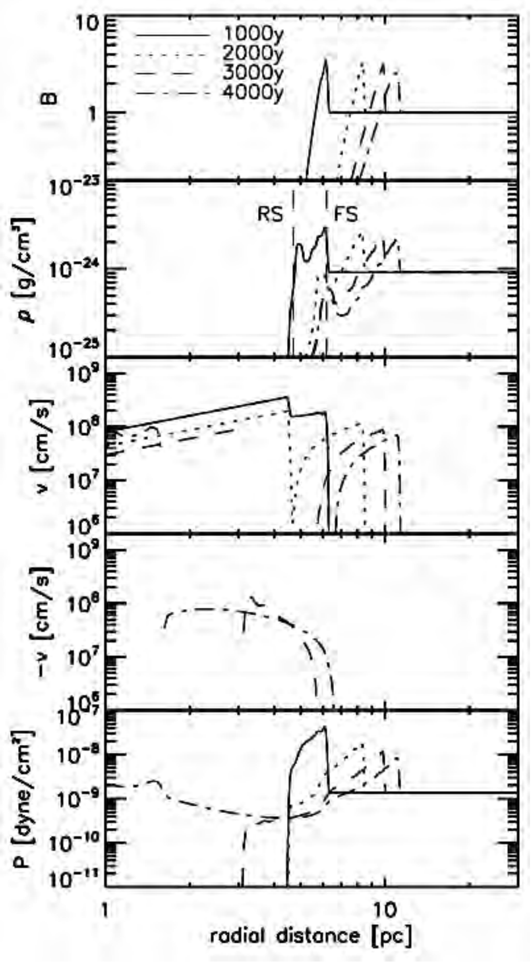

Figure 5.2: The evolution of a typical SNR where the results are shown from 1 to 4 kyrs without radiative cooling. Shown in the top panel is the ISM magnetic field (perpendicular to the flow). The density profile is shown in the second panel, where the positions of the RS and the FS is marked with a vertical dashed line. The velocity, v, is shown on a logarithmic scale, while the reverse velocity ($-v$) is shown just below it. The last panel or bottom panel shows the thermal pressure, here marked as P. Taken from Ferreira & de Jager (2008)

Jager (2008), that the swept up mass of the material is comparable to the ejected mass at ≈ 1 kyrs. As time increases the swept up mass becomes much larger than the ejecta mass and the SNR enters the Sedov-Taylor phase where the FS radius increases as $t^{2/5}$.

The third panel shows the velocity, v, on a logarithmic scale, while the reverse velocity (denoted here as $-v$) is shown in the fourth panel. At some time the RS will change direction and move backward towards the center or origin. In Figure 5.2 it is shown that at 4 kyrs the RS has reached the origin. The bottom panel shows the thermal pressure, here denoted as P. The thermal pressure shows that, as the RS propagates backward towards the origin and through the ejecta, the ejecta is heated.

Figure 5.3 (from Ferreira & de Jager, 2008) shows the FS (top panel) and RS (bottom panel) as a function of time for similar simulations as in Figure 5.2. Shown are different scenarios corresponding to a SNR expanding in an ISM of different densities, with the ISM densities considered ranging from 10^{-27} g cm^{-3} to 10^{-23} g cm^{-3}. The left panels show the SNR where $M_{ej} = 3M_{\odot}$, $M_{ej} = 2M_{\odot}$ for the middle panel, and $M_{ej} = M_{\odot}$ for the panel on the right. The dotted line in the upper left panel shows the Sedov-Taylor solution, where the FS radius increases as $t^{2/5}$.

Ferreira & de Jager (2008) finds the FS radius to be dependent on the ISM density, with larger densities leading to a smaller FS radius when compared to lesser densities for the same simulation time. It is also found that the ejecta mass, M_{ej}, does not play a large role in the determination of the FS radius, especially for times close to the end of the simulation. This is because after a few hundred years the mass of the swept up material is comparable or higher than the ejecta mass. This is not the result in the first couple of hundred years, where this quantity results in a different initial speed (see Equation 5.3) and may influence the transition time from a free expansion to a adiabatic phase.

The bottom panels of Figure 5.3 (from Ferreira & de Jager, 2008) show that the RS radius, and the time for it to return to the origin, is very dependent on both the ISM density and M_{ej}. For a large ISM density the SNR evolves sooner into the Sedov-Taylor phase (by comparison to the computed FS radius in the upper left panel to the dotted lines). This is also the case for a smaller M_{ej}, which will lead to a smaller pressure of the ejecta material. Figure 5.3 shows that the density of the ISM is an important parameter determining the RS radius and the return time to the origin.

The evolution of a young SNR is shown in Figure 5.4. Shown here are modelled results showing the evolution of a SNR in the form of density contour plots of density on a log scale from 1.15 kyrs to 1.4 kyrs for a uniform density ISM. No relative motion or magnetic field, and no pre-existing cavity are assumed in the model for now. The reverse shock becomes important when the mass swept up by the forward shock, the shocked ISM, becomes comparable to that of the ejecta mass. Figure 5.4 shows that all mass initially moves outward from 1.15 kyrs to 1.25 kyrs, as shown by the blue contours representing low density, after which it starts to be driven back into the ejecta at 1.3 kyrs. This is consistent with McKee & Truelove (1995). The ejecta dominated phase ends after the formation of the RS.

5.2.2 Sedov-Taylor Phase

This phase occurs at a later stage when

$$M_{ej} << \frac{4\pi\rho_0 R^3}{3}, \tag{5.5}$$

that is to say the SNR is now dominated by swept-up matter, and the RS has already reached the center of the SNR. The ejecta has been heated by the RS and pressure of the SNR is still much larger than that of the ISM (e.g. Draine, 2011). Radiative losses are negligible and the energy is therefore conserved. The explosion can be treated as a point explosion by injecting

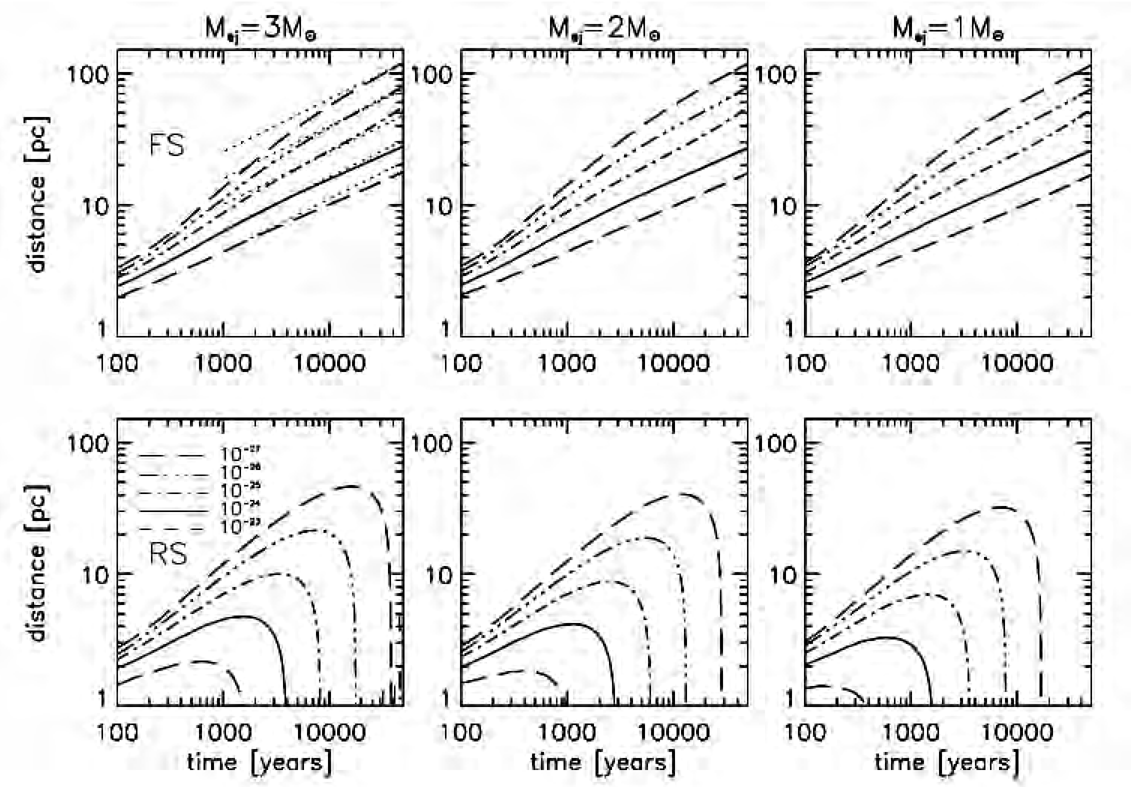

Figure 5.3: The computed FS (top panel) and RS (bottom panel) radius as a function of time on a logarithmic scale with radiative cooling not included. Different scenarios are shown for a SNR expanding in an ISM of different densities from 10^{-27} g cm^{-3} to 10^{-23} g cm^{-3}. The left panels show the SNR where $M_{ej} = 3M_\odot$, $M_{ej} = 2M_\odot$ for the middle panel, and $M_{ej} = M_\odot$ for the panel on the right. Taken from Ferreira & de Jager (2008).

energy E_{ej} into a zero temperature medium with density ρ_0. Then, according to Woltjer (1972), the radius of the shock for a ratio of specific heats 5/3 is given as

$$R = 1.17 \left(\frac{E_{ej}}{\rho_0}\right)^{1/5} t^{2/5} \tag{5.6}$$

while the shock velocity is

$$v_s = \frac{2R}{5t}. \tag{5.7}$$

Radiative cooling in this stage becomes increasingly important as the shock slows down and results in the decreasing of the cooling time.

5.2.3 The Snowplow Phase

This phase occurs when the dynamical time of the SNR is larger than the cooling time. The gas just behind the shock cools quickly and according to Falle (1981) this can create additional shocks. The hot gas in the interior has not cooled, forcing the SNR to continue its expansion.

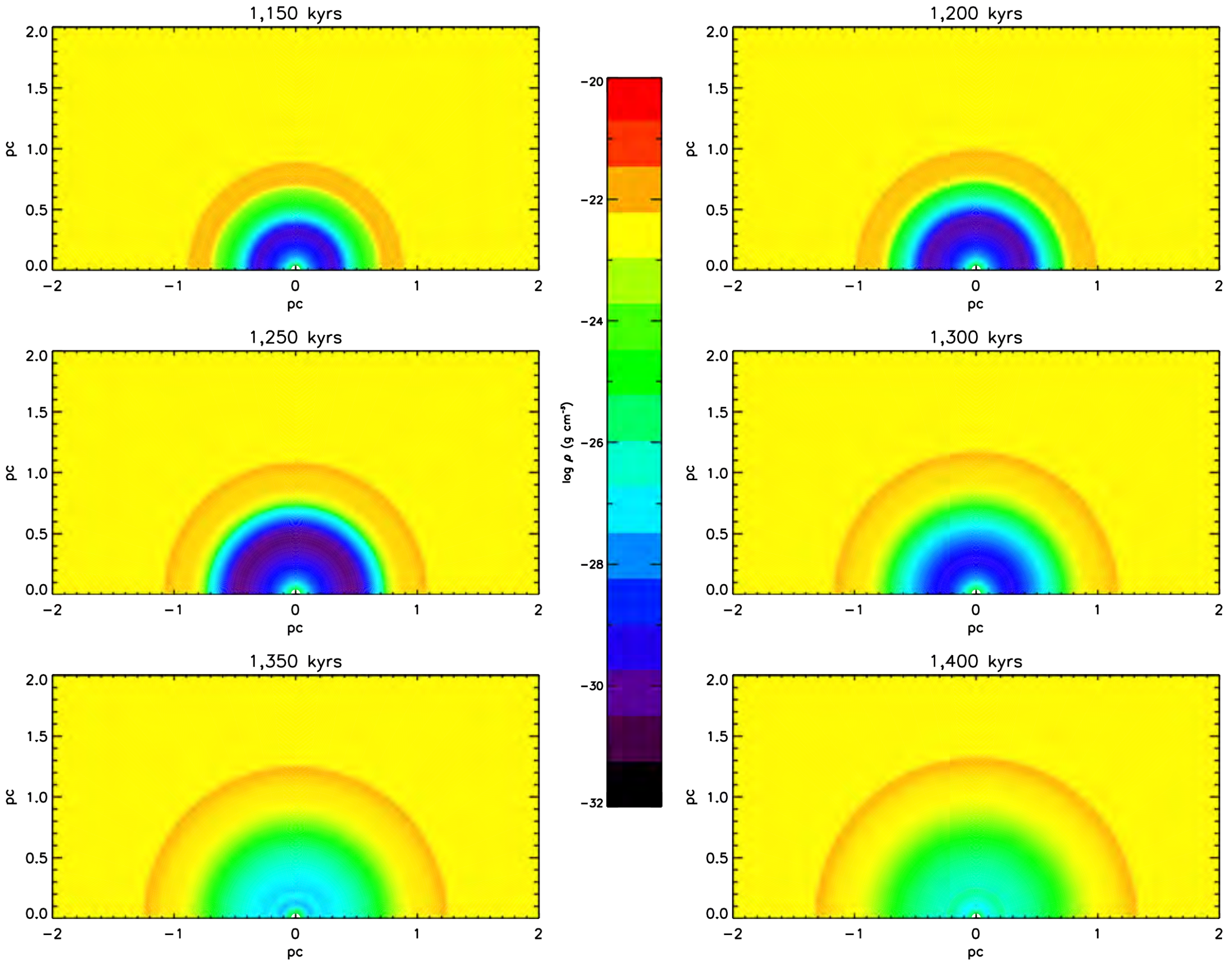

Figure 5.4: Density contour plot of the evolution of a supernova in uniform ISM with no relative motion or magnetic field.

The hot interior of the SNR is now enclosed by a thin cool shell of swept up, shocked, and cooled ISM material. The shock continues to slow and upon reaching a velocity comparable to that of the surrounding ISM, the shell loses its identity and fades away (e.g. Woltjer, 1972, Draine, 2011).

5.3 The Effects of Radiative Cooling on SNR Evolution in an Undisturbed ISM

As in the previous section, SNR evolution in uniform ISM with no relative motion or magnetic field, is considered. Also neglected, again at this stage, is the presence of a pre-existing cavity or astrosphere. In the free expansion phase, or ejecta dominated phase, it is expected that radiative cooling would not be important. The ejecta region at this stage has a high velocity and low density, and should result in high cooling time. The FS has higher density, the velocity however of the FS is still high and should also result in a high cooling time. As is pointed out earlier, radiative cooling of the SNR is first expected during the snowplow phase; how-

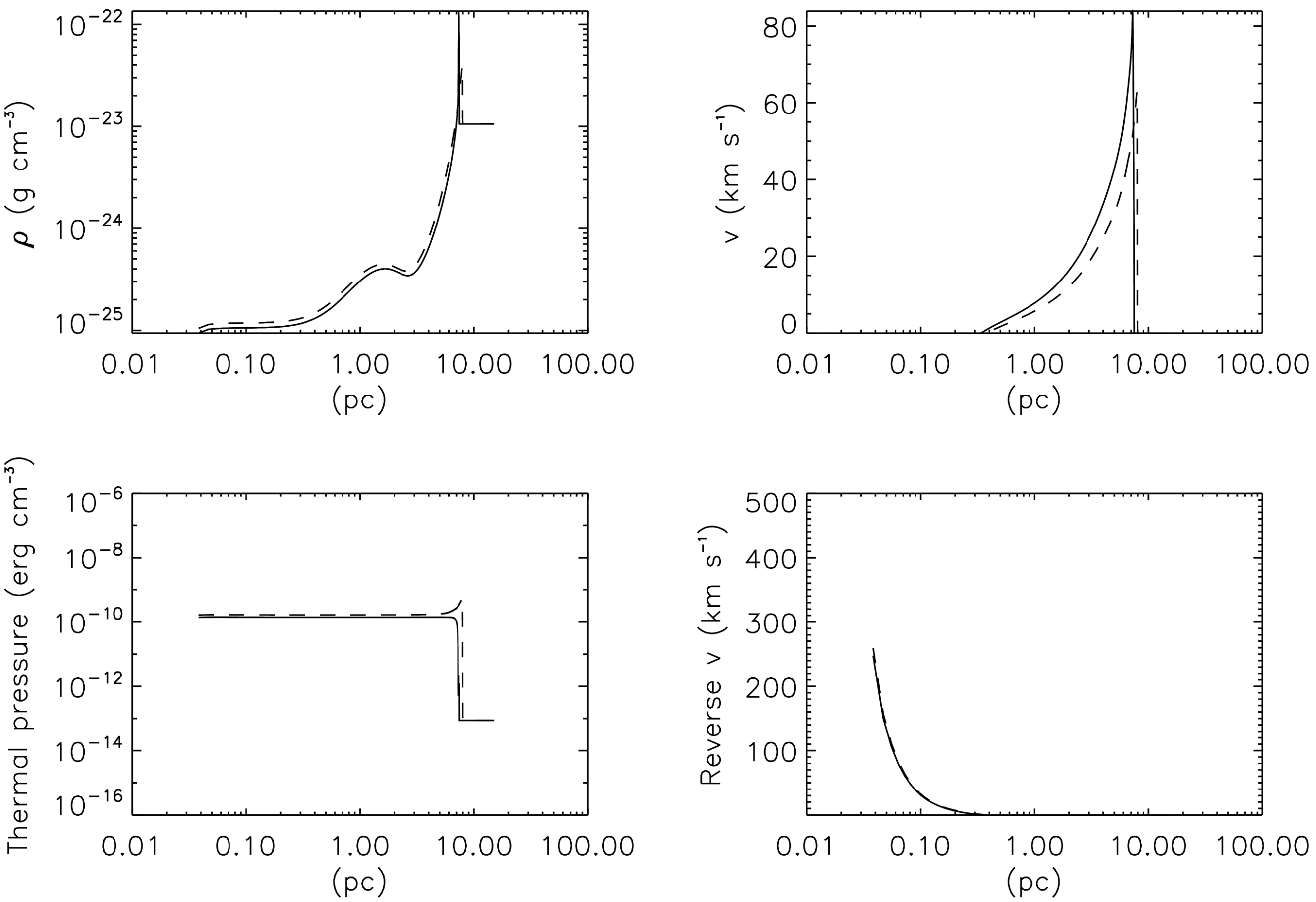

Figure 5.5: The computed density, outward bulk velocity, thermal pressure and backwards bulk velocity of a SNR in a uniform ISM with no relative motion or magnetic field. Results with radiative cooling is shown as the solid line, while the result without radiative cooling is shown as the dashed line. Results are shown at 38 kyrs.

ever, Falle (1975b) and Falle (1981) describe catastrophic cooling during the transition from the Sedov-Taylor phase to the point when the SNR merges with the ISM, while Cioffi et al. (1988) finds that radiative cooling may start after the end of the free expansion stage.

Figure 5.5 shows the density, bulk outwards velocity, thermal pressure, and backwards (toward the inner boundary) bulk velocity for a SNR evolving in a uniform ISM with no relative motion or magnetic field for parameters as discussed earlier. The ISM density is now 1.05×10^{-23} g cm^{-3}. The results are shown at 38 kyrs after the explosion. The solid line shows results with radiative cooling, while the dashed line shows results without radiative cooling included in the model. The difference between the results with and without radiative cooling shows that the computations with radiative cooling is significantly more compressed in the FS region compared to the no-cooling case. This illustrates that radiative cooling has a significant effect, especially at the FS region.

The outward velocity profile shows only the forward moving plasma while the reverse velocity profile shows the backwards moving plasma; in this case, the RS has returned to the origin long ago. The reverse velocity profile thus shows the shocked ejecta which was heated by the ejecta. The FS in the thermal pressure profile shows that the result with radiative cooling is closer to the center after 38 kyrs of simulation time. This is a result of the FS loosing thermal pressure and, to balance, moves inwards compared to the no cooling result.

Predictions of a radiative RS are made by McKee & Truelove (1995). Since the RS maintains approximate pressure equilibrium with the gas behind the FS it is found that (McKee, 1974)

$$\rho_{ej} v_{RS}^2 = \beta \rho_0 v_{FS}^2, \tag{5.8}$$

where v_{RS} is the velocity of the reverse shock, and v_{FS} is the forward shock velocity in the ejecta dominated phase (free expansion phase), and ρ_0 is the ISM density. During the ejecta dominated phase v_{FS} remains approximately constant, while the ρ_0 is also constant. The ejecta density, ρ_{ej}, however, will drop dramatically. Therefore the RS shock velocity, v_{RS}, must increase to maintain pressure equilibrium. To do this the RS turns around and moves into the ejecta, as shown in Ferreira & de Jager (2008).

Figure 5.6 shows a contour plot of the density as a function of time and distance on a logarithmic scale showing the evolution of a SNR evolving in a uniform ISM, including radiative cooling. Figure 5.7 shows the same, but for the thermal pressure. Both results are shown up to 40 kyrs and 10 pc. The evolution of the outward moving FS is clearly visible in both figures. The RS returning to the origin at 1.2 kyrs can be seen, where the blue and purple shaded regions, corresponding to low density and pressure, are suddenly filled and heated as the RS moves inward.

In both figures, secondary shocks are also clearly visible, bouncing off the inner boundary as the RS reaches the origin. These secondary shocks eventually also reach the FS at about 10 kyrs. At 20 kyrs, the FS shock is at 7 pc, and for this later stage, the effect of radiative cooling becomes important, as shown in the previous figure.

5.4 SNR Evolution in a Pre-Existing Cavity with No ISM Magnetic Field or Relative Motion

Most supernovae are expected to explode in low density hot media (e.g. Tang & Wang, 2005). The SNR RCW 68 is an example of a SNR evolving in a windblown bubble, cavity or astrosphere. The astrosphere creates a low density environment in which the SNR expands freely (Chevalier & Liang, 1989). The free expansion ends when the SNR interacts with OAS (Chevalier & Liang, 1989), and creates a reflection and a transmitted shock (e.g. Tenorio-Tagle et al., 1990a,b, 1991). Dwarkadas (2005) shows that these shocks can already be created with the interaction of the remnant with the IAS. The evolution of the SNR in the pre-existing astrosphere

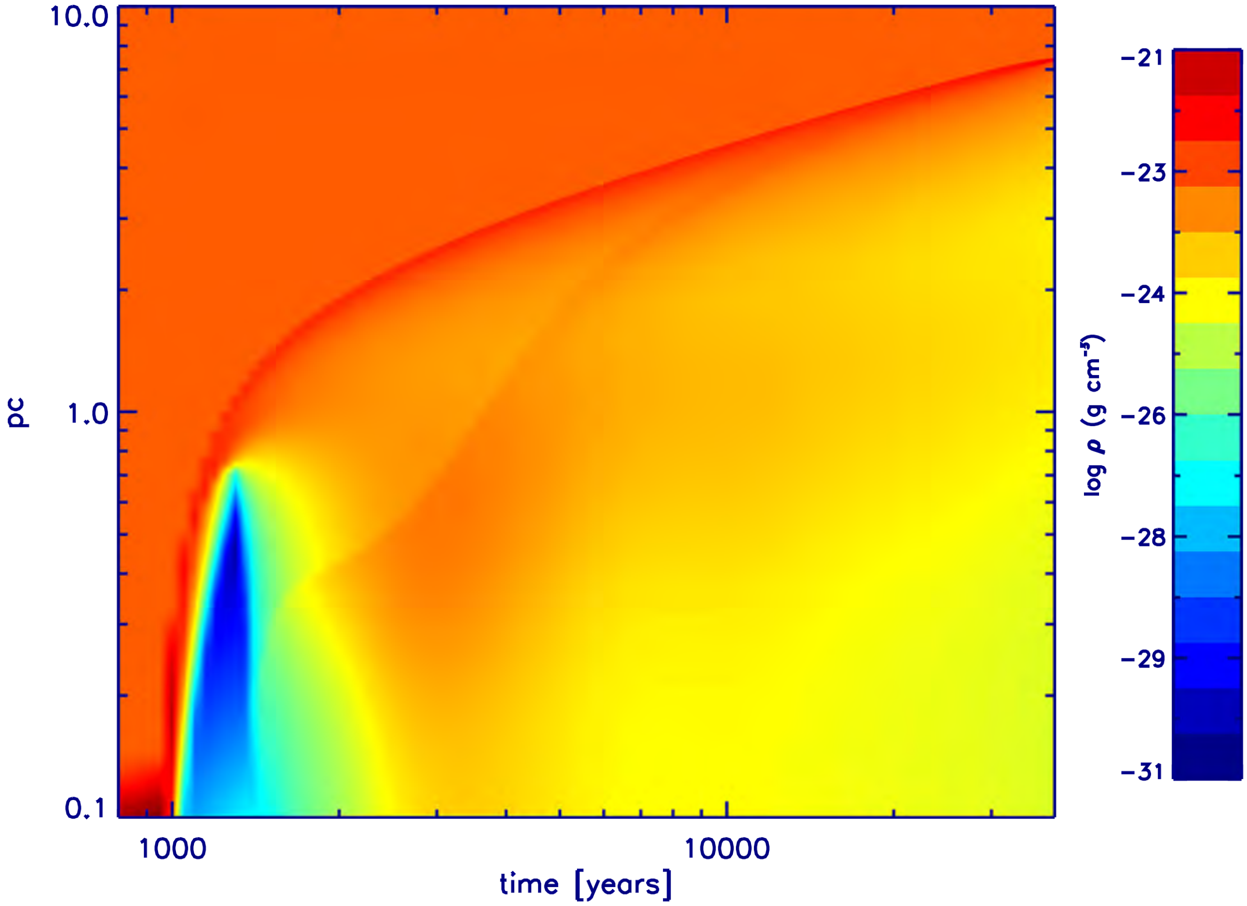

Figure 5.6: Contour plot of density of a SNR evolving in a uniform ISM as a function of time and distance. Radiative cooling is included

is found to be dependent on the structure of the astrosphere in which it is evolving (e.g. Franco et al., 1991, Dwarkadas, 2005). Further simulations on SNR in a pre-existing cavity is presented by Pérez-Rendón et al. (e.g. 2009), Haid et al. (e.g. 2016), and Chen et al. (2003).

In this section the supernova is now detonated in a cavity as shown in Figure 5.8. The cavity is a result of an outflow with a velocity of 1500 $\mathrm{km\ s^{-1}}$. An outflow density of $10^{-23.5}$ $\mathrm{g\ cm^{-3}}$ and temperature 10^4 K at 1.7×10^{-2} pc is assumed for the inner boundary conditions. For the ISM, a density of 1.05×10^{-23} $\mathrm{g\ cm^{-3}}$ with a temperature of 100 K, is assumed. No relative motion, ISM magnetic field or radiative cooling was included. The BS is found at $\approx$ 7.5 pc while the AP, and the end of the stellar wind, is found at $\approx$ 6 pc. The supernova is detonated after some time for the cavity to form, e.g. at 100 kyrs at the center of the grid (0.01 pc), as shown in Figure 5.8. These results are now compared to the case where the simulated explosion occurs in the undisturbed ISM.

Figure 5.9 shows the SNR evolution in a cavity, depicted with a solid line, and the SNR evolution without a cavity in the undisturbed ISM, shown with a dashed line. Results are shown at 250 yrs after the detonation of a supernova. As mentioned before, radiative cooling, relative

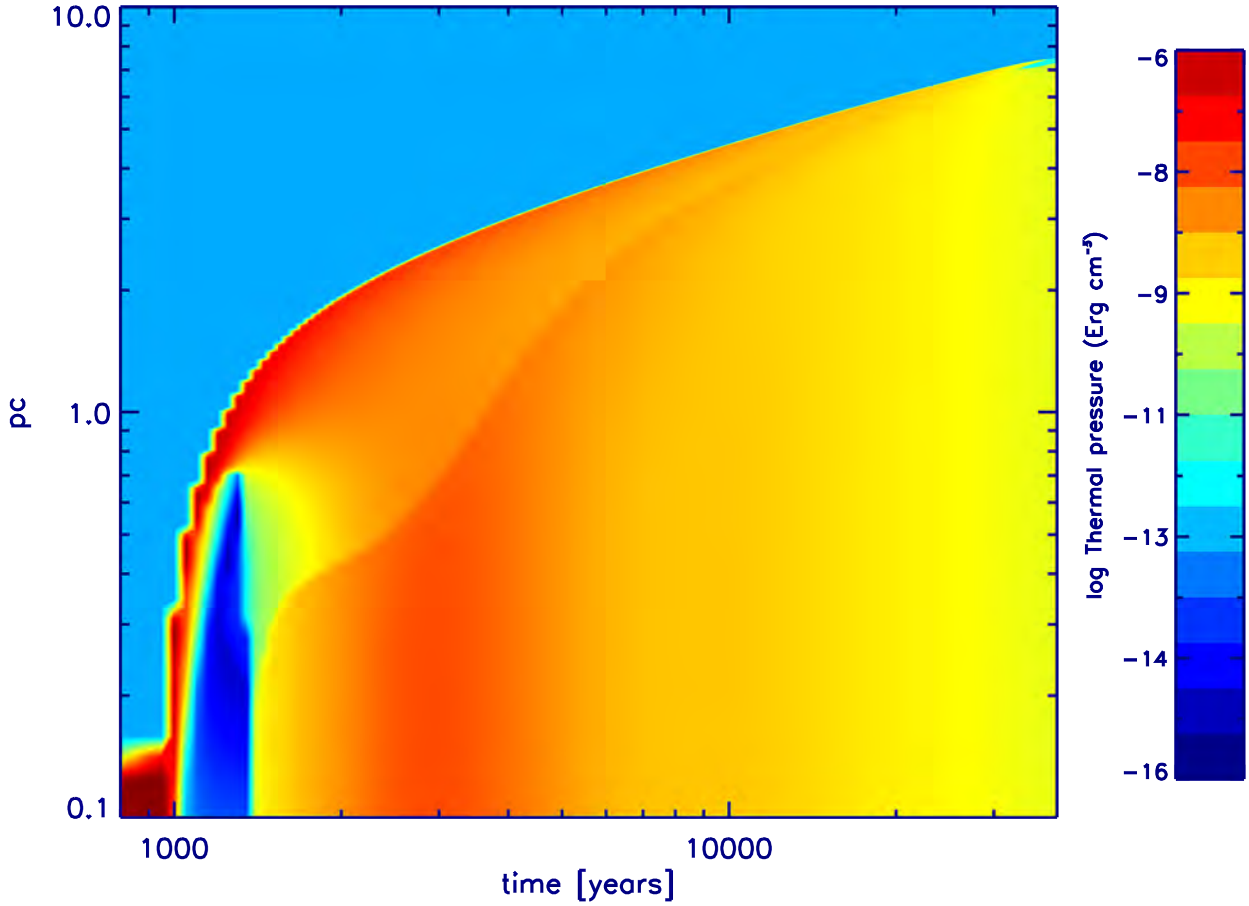

Figure 5.7: Contour plot of thermal pressure of a SNR evolving in a uniform ISM as a function of time and distance. Radiative cooling is included

motion, and the ISM magnetic field has been neglected and is included later. The SNR evolving in the pre-existing cavity (solid line) is still in the free expansion phase of the cavity and has just interacted with the TS and IAS. The SNR without the cavity (dashed line) is as of yet not as evolved as the result with the pre-existing cavity (solid line). It can barely be seen at 0.1 pc.

The reason for this, is that the SNR in a pre existing cavity is evolving in a much lower density environment. A result of this is that it will have to do a lot less work since the SNR has less matter to move. The opposite is true for the case of the supernova evolving in the undisturbed ISM. Since this is a much more dense environment, the supernova will have to do more work moving the ISM. This will result in it expanding at a slower rate. When the FS collides with the TS at ≈ 0.9 pc it creates a transmitted shock progressing into the IAS.

Figure 5.10 shows the same as Figure 5.9 but at 500 yrs after the detonation of a supernova. Here the FS is being transmitted into the IAS, and has not yet interacted with the OAS or BS. The interaction of the FS of the SNR with the TS of the pre-existing cavity has not resulted in reflected shock. The SNR without the pre-existing cavity (dashed line) is still in the free

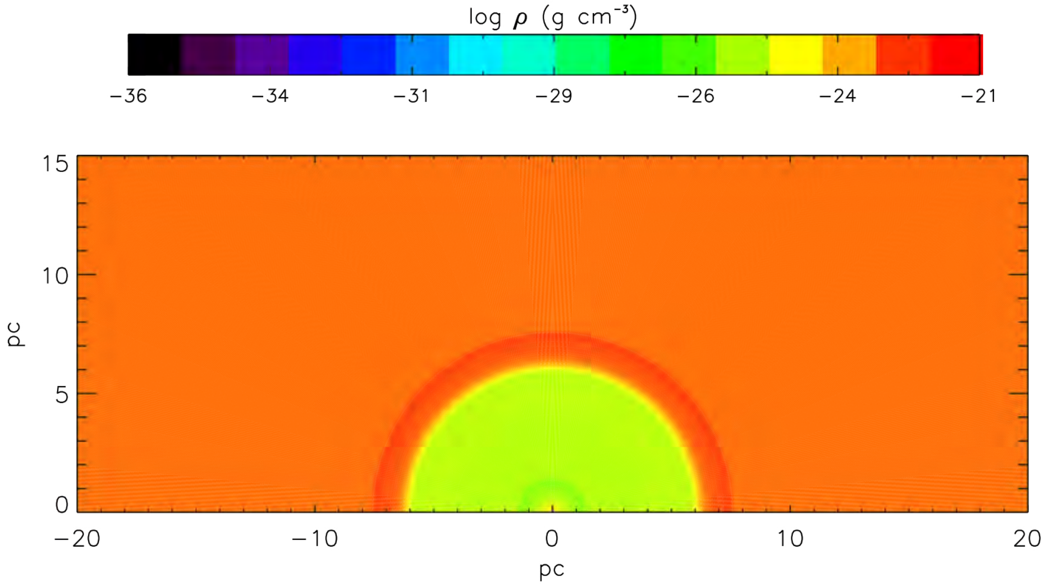

Figure 5.8: A plot of density of a cavity in which the supernova is detonated. The cavity is a result of a stellar wind with an outflow with a velocity of 1500 $\mathrm{km\,s^{-1}}$ with an outflow density of $10^{-23.5}$ $\mathrm{g\,cm^{-3}}$ and temperature 10^4 K at 1.7×10^{-2} pc is assumed for the inner boundary conditions. For the ISM a density of 1.05×10^{-23} $\mathrm{g\,cm^{-3}}$ with a temperature of 100 K is assumed. No relative motion, ISM magnetic field or radiative cooling was included.

expansion phase.

Figure 5.11 shows again the SNR evolution in a cavity, shown with a solid line, and the SNR without a cavity, shown with a dashed line, but this time at 1.15 kyrs after the detonation of a supernova. For the solid line, it can be seen that the FS has yet to reach the OAS or the BS of the astrosphere situated at ≈ 7.5 pc. Also shown is a pressure gradient for the case with the pre-existing cavity that can be found at ≈ 0.6 pc. This leads to the RS which decelerates the rapidly expanding ejecta (e.g. Tenorio-Tagle et al., 1990a). For the case without the pre-existing cavity (dashed line), the SNR is still in the free expansion phase and has a higher maximum forward velocity, and pressure. The higher thermal pressure for the dashed line scenario is a result from the SNR evolving in the ISM instead of a pre-existing cavity, which would have lower thermal pressure. This implies that the thermal pressure gradient would become large at a relatively early time compared to case with a pre-existing cavity. As a result of this, the RS would start its movement back towards the center earlier than the result with a pre-existing cavity.

Figure 5.12 shows the SNR evolution at 3.35 kyrs after the detonation of the supernova. For the case with the pre-existing cavity, the FS has reached the OAS and the transmitted shock has

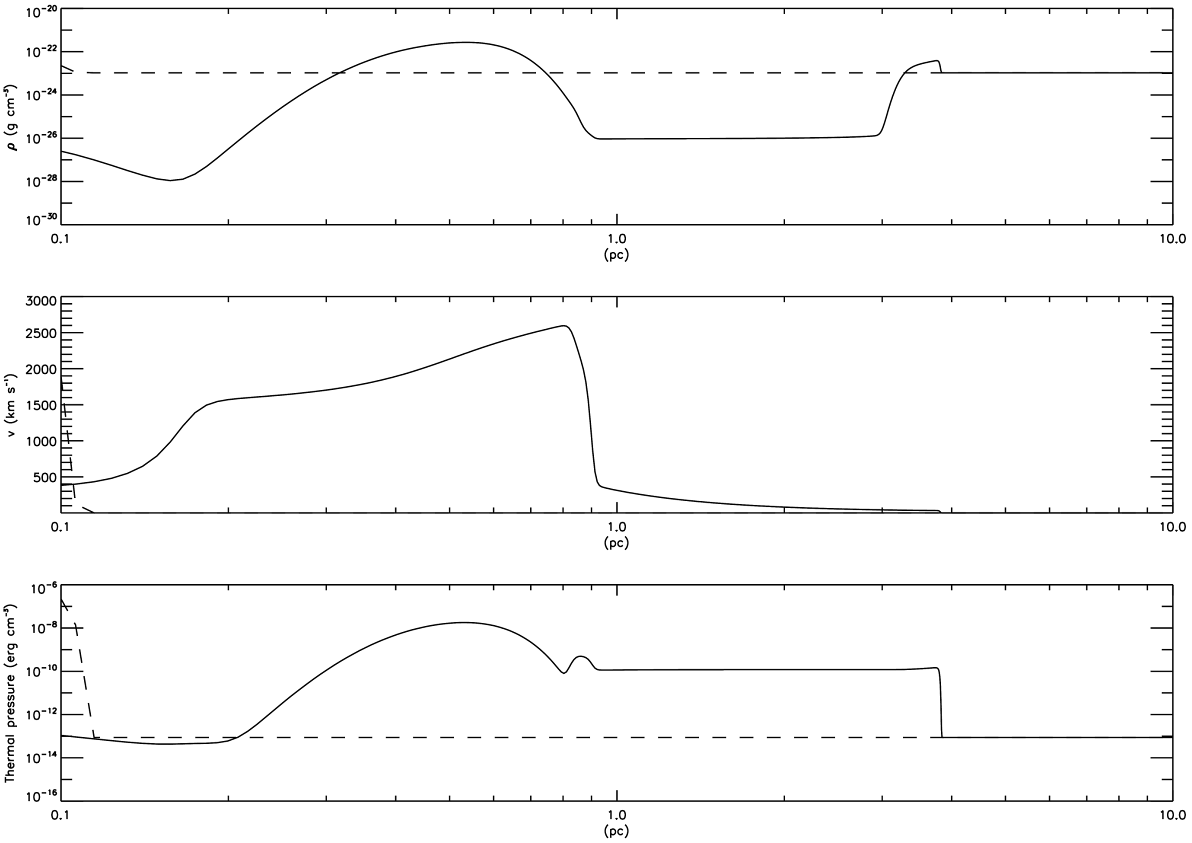

Figure 5.9: The density, outward bulk velocity, and thermal pressure of a SNR evolving in a cavity (as shown in Figure 5.8) shown with a solid line, while the supernova evolving in the undisturbed ISM is shown with a dashed line. Results are shown for a SNR with no relative motion or ISM magnetic field. The results are shown at 250 yrs after the detonation of the supernova.

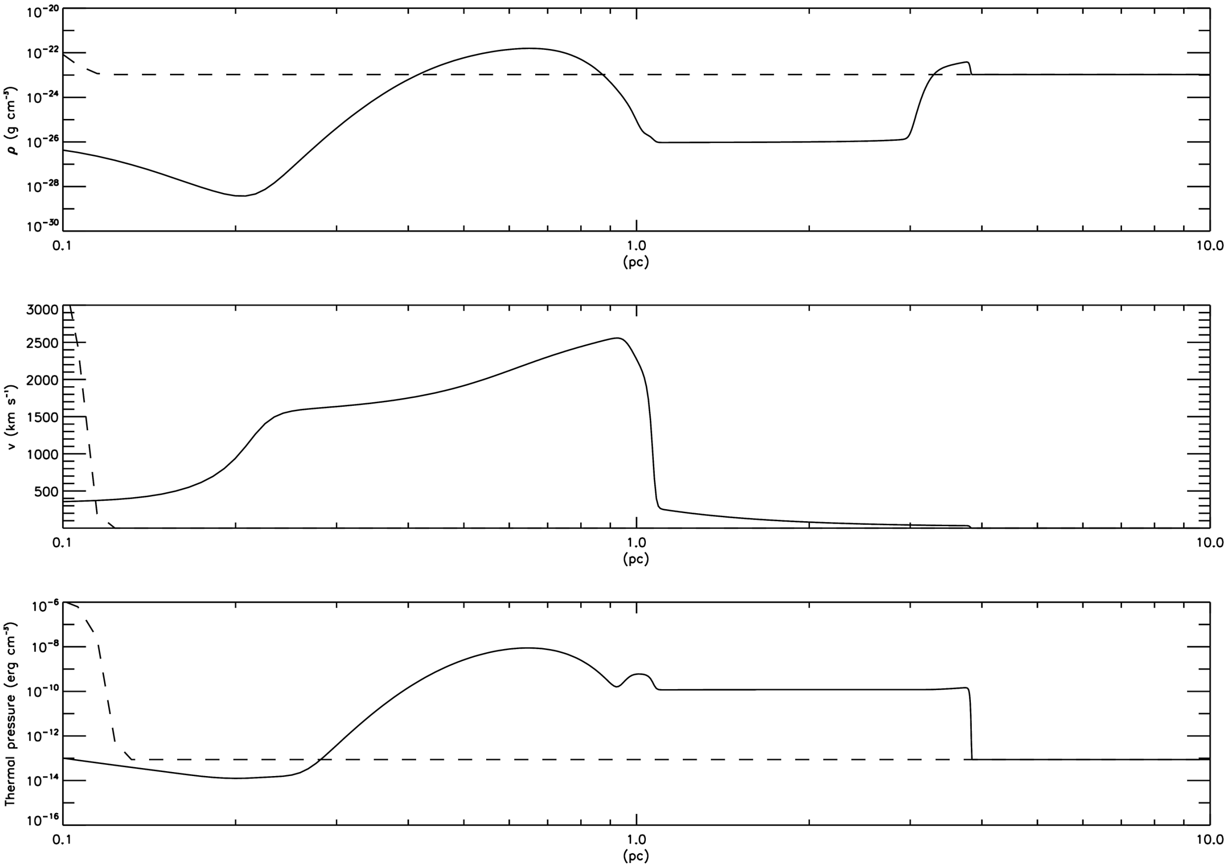

Figure 5.10: Similar to Figure 5.9, but for 500 yrs after the detonation of the supernova.

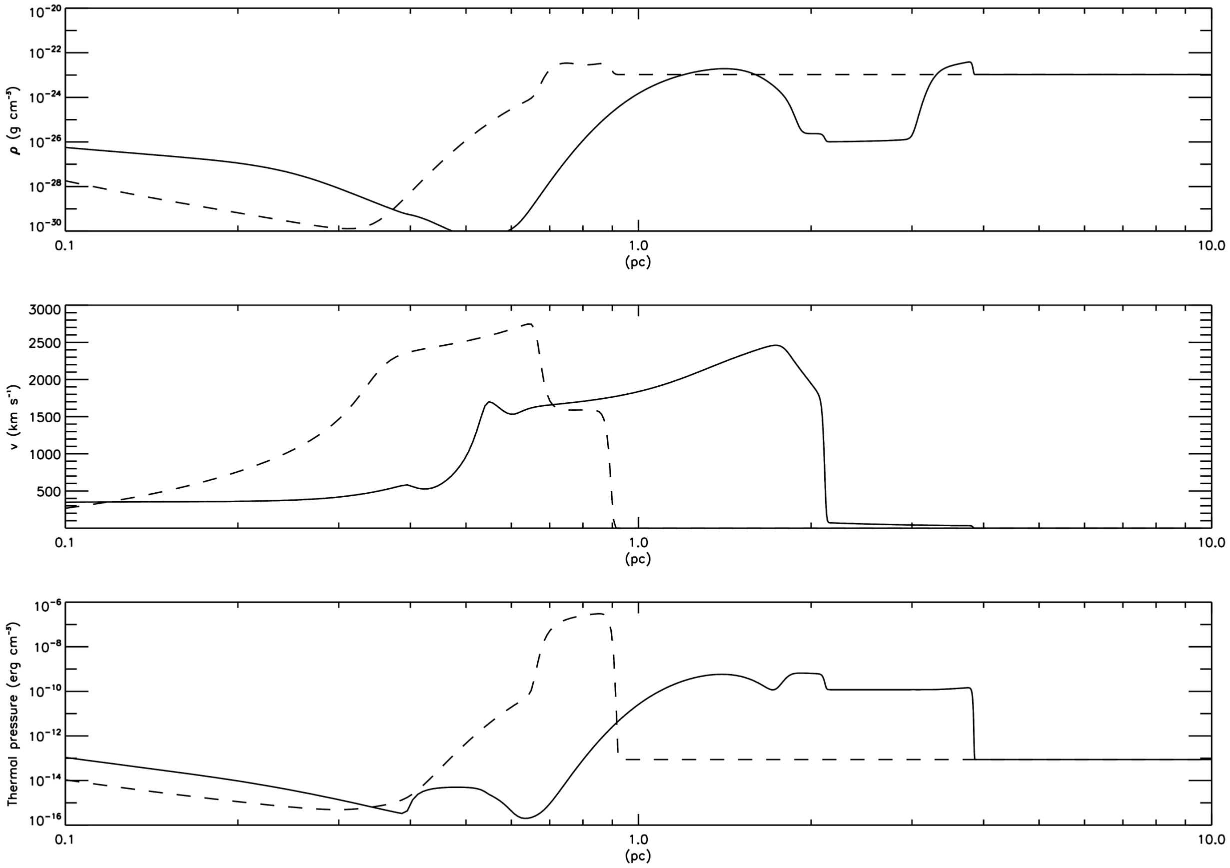

Figure 5.11: Similar to Figure 5.9, but for 1.15 kyrs after the detonation of the supernova.

started to propagate through the OAS. Also shown now, as opposed to the previous figures, is the reverse velocity e.g., flow back towards the center. The reflected shock can now clearly be seen moving back to the centre in the reverse velocity plot (solid line) at ≈ 3 pc at a reverse velocity of ≈ 400 $\mathrm{km\ s^{-1}}$. For the result without the pre-existing cavity (dashed line), the reverse shock already reached the origin with waves now moving back and forth. As shown in the pressure plot for this scenario, the interior of the SNR is heated to a higher thermal pressure.

Not so clear in a snapshot plot but in Figure 5.13 the reflected shock (for the case with pre-existing cavity), reflecting off the OAS, has collided with the RS shocked ejecta. The thermal pressure from the reflected shock interacts with that of the RS and pushes the RS backwards towards the centre. The plot of the reverse velocity shows that the velocity has increased to over 25 000 $\mathrm{km\ s^{-1}}$, and shows just how effective this process is. The next two figures connect to this aspect.

Figure 5.14 shows contour plots of the density concentrating on the RS evolution of the SNR from 3.4 kyrs to 4.9 kyrs, with the lowest density (blue) at 10^{-36} g cm^{-3} and the highest density (red) at 10^{-21} g cm^{-3}. Simulations include a pre existing cavity. From 3.4 kyrs to 3.6 kyrs the RS forms and still moves forward. At 3.7 kyrs, however, the RS has reversed to ≈ 2.5 pc, and at 3.8 yrs the RS has already reached the center. The RS moves backwards towards the centre

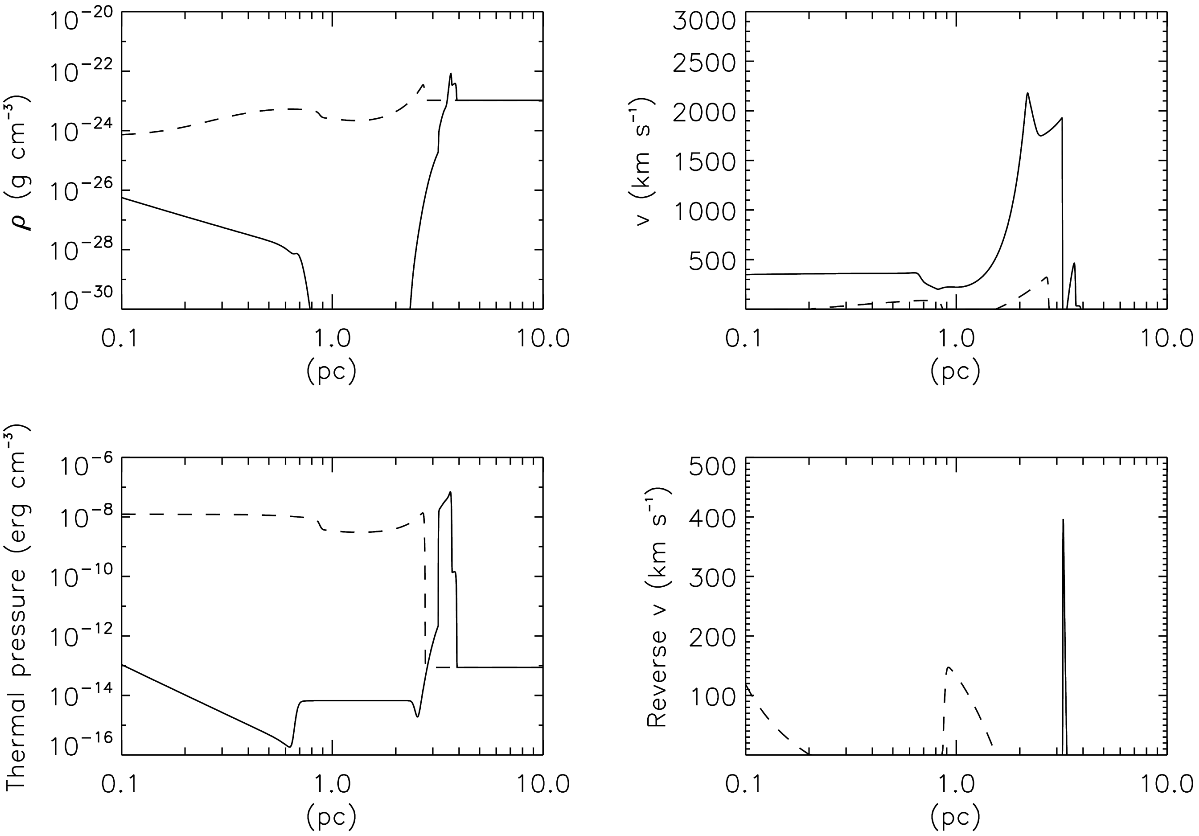

Figure 5.12: Similar to Figure 5.9, but shown at 3.35 kyrs after the detonation of the supernova. Also shown now is the reverse velocity e.g., flow toward the center.

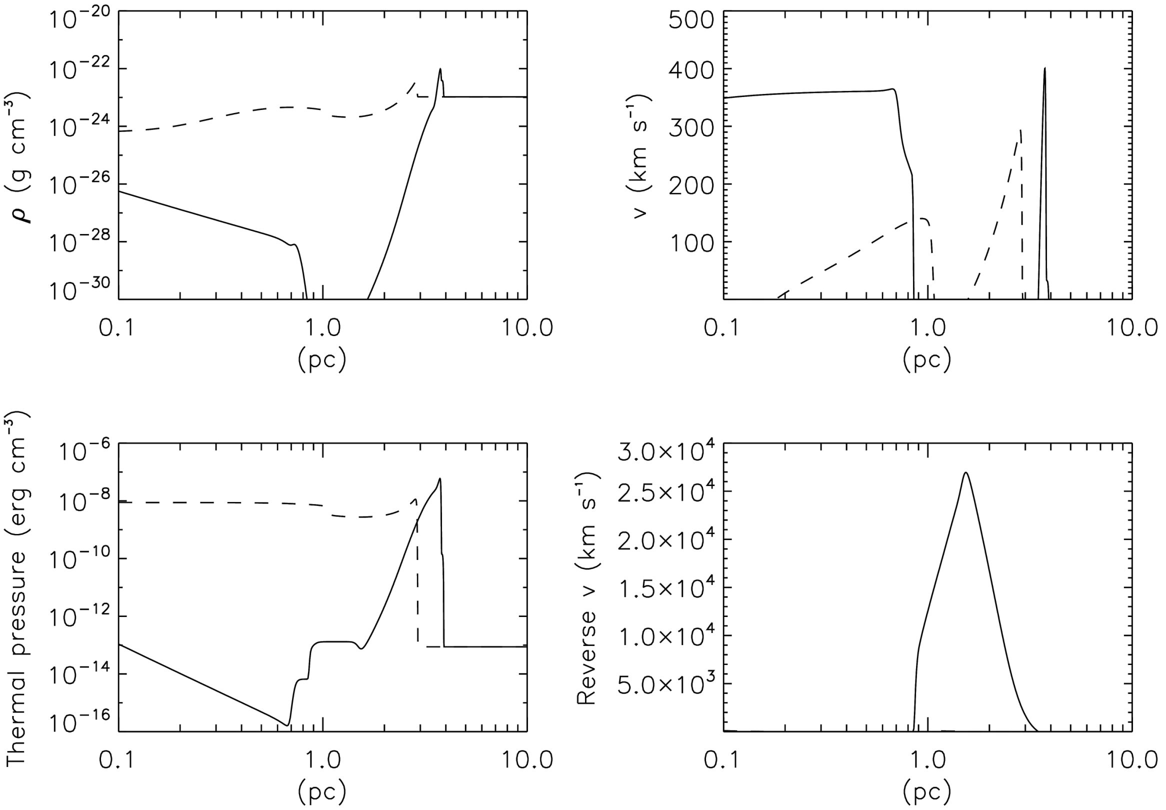

Figure 5.13: Similar to Figure 5.12, with results shown at 3.75 kyrs, after the detonation of the supernova.

after interacting with the reflected shock, as explained earlier. At 4.9 kyrs, secondary shocks can be seen emerging from the center. This is more quantitatively shown in Figure 5.15, which shows the density, bulk velocity, thermal pressure and backwards bulk velocity of a SNR in a cavity at 3.5 kyrs (solid line), 3.7 kyrs (dashed line), 3.9 kyrs (dot-dashed line), and 6 kyrs (dot-dot-dot-dashed line). These dates are shown to highlight the return of the RS back to the origin.

The RS starts to form at 3.5 kyrs (solid line) and is clearly visible as the thermal pressure gradient at 6 pc in Figure 5.15. At this stage, the FS interacts with the boundary of the cavity and a reflected shock has also started to move back from the OAS towards the RS (not visible in reverse velocity plot, because of the scale). At this time the RS still moves forward at a velocity of almost 2000 km s^{-1} (solid line in velocity plot).

At 3.7 kyrs (dashed line), the reflected shock has now interacted with the RS, and the RS has started to move backwards towards the origin. This can be seen in the thermal pressure plot where the RS is found at about $\approx$ 1.5 pc. The reverse velocity shows the RS moving backwards at a maximum velocity of over 25 000 km s^{-1}. At 3.9 kyrs, the RS is at 0.3 pc, and is clearly visible as the large gradient in the thermal pressure (dot-dashed line). The reverse velocity is now about 15 000 km s^{-1}. At 6 kyrs (dot-dot-dot-dashed line) is that the RS has already reached the center, and has reached the inner boundary of the SNR.

However, the reverse velocity profile at 6 kyrs (dot-dot-dot-dashed line) barely shows a reflected shock when the FS collides with the BS of the cavity, and causes matter to move backwards toward the center. This reduces the momentum available for the FS to move outwards.

5.5 SNR Evolution in a Pre-Exiting Cavity with No ISM Magnetic Field or Relative Motion, but with Effects of Radiative Cooling Included

A supernova is now detonated in a cavity similar to that of Figure 5.8 in the previous section. The cavity is again a result of an outflow with a velocity of 1500 $\mathrm{km\,s^{-1}}$, with an outflow density of $10^{-23.5}$ $\mathrm{g\,cm^{-3}}$ and temperature 10^4 K at 1.7×10^{-2} pc, is assumed for the inner boundary conditions. For the ISM, a density of 1.05×10^{-23} $\mathrm{g\,cm^{-3}}$ with a temperature of 100 K is assumed. However, radiative cooling is now implemented in both the cavity and the SNR. The effects of radiative cooling on an expanding spherical astrosphere is previously studied and shown in Chapter 3. The computed cavity is shown in Figure 5.16, and the most notable difference compared to Figure 5.8 is the highly compressed, high density surrounding OAS. As shown already, including radiative cooling results in the TS being further out, while the AP and BS is found to be closer to the center when compared to the case without the effect of radiative cooling.

Figure 5.17 shows the density, outward bulk velocity, and thermal pressure for a supernova

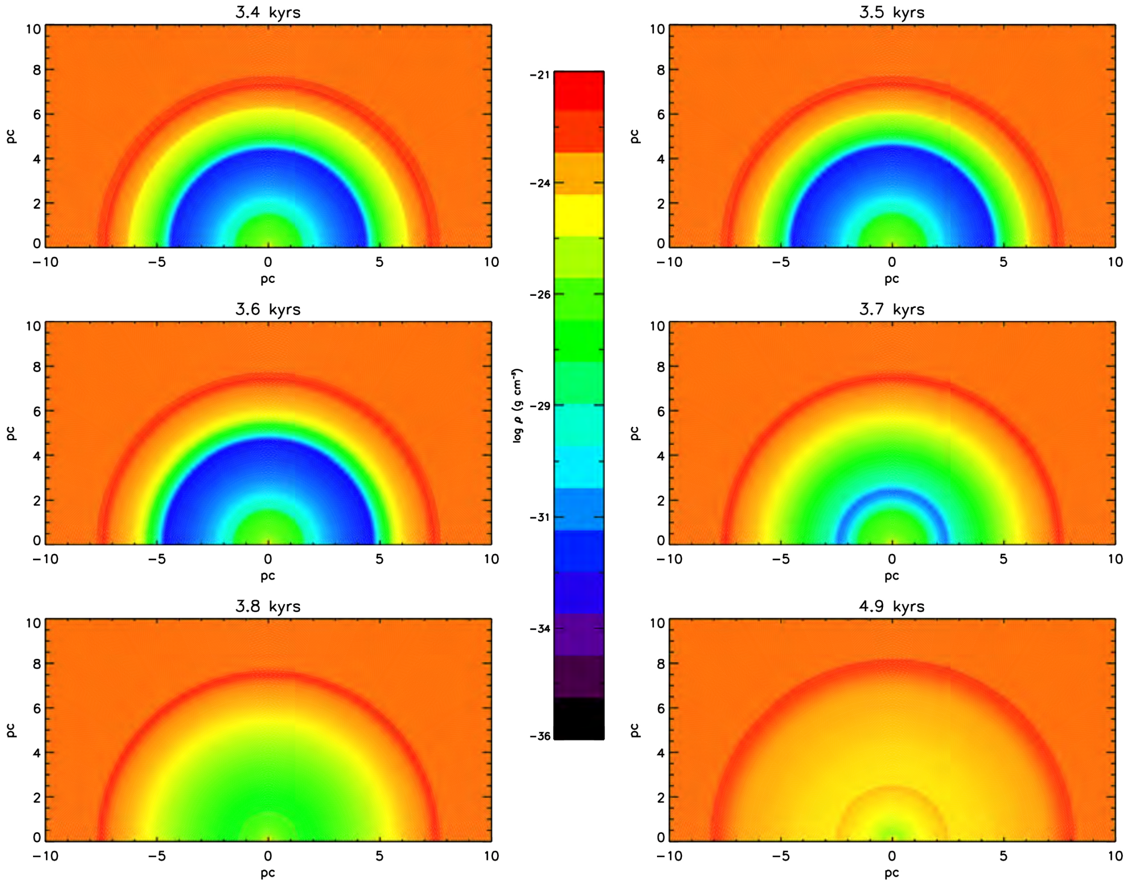

Figure 5.14: Contour plot of the evolution of a supernova in a cavity, at different times, with no relative motion or magnetic field. Radiative cooling is not included.

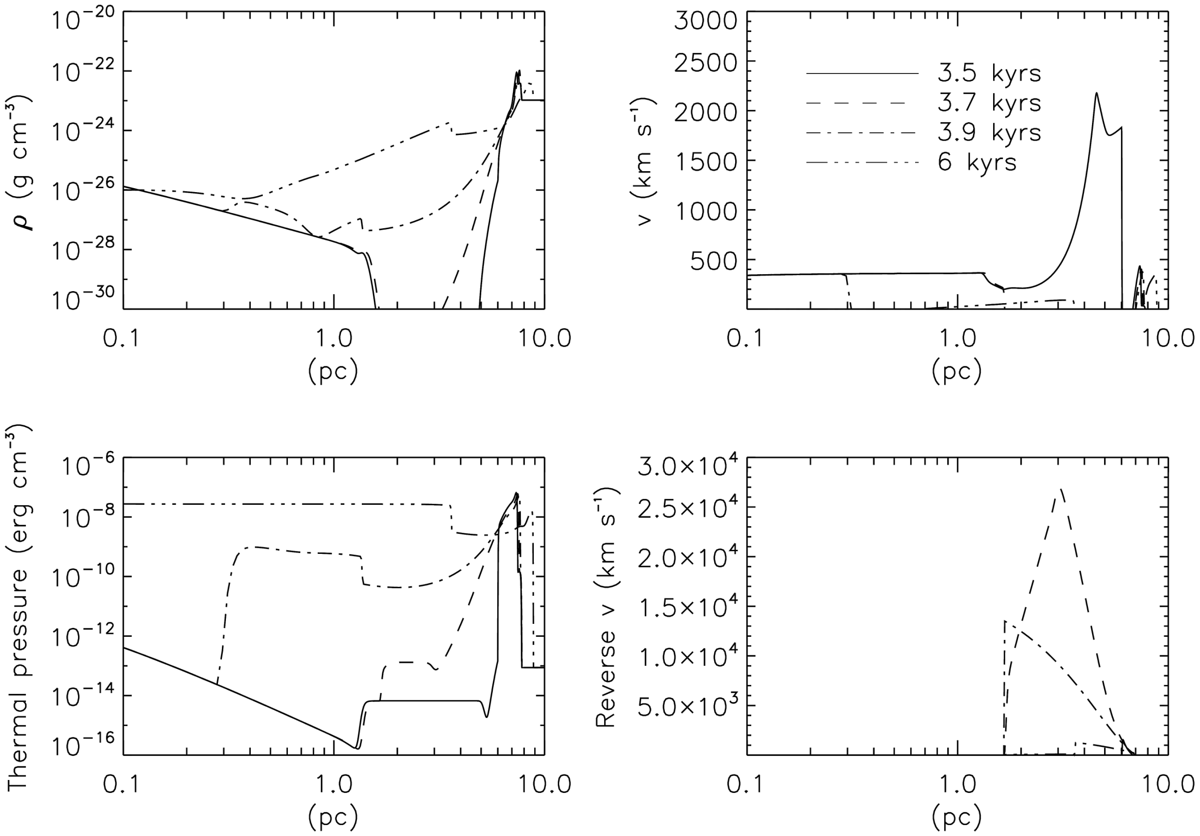

Figure 5.15: The density, bulk velocity, thermal pressure and backwards bulk velocity of a SNR exploding in a cavity. Results are shown for the case with no relative motion or ISM magnetic field. The results are shown at 3.5 kyrs (solid line), 3.7 kyrs (dashed line), 3.9 kyrs (dot-dashed line), and 6 kyrs (dot-dot-dot–dashed line) after the detonation of a supernova.

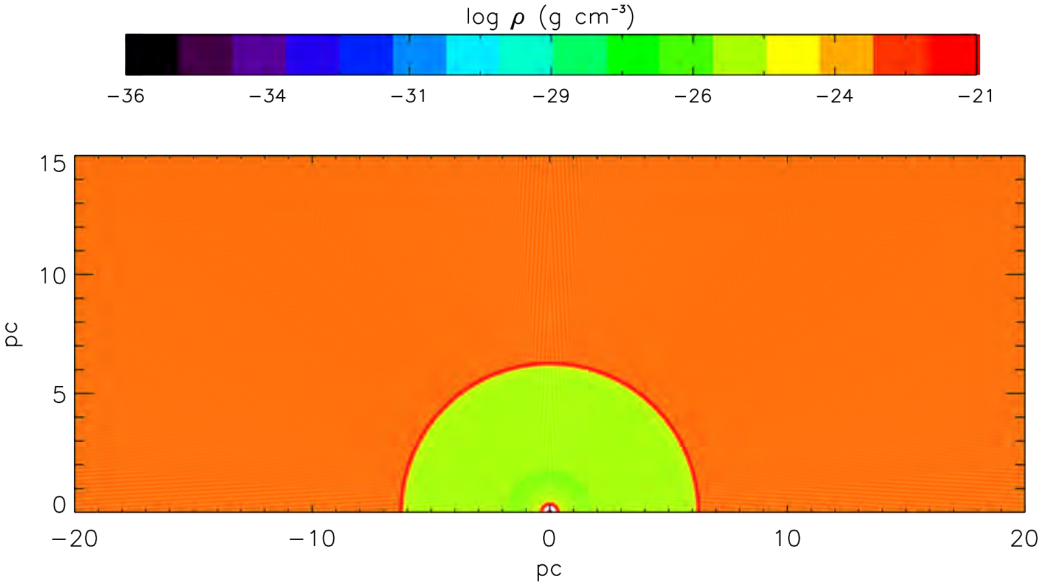

Figure 5.16: Computed stellar wind cavity in which the supernova will be detonated. The cavity is a result of a stellar wind with an outflow with a velocity of 1500 $\mathrm{km\ s^{-1}}$, an outflow density of $10^{-23.5}$ $\mathrm{g\ cm^{-3}}$ and temperature 10^4 K at 1.7×10^{-2} pc, assumed for the inner boundary conditions. For the ISM, a density of 1.05×10^{-23} $\mathrm{g\ cm^{-3}}$ with a temperature of 100 K is assumed. No relative motion, or ISM magnetic field are included. Here, the effects of radiative cooling is included.

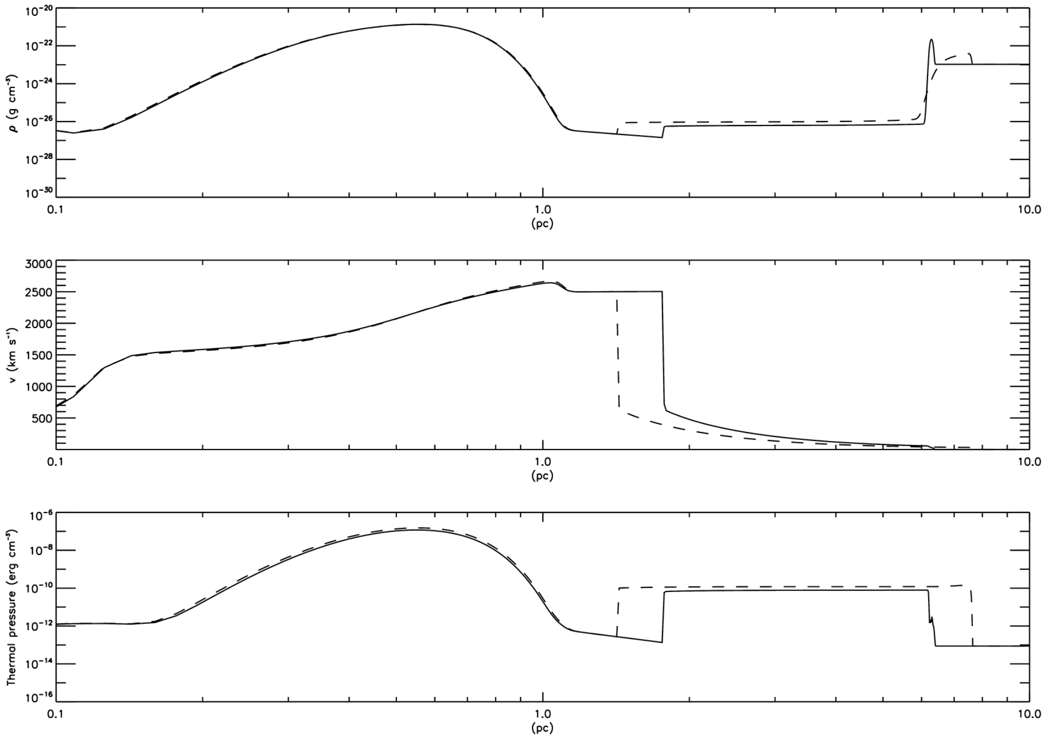

Figure 5.17: The density, outward bulk velocity, thermal pressure of a SNR evolution in a cavity (as in Figure 5.8) is shown by the dashed line. This scenario correspond to no radiative cooling included in the model. Results shown as a solid line corresponds to SNR evolution in a cavity (corresponding to Figure 5.16), where radiative cooling is included. Results are shown for SNR with no relative motion or ISM magnetic field. The results are shown at 250 yrs after the detonation of the supernova.

evolving in a cavity. Shown by the dashed line is the scenarios without radiative cooling. The new results, which include radiative cooling when the cavity is computed, are shown in Figure 5.17 with a solid line. This is shown for 250 yrs after the detonation of the supernova. The effects of radiative cooling are visible, i.e., the highly compact dense OAS and the TS being further away from the star at $\approx$ 1.7 pc compare to $\approx$ 1.1 pc for the result without radiative cooling. Here, for both results, the SNR is still in the free expansion region of the astrosphere, and has yet to interact with the TS or the IAS.

Figure 5.18 shows the evolution of the SNR for 400 yrs after the detonation of the supernova. For the computations without radiative cooling, the FS of this scenario has started to interact with the IAS. The result with radiative cooling (solid line) is still in the free expansion stage, because the TS for this scenario is further out. Figure 5.19 shows the same as in Figure 5.18, but for 600 yrs after the detonation of the supernova. Here it can be seen that in spite the earlier interaction of the SNR with the IAS, when radiative cooling is not included, the SNR evolution is now very similar once the radiatively cooled SNR also interacts with IAS.

Figure 5.20 shows the same as in Figure 5.18, but for 3.2 kyrs after the detonation of the supernova. The reverse velocity is now also shown in the bottom right panel. The FS of both the supernovas is now in the outer regions of the cavity, and starts to interact with the AP. It can be seen that in the computations with radiative cooling taken into account, the solid line, a reflected reverse shock has already started its backwards motion as seen in the reverse velocity profile at ≈ 5 pc. Since the AP and BS are closer to the origin when radiative cooling is included, the FS will interact with these structures sooner than in the case without radiative cooling. This then implies that a reflected shock, reflecting off of the AP, would be initiated earlier than the case without radiative cooling.

As shown in the bottom right panel of Figure 5.20, the result with radiative cooling results in a reflected reverse shock which reaches relatively high reverse velocities. This increases over time, as shown in Figure 5.21. Figure 5.21 shows the same but 50 years later at 3.25 kyrs. Here, this RS has reached a reverse velocity of over $3500\ \mathrm{km\,s^{-1}}$. The scenario without radiative cooling shows no reflected shock, yet.

As is noted in Chapter 3, the density of the OAS increases dramatically when radiative cooling is included. This increase in density could result in an increase in the shock impedance (e.g. Henderson et al., 1990), and result in an increase in the energy reflected back towards the center leading to the high reverse velocity for this scenario.

Although not visible in Figure 5.21, for both scenarios it is found that FS created a transmitted and reflected shock pair when interacting with the OAS. The transmitted shocks eventually change the OAS. Figure 5.22 shows the same, but now for 3.45 kyrs after the detonation of a supernova. The results corresponding to radiative cooling show that almost all of the matter is moving back towards the center, except for the FS that is still moving forward at $\approx 50\ \mathrm{km\,s^{-1}}$. The opposite is found for the results without radiative cooling. For this scenario, most of

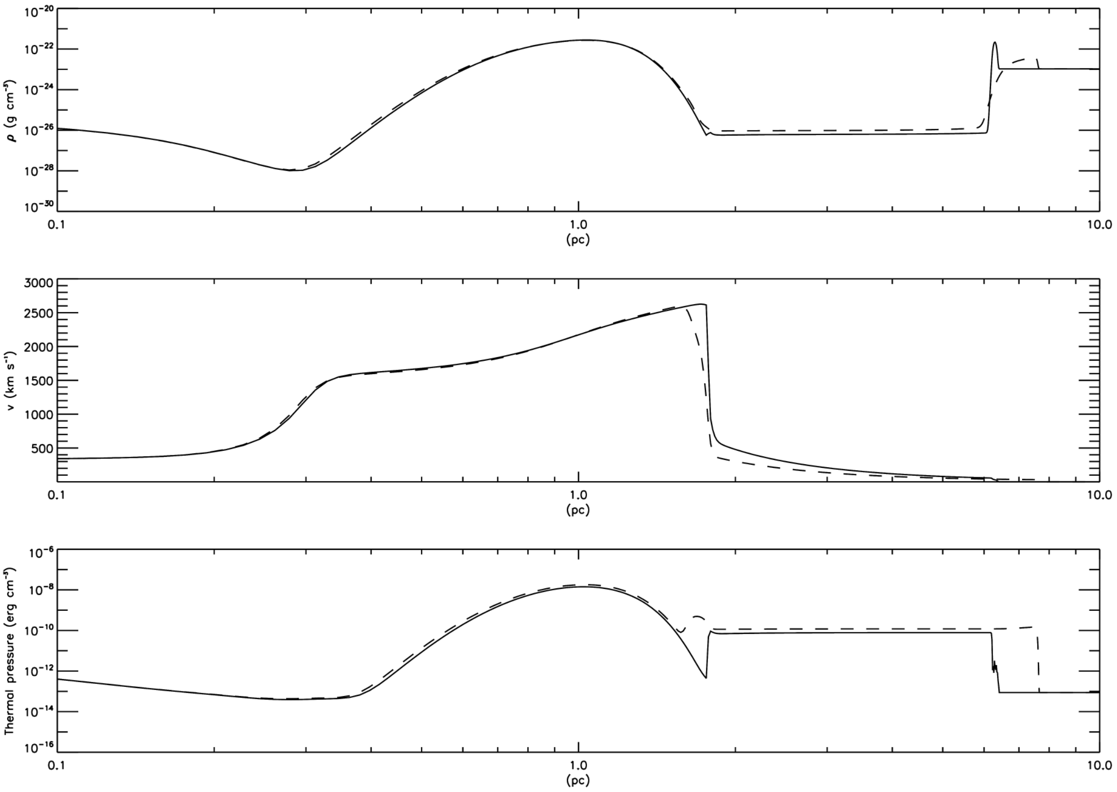

Figure 5.18: Same as Figure 5.17 but, for 400 yrs after the detonation of the supernova.

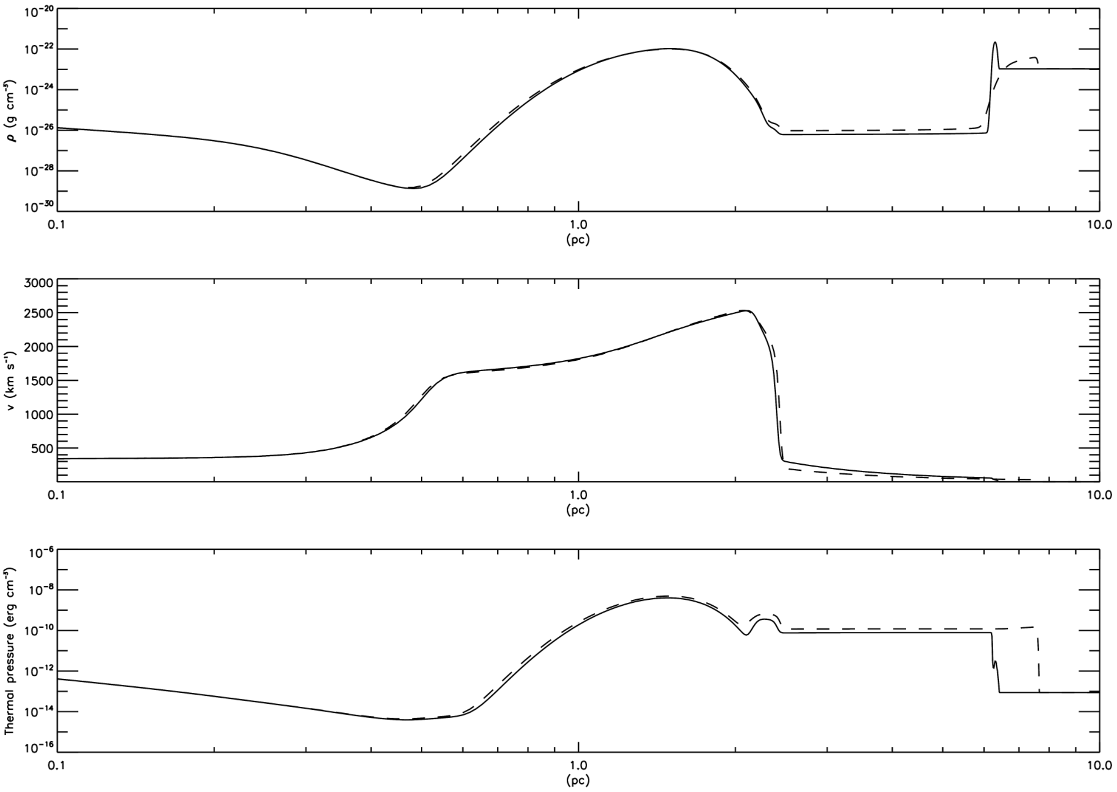

Figure 5.19: The same as Figure 5.18, but for 600 yrs after the detonation of the supernova.

the matter is still moving forward away from the center. The thermal pressure shows that the computations without radiative cooling has significantly less pressure everywhere at this time step, except at the OAS where the thermal pressure is similar to that of the results with radiative cooling. This is because the interior for the solid line scenario has been heated by the reflected shock.

The result with radiative cooling in Figure 5.22 shows that the RS has reached the center of the SNR, and implies that the SNR has reached the Sedov-Taylor phase. For the result without radiative cooling, the reflected shock, reflecting off the OAS, has yet to interact with the interior (not shown here), and it is found that this scenario reaches the Sedov-Taylor phase only at ≈ 4 kyrs after the detonation of the supernova.

Figure 5.23 shows a contour plot of the density as a function of time and distance showing the evolution of a SNR in a pre-existing cavity. The left panel shows the result without radiaitve cooling, while the right hand panel shows the result when radiative cooling has been included. The FS of the SNR in both cases is visible as the high density feature starting with 0.1 pc at 50 yrs, and then moving outward. The RS can be tracked when the blue and purple shaded regions (which corresponds to low density) is filled by the material flowing back after the passage of the RS. On the left panel, the result without radiative cooling, the TS of the cavity is barely visible at ≈ 1.5 pc before the interaction with the FS. For the results including radiative cooling, the TS is visible at ≈ 1.9 pc before the interaction with the FS. The OAS for both scenarios is found at 6 pc.

As shown, the FS interacts with the OAS, creating a transmitted shock and a reflected shock. The transmitted shock is transmitted into the OAS, while the reflected shock reflects off the OAS and moves back towards the center. Depending on parameters, the reflected shock may interact with the RS, causing the RS to move rapidly back towards the center, as explained earlier. Secondary shocks may form as the RS bounces off the origin.

5.6 The Effect of an ISM Magnetic Field on SNR Evolution

The introduction of an ISM magnetic field (in this work of 3 μG) to the case where the SNR evolves in an uniform ISM, i.e. no pre-existing cavity, seems to have no dynamic effect on the evolution of the SNR at early times (e.g. Ferreira & de Jager, 2008). This is because the SNR is kinetically dominated, making the effect of the ISM magnetic field negligible.

Figure 5.24 shows a contour plot of ISM magnetic field as a function of time and distance along a cut of the spherical solution. Radiative cooling is included, and for simplicity there is no field present from the star ,this is indicated by the blue shaded area up to ≈ 6, pc which represents a very small or neglected magnetic field. The SNR evolves in a pre-existing cavity with parameters as described earlier.

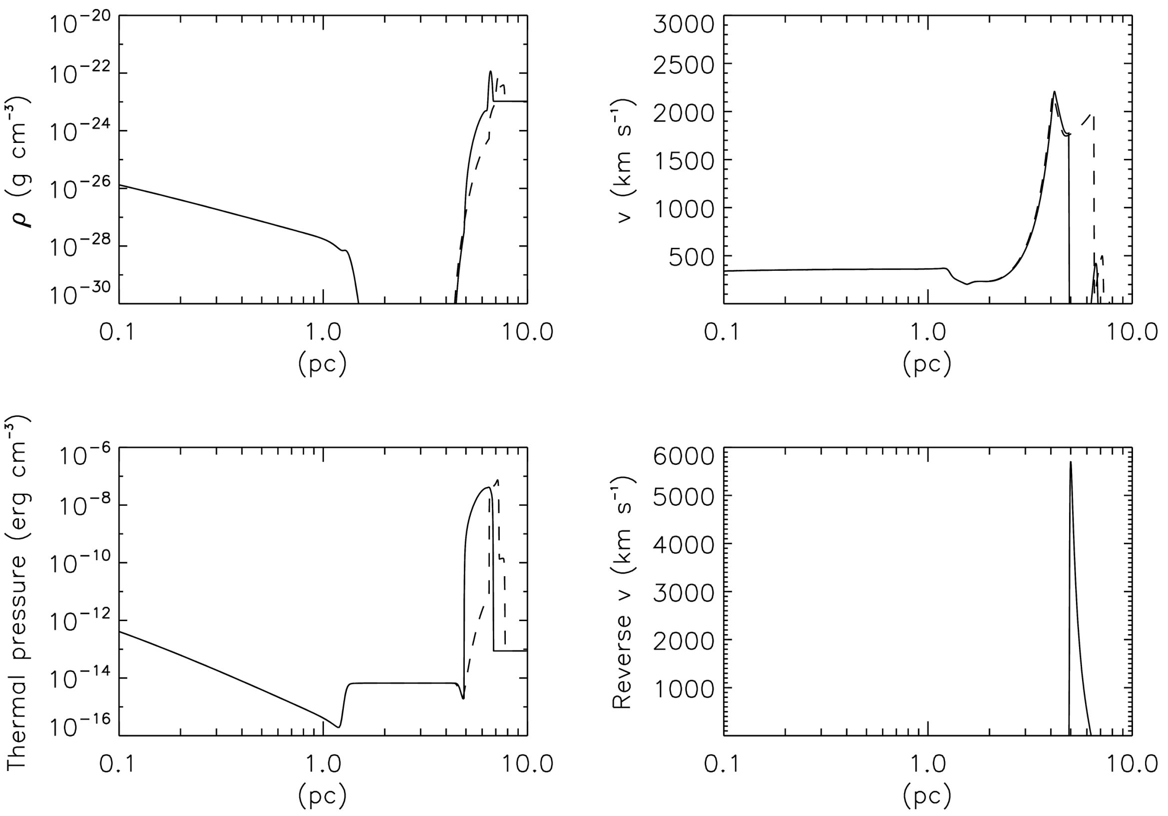

Figure 5.20: Similar to Figure 5.18 but, for 3.2 kyrs after the detonation of the supernova. The reverse velocity is now included.

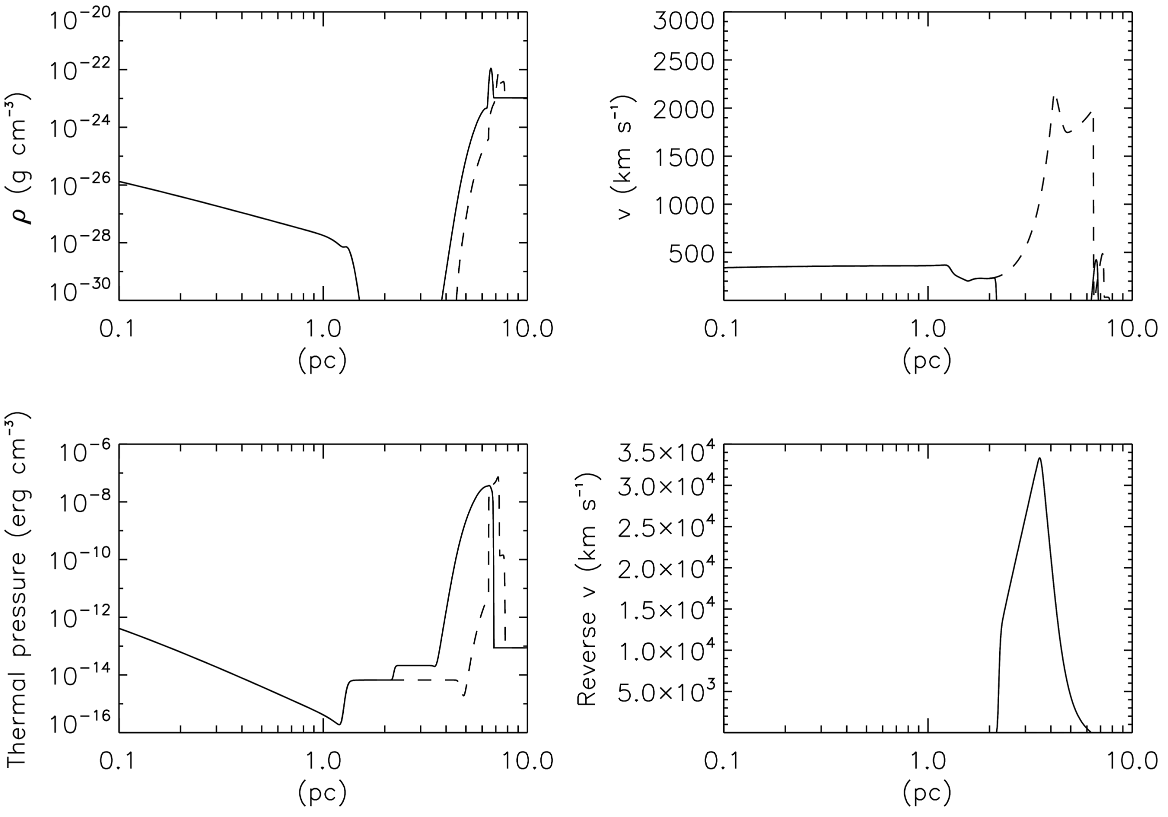

Figure 5.21: Similar to Figure 5.20 but, for 3.25 kyrs after the detonation of the supernova.

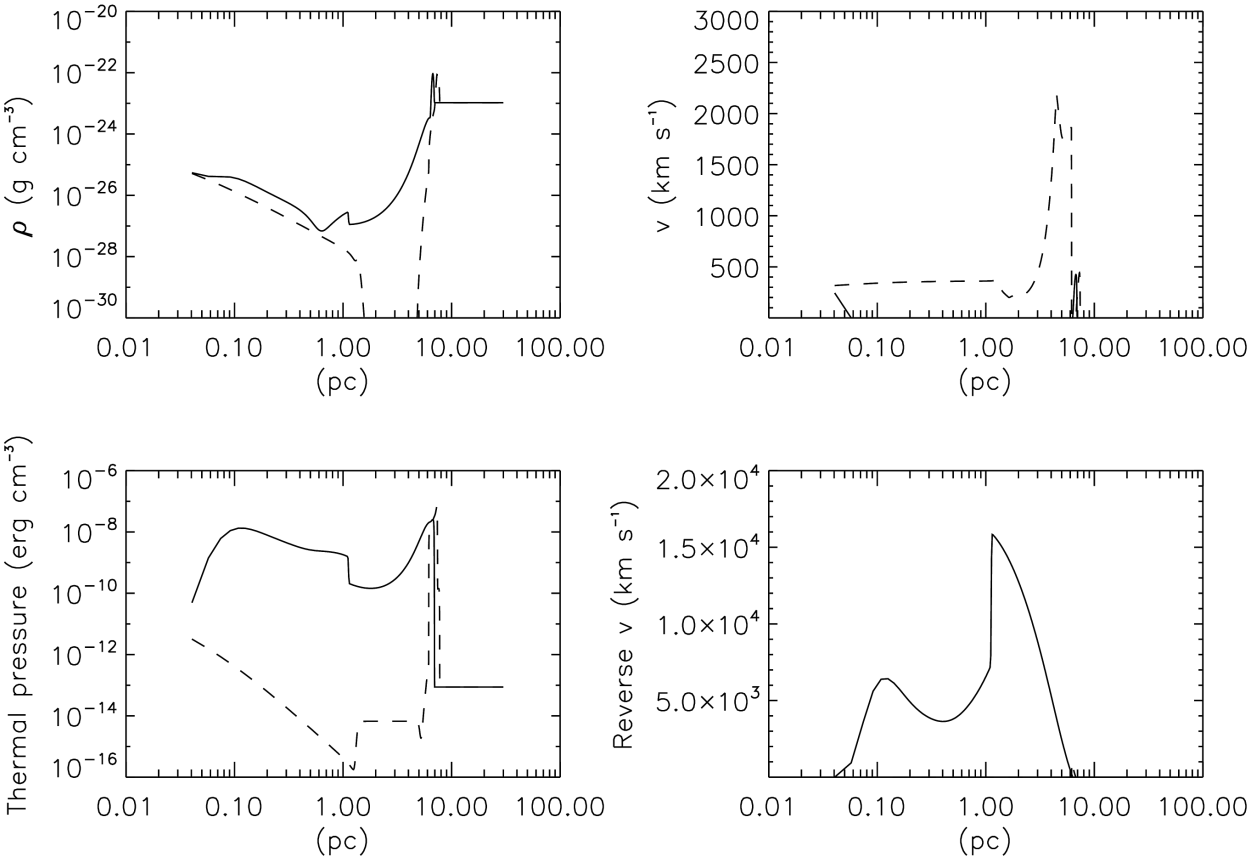

Figure 5.22: The same as Figure 5.18, but for 3.45 kyrs after the detonation of the supernova.

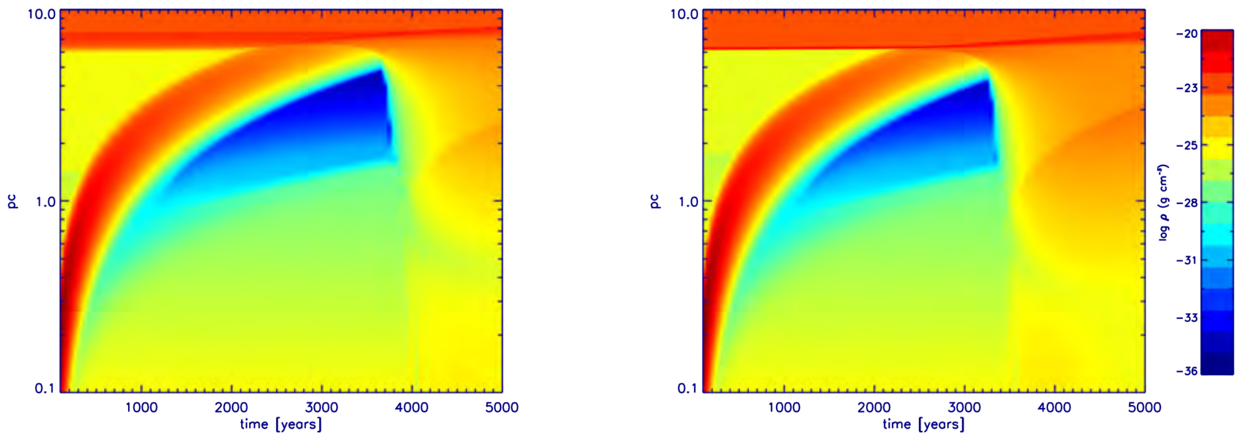

Figure 5.23: Computed contour plots of the density of a SNR evolving in a pre-existing cavity as a function of time and distance. The result without radiative cooling is shown on the left, while the result with radiative cooling is shown on the right.

Visible in the magnetic field is the OAS to be found at ≈ 6 pc. The enhanced ISM magnetic field in this region is a result of compression and is enhanced by radiative cooling.

Shown in Figure 5.24 is that the FS of the SNR interacts with the AP at ≈ 3 kyrs. The FS compresses the OAS, and this results in an increase in the OAS magnetic field. The creation of the reflected shock and the movement of the RS back toward the origin at a later stage results in the OAS magnetic field (essentially the shocked ISM magnetic field), to be dragged into the cavity. The OAS magnetic field travels inward to ≈ 4 pc from the origin at ≈ 7 kyrs. After which, the OAS magnetic field is again pushed outward due to a secondary shock travelling outward. This shock is the reflected shock reflected again off the inner boundary as shown in the density profile of Figure 5.23. The secondary shock is transmitted trough the OAS at ≈ 10 kyrs, and results in the creation of another reflected shock.

The transmission of the secondary shock through the OAS results in the compression of the OAS and an increase in the OAS magnetic field. This is more quantitatively shown in Figure 5.25. Here the ISM magnetic field is shown for 250 yrs, with a solid line, 2.8 kyrs, shown with a dashed line, 3.85 kyrs, shown with a dashed-dot line, 4.25 kyrs, shown with dot-dot-dot-dashed line, and 6 kyrs shown with a dotted line.

At 250 yrs, the solid line, the FS of the SNR has yet to interact with the ISM magnetic field, and therefore shows the enhanced ISM magnetic field, due to the interaction with the stellar wind cavity. At 2.8 kyrs, the dashed line, the FS has started to interact with OAS by compressing it. This compression leads to an enhancement of the magnetic field. This can be seen in Figure 5.25 in the dashed line where the magnetic field is enhanced to 2×10^{-5} G at 6.7 pc. Beyond 6.7 pc, the magnetic field is still the same value as in the 250 yrs result.

At 3.85 kyrs, the dot-dashed line, the FS has now completely compressed and enhanced the OAS magnetic field to values 4×10^{-5} G at 7.5 pc. At 4.25 kyrs (the dot-dot-dot-dashed line) the enhanced OAS magnetic field value drops compared to the previous time to 2×10^{-5} G at 7.7 pc as the FS has now passed the OAS, and the OAS is now decompressing, leading to a drop in the magnetic field. This decompression is further shown at 6 kyrs (the dotted line) leading to even lower values of the OAS magnetic field, peaking at slightly more then 10^{-5} G at 8.4 pc.

Figure 5.26 shows the compression ratio at the enhanced interstellar magnetic field as function of time in kyrs for the result in Figure 5.24, with radiative cooling included. The compression ratio remains constant from 0 to 3 kyrs, and is a result of the compression of the expanding and radiative cooling of the cavity, prior to the detonation of the supernova. The FS of the SNR has yet to reach the OAS of the cavity. After 3 kyrs, however, the compression ratio increases sharply reaching a value up to 13.5, before a sudden drop in the compression ratio. This is a result of the the compression caused by the FS of the SNR being transmitted through the OAS.

The sudden drop in the compression ratio, after the compression by the FS, is a result of the RS moving backward toward the origin, and dragging the field with it. This results in a compres-

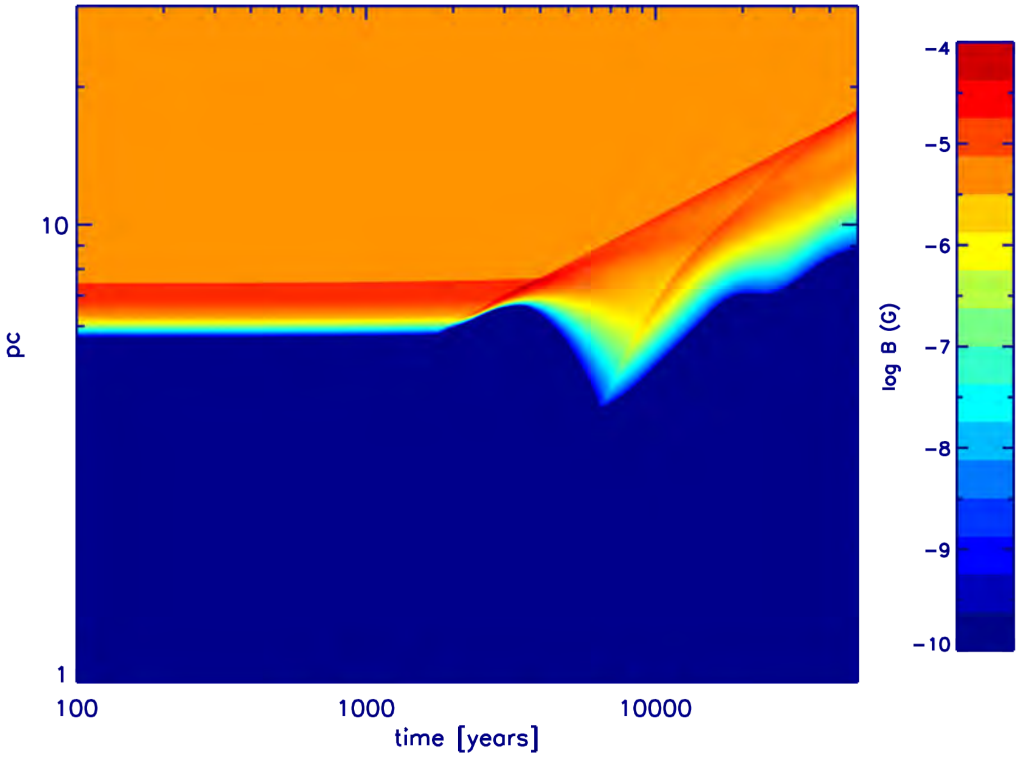

Figure 5.24: Contour plots of the ISM magnetic field of a SNR evolving in a pre existing cavity as a function of time and distance. The result is shown with radiative cooling included. The undisturbed ISM has a magnetic field 3 μG, while no stellar magnetic field is included.

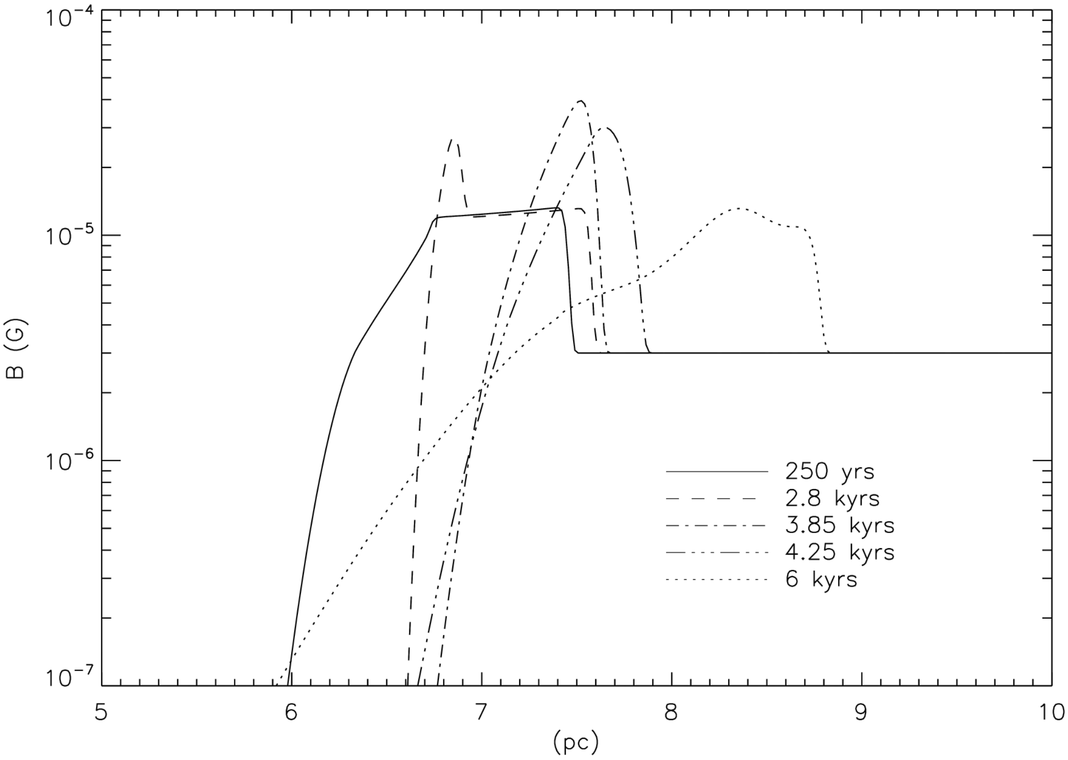

Figure 5.25: Radial plots of the computed ISM magnetic field at different times after the detonation of a SNR in a cavity. The original ISM magnetic field is 3 μG. The ISM magnetic field is shown for 250 yrs, with a solid line, 2.8 kyrs, shown with a dashed line, 3.85 kyrs, shown with a dashed-dot line, 4.25 kyrs, shown with dot-dot-dot-dashed line, and 6 kyrs shown with a dotted line.

sion ratio of $\approx$ 3.5 at 7 kyrs. Afterwards, the compression ratio increases at a relatively slow rate, reaching a value of $\approx$ 4 at 35 kyrs. This is a result of the FS still moving outward.

After 35 kyrs the compression ratio again increases. This is a result of the FS of the SNR being overtaken by secondary shocks bouncing off the inner boundary. As the secondary shock is transmitted trough the FS, it compresses the FS further, resulting in an increase in the compression ratio of the magnetic field.

5.7 The Effect of the Relative Motion of a Pre-Existing Cavity on SNR Evolution

In this section, a supernova is now detonated in a cavity with a relative motion of 90 $\mathrm{km\ s^{-1}}$, moving from right to left, as shown in Figure 4.2. The cavity is, like in the previous section, a result of an outflow with a velocity of 1500 $\mathrm{km\ s^{-1}}$ with an outflow density of $10^{-23.5}$ $\mathrm{g\ cm^{-3}}$ and temperature 10^4 K at 1.7×10^{-2} pc, assumed for the inner boundary conditions. For the ISM, a density of 1.05×10^{-23} $\mathrm{g\ cm^{-3}}$ with a temperature of 100 K is assumed. The ISM magnetic field is not considered in the computations.

The SNR evolution is shown in Figure 5.27. Shown at 950 yrs, is the early stages of the SNR. Here the FS is now interacting with OAS in the nose, while it is freely expanding in the tail region. While the supernova itself is initially spherically symmetric, it is clear at 950 yrs that the SNR is not, due to the influence of the cavity.

At 950 yrs and 1.5 kyrs, the RS is beginning to form and is initially almost spherically symmetric. However, the reverse flow back towards the center at 1.9 kyrs is not symmetric. The reverse motion starts in the nose direction and flows towards the tail. As the FS expands beyond the cavity, at 2.8 and 8 kyrs, it is clear that the SNR is not spherical. The effect of such a cavity is important to consider in simulations like these.

Figure 5.28 shows contour plots of density for a SNR evolving in a cavity, similar to that of Figure 5.27, with the relative velocity now decreased to 30 km $\mathrm{s^{-1}}$. The SNR evolution is shown at 2, 2.25, 2.5 3, 4.25, and 5 kyrs. The lower relative velocity results in a much larger and symmetric cavity than that of Figure 5.27. Also, the cavity has a closed structure in the tail direction.

At 2 kyrs, the RS starts to form, and the FS is interacting with the OAS, resulting in the compression of the OAS in the nose. At 2.25 kyrs, the interaction of the FS with the OAS has resulted in a reflected shock in the nose region. At 2.5 kyrs, the reflected shock has collided with the RS, resulting in the two moving backward towards the center. At 103 kyrs the RS in the nose region has reached the origin, while the RS in the tail region is still visible and can be found at $\approx$ -4 pc. The FS has still not interacted with the OAS in the tail region and can be found at -8 pc.

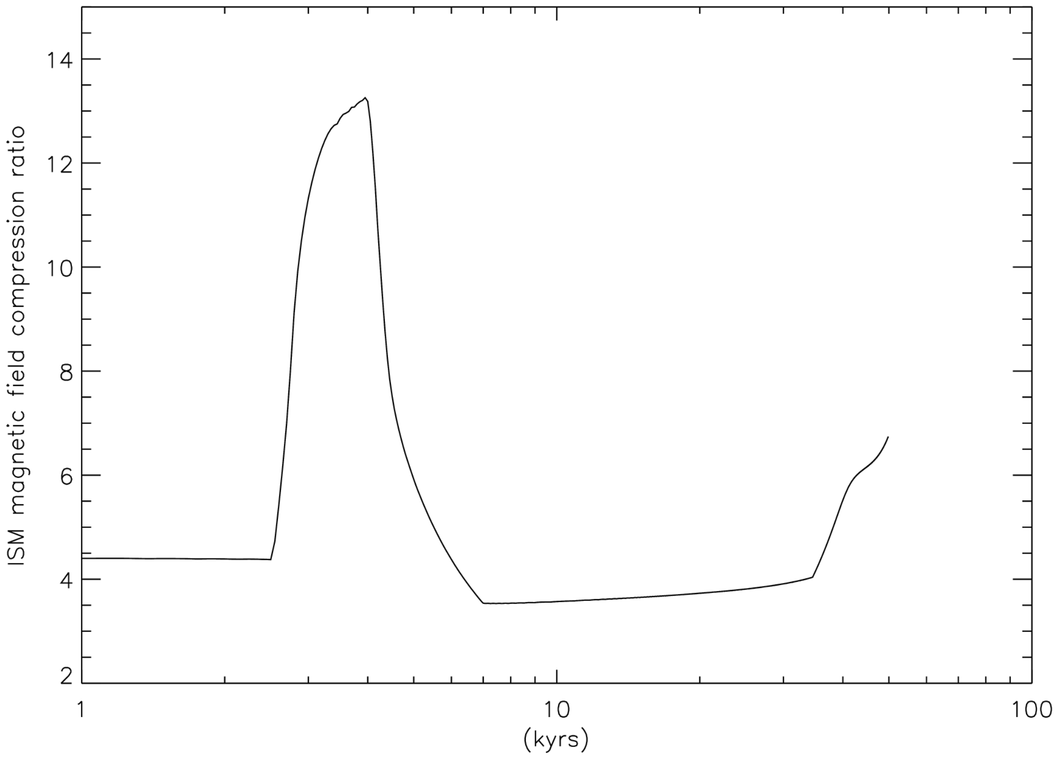

Figure 5.26: The compression ratio of the enhanced interstellar magnetic field as a function of time in kyrs for the result in Figure 5.24, with radiative cooling included.

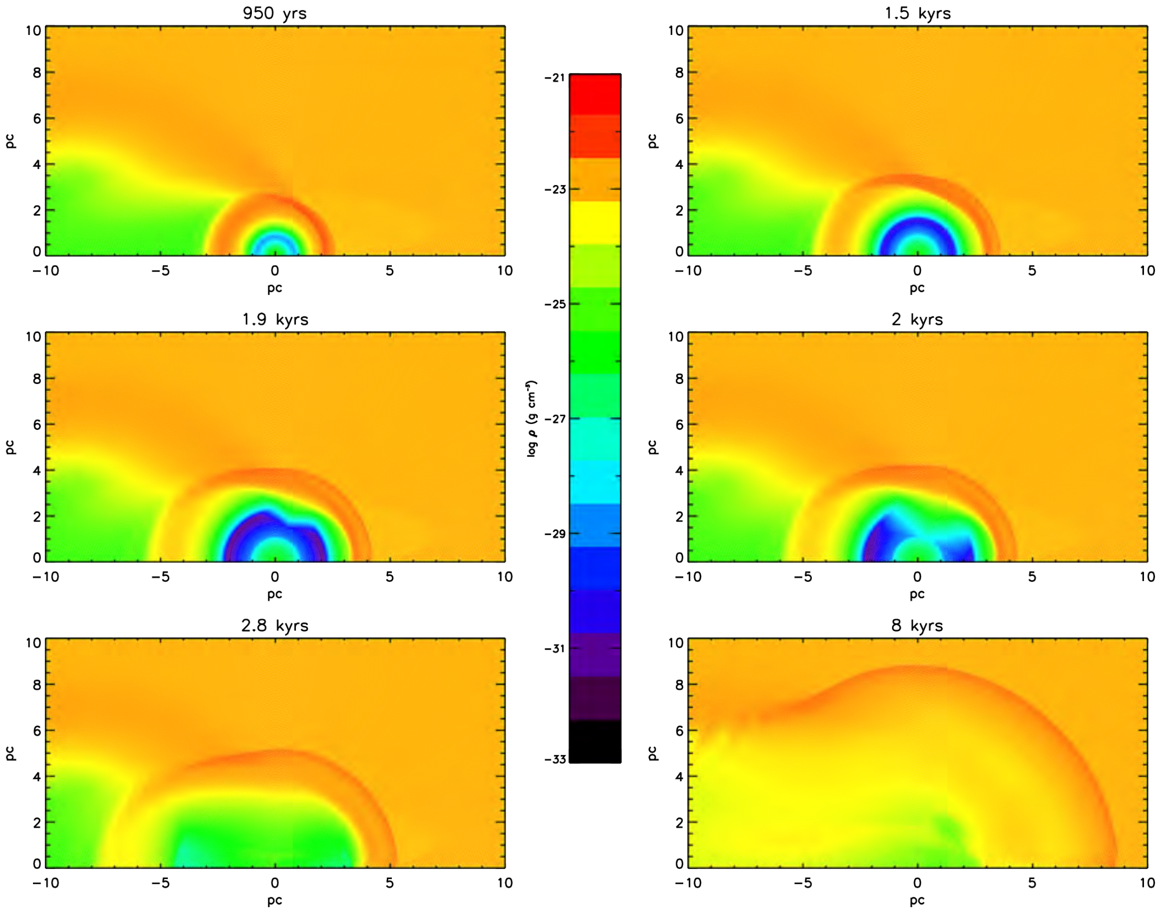

Figure 5.27: Contour plots of density of a SNR evolving in a cavity as described by Figure 4.2 at 950 yrs, 1.5, 1.9 2, 2.8, and 8 kyrs.

Not so visible, but at 4.25 kyrs in Figure 5.28, the RS in the tail region has started to move back toward the center. In the tail region, the RS moves back as described by Equation 5.8, and not as result of an interaction with the RS, formed when the FS interacts with OAS. At this time, the FS compresses the OAS in the tail region, and results in a reflected shock moving back toward the center. This reflected shock, created in the tail region, was found to move all the way to the nose of the cavity. This is seen at 15 kyrs, where this reflected shock, formed in the tail region, causes an enhancement at ≈ 5 pc in the nose direction.

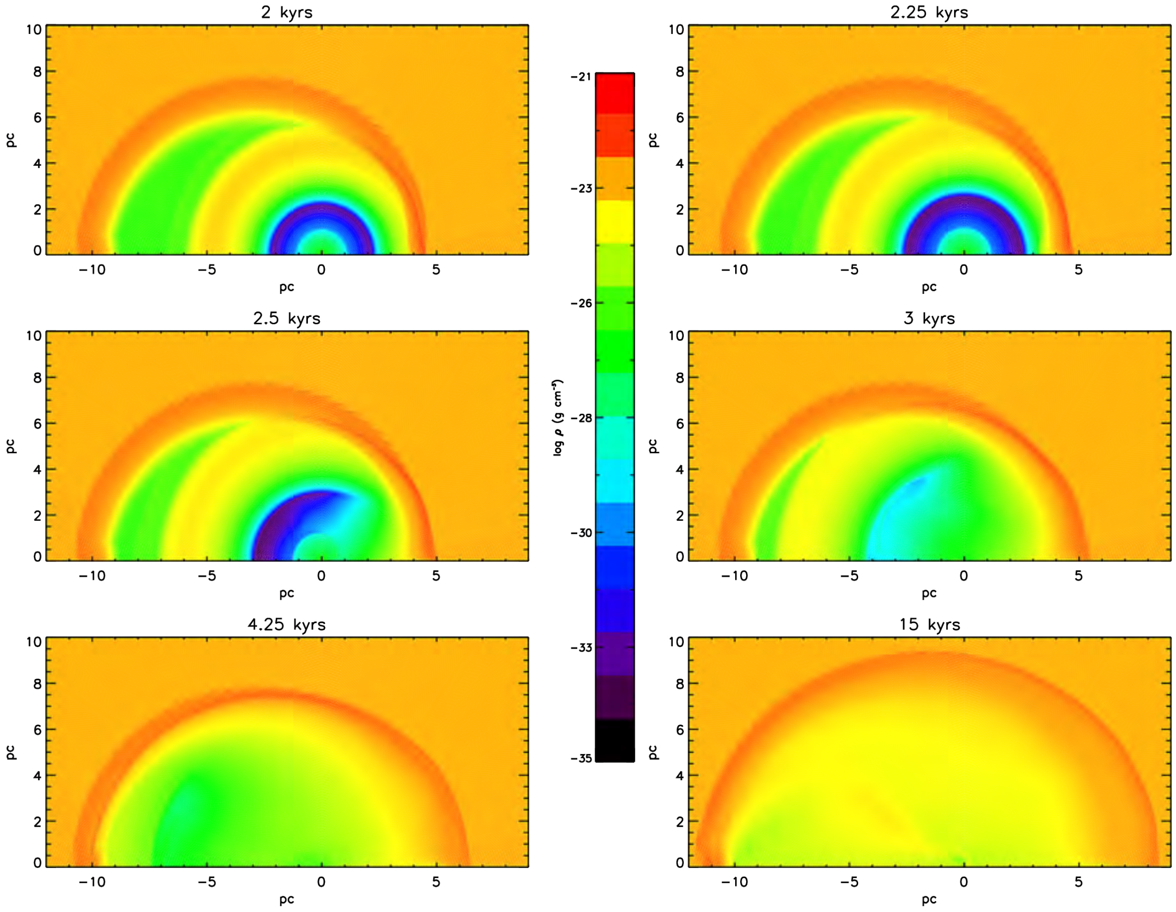

Figure 5.28: The same as Figure 5.27 but at 2, 2.25, 2.5 3, 4.25, and 15 kyrs. The relative velocity is decreased to 30 km s^{-1}.

5.8 The Effect of the Relative Motion of a Pre-Existing Cavity on SNR Evolution, Including an ISM Magnetic Field

The contour plots of the ISM magnetic field as a function of time and distance for the case of a pre existing cavity with relative motion are shown in Figure 5.29 for the case without radiative cooling and Figure 5.30 for the case with radiative cooling included. The results are shown for the nose region of the cavity.

The results without radiative cooling (Figure 5.29) again show a more uncompressed OAS magnetic field between $\approx 1.5 - 2$ pc. While the results with radiative cooling (Figure 5.30) show a more compressed and enhanced OAS magnetic field. Note that no stellar magnetic field is assumed, resulting in very low values inside the cavity.

The FS interacts with the OAS at a time ≈ 400 yrs, is transmitted trough the OAS, and enhances the OAS magnetic field. For this set of parameters, there are no clear signs of a significant reflected shock. The RS begins its movement towards the origin at ≈ 3 kyrs. The OAS magnetic field is now dragged deep into the cavity, and there are no clear signs of secondary shocks pushing the OAS magnetic field out toward the ISM.

5.9 Summary and Conclusions

In this chapter, SNR evolution is studied by computing the evolution of the blast wave Forward Shock (FS) and Reverse Shock (RS) for various scenarios. These include SNR evolution in the undisturbed interstellar medium, SNR evolution in a pre-existing cavity where radiative cooling was taken into account and where it was not, as well as the effect of the interstellar magnetic field and relative motion.

For the scenario of a SNR evolving in an uniform ISM, without the inclusion of a magnetic field, Figure 5.5 shows that after 38 kyrs, for parameters used in this study, that radiative cooling results in a more compressed FS. It is also found that radiative cooling results in the FS being closer to the center, compared to the result where radiative cooling is not taken into account, and should therefore be taken into account when simulating SNR FS evolution. This was a result of the FS loosing thermal pressure due to radiative cooling, and to balance this loss it has to move inwards. Secondary shocks are seen propagating outwards after the RS has reached the center. This is observed in results with and without radiative cooling.

It is found that a SNR evolving in a pre-existing cavity does not result in a reflected shock when the FS of the SNR interacts with the TS of the pre-existing cavity for the parameters used here, as shown in Figure 5.10. For this case, it is found that the SNR evolves considerably faster compared to the result of a SNR evolving in a uniform, undisturbed ISM, meaning, without a pre-existing cavity. This is because the SNR in the pre-existing cavity has to do a lot less work since it evolves in a lower density medium. The SNR in a uniform undisturbed ISM, however, will have to move the ISM and do more work in the process.

A further consequence of the SNR evolving in an undisturbed ISM when compared to that of the SNR evolving in a pre-existing cavity, means that it will have a higher pressure gradient. This will result in the RS starting its backwards motion towards the origin at an earlier stage than the SNR evolving in a pre-existing cavity as shown in Figure 5.12.

The interaction of the FS with AP or OAS of the scenario including a pre-existing cavity results in the creation of a transmitted and a reflected shock pair. When the reflected shock interacts with the RS, the RS starts its motion back toward the origin, as shown in Figure 5.13. This

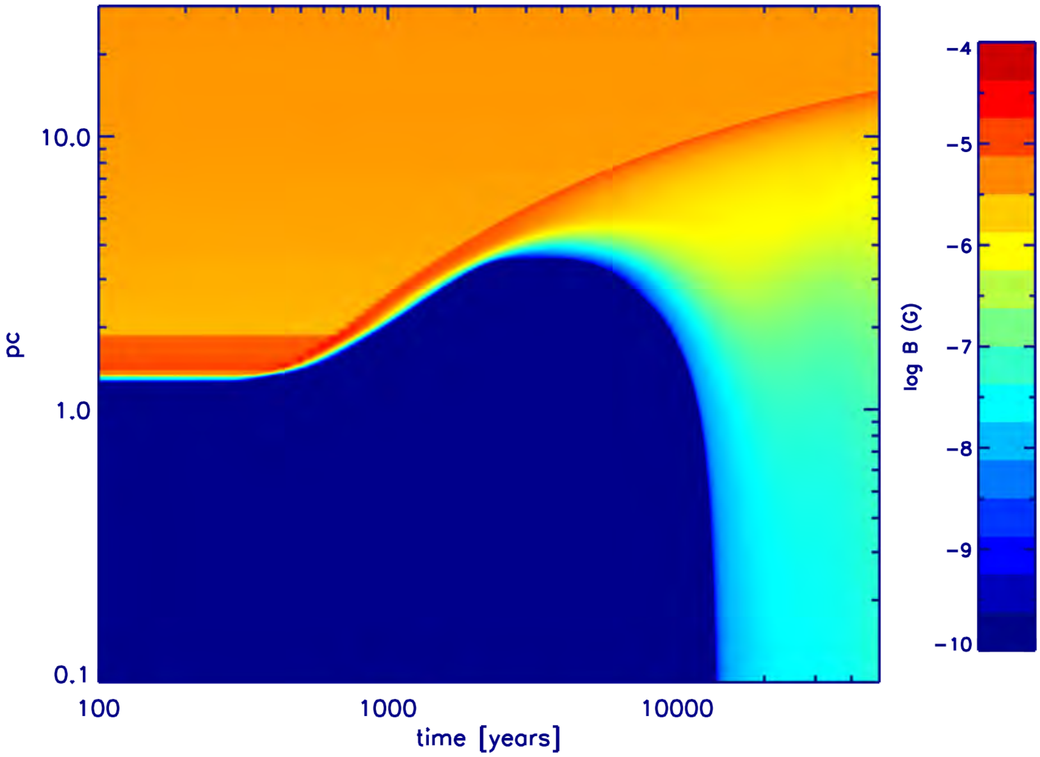

Figure 5.29: A contour plot of ISM magnetic field of a SNR evolving in a pre-existing cavity as a function of time and distance, both on a logarithmic scale. The result without radiative cooling is shown here. Relative motion is included with a velocity of 90 km s^{-1}. The results are shown only for the nose region.

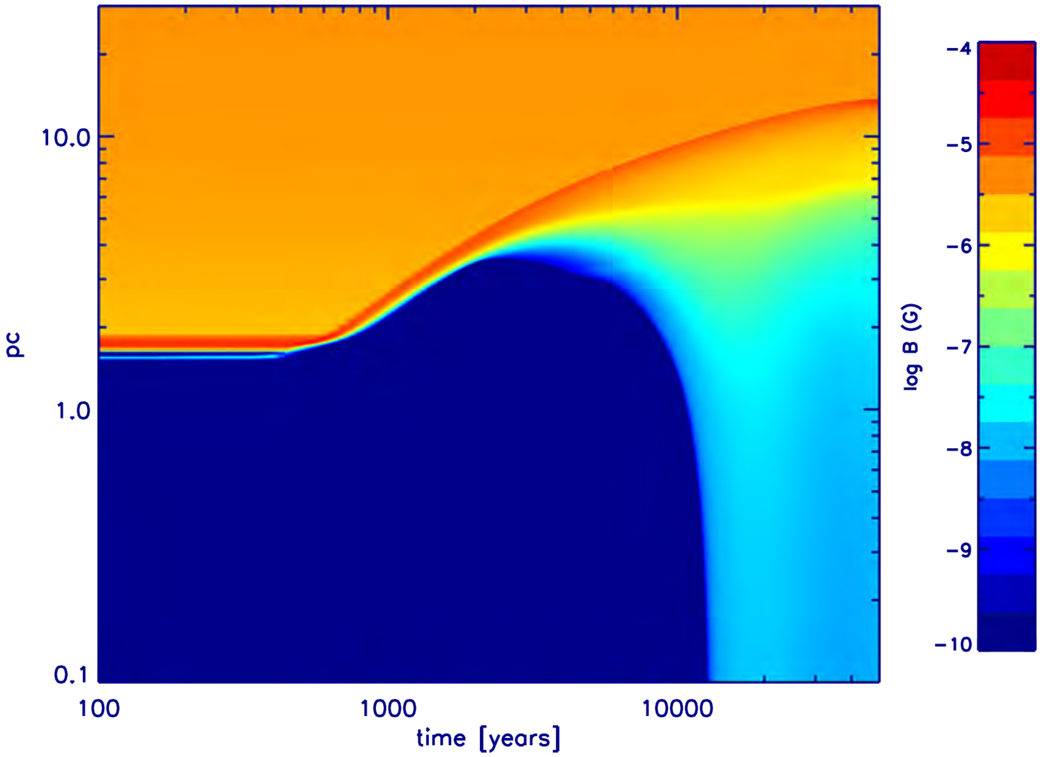

Figure 5.30: Same as in Figure 5.29, but with radiative cooling included.

backward motion is found to take place at high velocities, and is a very different mechanism compared to the backward motion of the RS for a SNR evolving in an undisturbed, uniform ISM. Again, secondary shocks are seen to emerge from the center, once the RS reaches the center, as in the scenario for the SNR evolution in a uniform, undisturbed ISM.

At much later stages, this reflected shock can collide with the BS of the pre-existing cavity, resulting in yet another reflected shock that causes the matter close to the FS to move backward. This reduces the momentum available for the outward motion of the FS, and results in a slow-down of the forward motion of the FS, as seen in Figure 5.15.

It is shown in previous chapters that when radiative cooling is included in wind blown cavities that it results in a change in the structure of the cavity. It is found that the TS is further outward, while the AP and BS are closer to the origin, compared to results where radiative cooling is not included. These structural changes in the cavity is found to influence the way in which SNRs evolve when radiative cooling is included. For instance, at early times, the FS of SNR evolving in a pre-existing cavity interacts with the TS of this cavity at an earlier time, compared to the corresponding case when radiative cooling is included. This results in the SNR evolving in a pre-existing cavity with radiative cooling included to be in the free expansion phase for longer, compared to the corresponding case without radiative cooling included.

Since the position of the AP and the BS are closer to the origin when radiative cooling is included, a reflected shock, created after the interaction of the SNR FS with the AP of the pre-existing cavity, results in the RS, moving to the origin at an earlier time than the corresponding case without radiative cooling included, as shown in Figure 5.18. The SNR evolving in a cavity with radiative cooling included, is found to enter the Sedov-Taylor phase at an earlier time than the corresponding result without radiative cooling.

The introduction of an ISM magnetic field of $3\ \mu$G to the case where the SNR evolves in an uniform ISM, meaning no pre-existing cavity, seems to have no dynamic effect on the SNR evolution at early times. This could be because the SNR is kinetically dominated, making the effect of the ISM magnetic field negligible. However, for later stages, a relatively large magnetic field might influence SNR evolution (e.g. Ferreira & de Jager, 2008).

The introduction of a pre-existing cavity and an ISM magnetic field of $3\ \mu$G, as shown in Figure 5.24, shows that the compression of the OAS of the pre-existing cavity by the SNR FS will result in a large enhancement of the OAS magnetic field to a maximum value of 4×10^{-5} G. Furthermore, the backward motion of the RS at a later stage results in the OAS magnetic field to be dragged into the cavity while being reduced to a value of 10^{-5} G. After which, the OAS magnetic field is pushed outward by secondary shocks, again reflected off the inner boundary.

These secondary shocks are then transmitted trough the OAS. This then results in the OAS being compressed and the OAS magnetic field to be enhanced again. The FS will at some point be overtaken by these secondary shocks, resulting in the transmission of the secondary shocks through the FS. This then results in a further enhancement of the magnetic field, as shown in

Figure 5.25.

The inclusion of relative motion with a pre-existing cavity creates a spherically symmetric supernova. After some time the SNR is no longer spherically symmetric. It is found that the movement of the RS back toward the origin takes place first in the nose region. It then flows towards the tail. A slower relative motion was found to create a larger cavity compared to a faster relative motion. For this case, the RS is again found to move backward towards the origin in the nose region first. In both cases, this is a result of the interaction of the reflected shock that results from the FS interaction with the OAS in the nose direction, as shown in Figure 5.28.

In the tail region, the return of the RS back toward the origin is a result of what is described using Equation 5.8, and not a result of an interaction with a reflected shock. At this time the FS compresses the OAS in the tail region, and the resulting reflection shock moves towards the origin. This reflected shock, created in the tail region, moves all the way to the nose of the cavity, as shown in Figure 5.28.

The inclusion of a SNR to a pre-existing cavity with relative motion and an ISM magnetic field of 3 μG results in an enhanced OAS magnetic field, as the FS is transmitted trough the OAS. For these parameters there are no clear signs of a reflected shock. The OAS magnetic field is dragged deep into the cavity, as the RS moves back towards the origin. As shown in Figures 5.29 and 5.30 there are, however, no clear signs of secondary shocks pushing the OAS magnetic field out toward the ISM.

Chapter 6

The Modulation of Galactic Cosmic Rays in an Astrosphere

6.1 Introduction

Cosmic rays (CRs) are considered fully ionized nuclei as well as anti-protons, electrons, and positrons that are accelerated by relativistic jets from active galactic nuclei, gamma ray bursts, blazars and supernova remnants (SNRs). See e.g., Bell (2013), Blandford et al. (2014), and Zhang & Li (2016) for discussions regarding CR acceleration. As discussed by these authors, acceleration mechanisms include unipolar inductors, diffusive shock acceleration, reconnection, and magnetoluminesence.

After being accelerated, CRs are transported through the galaxy (e.g. Moskalenko et al., 2002, Bisschoff & Potgieter, 2016) up to the their arrival at Earth. The CR spectrum as observed at Earth is shown in Figure 6.1 (from Blandford et al., 2014). The CR spectrum extends from a few MeV to the ZeV range. The lowest energy particles originate from the Sun or the surrounding heliospheric environment. From the GeV to the 100 TeV range, the particles are assumed to be mostly from galactic SNR origin (e.g. Blandford et al., 2014). Particles with energy between a few 100 TeV to a few EeV reside in what is called the knee-ankle structure. It is assumed that particles with energies above the ankle must be extragalactic in energy since their Larmor radius is larger then the size of the galaxy (e.g. Bell, 2013).

The differential energy spectrum in Figure 6.1 has a spectral index of ≈ 2.6, in the range of GeV, to a few PeV. However, below a few GeV the power-law breaks down, due to the modulation of these galactic CRs in the heliosphere. The outward convection of the solar wind with the embedded magnetic field changes the intensity of these particles as a function of time, energy and position (Parker, 1965).

Apart from galactic CRs, CRs can also be produced inside the heliosphere:

Anomalous CRs have their origin as interstellar neutrals penetrating deep into the heliosphere, getting singly ionized, transported outward with the solar wind, and inbedded in the heliospheric magnetic field up to the heliospheric termination shock and beyond where they are

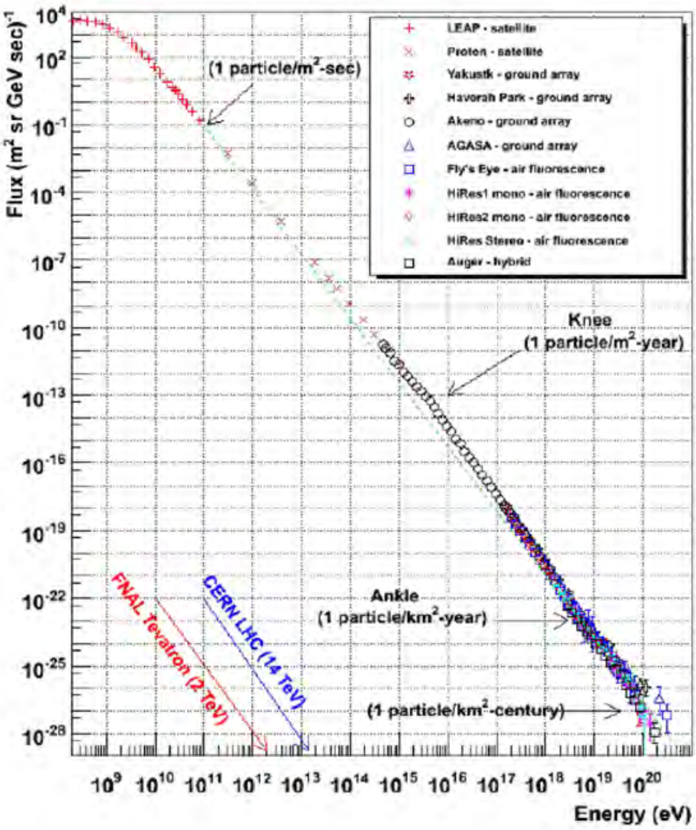

Figure 6.1: The CR spectrum from various experiments (from Blandford et al., 2014).

accelerated (e.g. Fisk et al., 1974). After they are accelerated, they are transported and modulated similar to galactic CRs. See Moraal (2014) for a recent review.

CRs from the Sun are particles produced by acceleration mechanisms in the Sun, and are more correctly referred to as solar energetic particles (e.g. Moraal, 2014). These particles are either flare accelerated, or they are found on a much more extended front in the bow shock around coronal mass ejections (Forbush, 1946).

CRs of Jovian origin refer to electrons in the $0.2 - 25$ MeV range. These electrons are released from the Jovian magnetosphere at 5 AU and their variability is caused mainly by varying heliospheric conditions (e.g. Simpson et al., 1974, Ferreira, 2005, Heber et al., 2007).

The numerical simulation of the modulation of CRs in the heliosphere has been studied extensively in the past with increasingly sophisticated models over the years. See recent work by Florinski et al. (2013), Manuel et al. (2014), Strauss & Potgieter (2014), Manuel et al. (2015), Scherer et al. (2015), Gil & Alania (2016), Luo et al. (2016), Raath et al. (2016) and Vos & Potgieter (2016), and is based on solving the Parker (1965) transport equation. This equation describes all the important physical processes, nl., diffusion, drift, convection from the expanding wind, and adiabatic energy losses, resulting from this expansion. The transport equation can be solved numerically (Florinski & Jokipii, 2003, Ferreira & Scherer, 2004, 2006). For reviews on the modelling of CRs see e.g., Potgieter (1998), Moraal (2013), Potgieter (2013) and Kóta (2013).

For the purpose of this study the modulation of galactic CRs in a stellar wind cavity is investigated. For the first time, a 1D version of the transport equation is solved numerically to study the modulation of galactic CRs in an astrosphere. Radiative cooling is implemented using the CF1 cooling function.

6.2 The Transport Equation

An equation for the distribution function f of CRs propagating through a spherically symmetric cavity as they scatter off irregularities in the heliospheric magnetic field can be written as

$$\frac{\partial f}{\partial t} = -\mathbf{V} \cdot \nabla f + \nabla \cdot (\mathbf{K} \cdot \nabla f) + \frac{p}{3} \nabla \cdot \mathbf{V} \frac{\partial f}{\partial p}, \tag{6.1}$$

where $\mathbf{V}$ is the convection velocity, and p is the momentum. This equation includes all the major transport processes that CRs may experience: diffusion, convection, drifts, and energy changes. In Equation 6.1, $\mathbf{K}$ is a diffusion tensor. In a 3D geometry this would include diffusion parallel and perpendicular to the magnetic field as well as drifts due to gradients and curvatures in the magnetic field (e.g. Engelbrecht & Burger, 2015). The diffusion tensor with drift neglected and written in a magnetic field aligned coordinate system for the heliosphere/astrosphere can be written as

$$\mathbf{K} = \begin{bmatrix} K_{\|} & 0 & 0 \\ 0 & K_{\perp\theta} & 0 \\ 0 & 0 & K_{\perp r} \end{bmatrix}, \tag{6.2}$$

where $K_{\|}$ is the diffusion coefficient parallel to a stellar/heliospheric magnetic field, $K_{\perp\theta}$ is the diffusion coefficient perpendicular to the stellar/heliospheric magnetic field in the polar direction, and $K_{\perp r}$ is the diffusion coefficient perpendicular to the magnetic field in the radial direction. The magnetic field aligned coordinate system is related to the spherical coordinate system by the following base vectors

$$\begin{aligned} \mathbf{e}_{\|} &= \cos\varphi \mathbf{e}_r - \sin\varphi \mathbf{e}_\phi \\ \mathbf{e}_1 &= \mathbf{e}_\theta \\ \mathbf{e}_2 &= \sin\varphi \mathbf{e}_\phi + \cos\varphi \mathbf{e}_r \end{aligned} \tag{6.3}$$

where $\mathbf{e}_{\|}$ is the unit vector parallel to the heliospheric magnetic field, $\mathbf{e}_1$ is the unit vector perpendicular to $\mathbf{e}_{\|}$ in the polar direction, and $\mathbf{e}_2$ is the unit vector perpendicular to $\mathbf{e}_{\|}$ in the radial direction. Furthermore, $\mathbf{e}_r$, $\mathbf{e}_\theta$, and $\mathbf{e}_\phi$ are the unit vectors in the spherical polar coordinate system while φ is the angle between $\mathbf{e}_r$ and $\mathbf{e}_\|$. By specifying the appropriate transformation matrix **T**, so that $\det(\mathbf{T}) = 1$, results in the transformation of the diffusion coefficients into spherical coordinates. This transformation matrix is given as

$$\mathbf{T} = \begin{bmatrix} \cos\varphi & 0 & \sin\varphi \\ 0 & 1 & 0 \\ -\sin\varphi & 0 & \cos\varphi \end{bmatrix} \tag{6.4}$$

from which the diffusion tensor in Equation 6.2 in spherical coordinates can be written as

$$\begin{aligned} \begin{bmatrix} K_{rr} & K_{r\theta} & K_{r\phi} \\ K_{\theta r} & K_{\theta\theta} & K_{\theta\phi} \\ K_{\phi r} & K_{\phi\theta} & K_{\phi\phi} \end{bmatrix} &= \mathbf{TKT}^T \\ &= \begin{bmatrix} \cos\varphi & 0 & \sin\varphi \\ 0 & 1 & 0 \\ -\sin\varphi & 0 & \cos\varphi \end{bmatrix} \begin{bmatrix} K_\| & 0 & 0 \\ 0 & K_{\perp\theta} & 0 \\ 0 & 0 & K_{\perp r} \end{bmatrix} \begin{bmatrix} \cos\varphi & 0 & -\sin\varphi \\ 0 & 1 & 0 \\ \sin\varphi & 0 & \cos\varphi \end{bmatrix} \\ &= \begin{bmatrix} K_\| \cos^2\varphi + K_{\perp r}\sin^2\varphi & 0 & (K_{\perp r} - K_\|)\cos\varphi\sin\varphi \\ 0 & K_{\perp\theta} & 0 \\ (K_{\perp r} - K_\|)\cos\varphi\sin\varphi & 0 & K_\|\sin^2\varphi + K_{\perp r}\cos^2\varphi \end{bmatrix}. \end{aligned} \tag{6.5}$$

Solving Equation 6.1 in only 1D (radial direction) results in the radial diffusion coefficient being written as

$$K_{rr} = K_{\perp r}\sin^2\varphi + K_\|\cos^2\varphi \tag{6.6}$$

However, as discussed in Chapter 4, only an azimuthal magnetic field is calculated so that Equation 6.6 now results in

$$K_{rr} = K_{\perp r}. \tag{6.7}$$

The transport equation can then be reduced to the following Fokker-Planck like equation

$$\frac{\partial f}{\partial t} = -V\frac{\partial f}{\partial r} + \frac{\partial}{\partial r}(K_{rr}\frac{\partial f}{\partial r}) + (\frac{\partial V}{\partial r})\frac{p}{3}\frac{\partial f}{\partial p} \tag{6.8}$$

This describes an inward radial diffusive flux that is resisted by an outward convective flux. Adiabatic energy losses in an expanding stellar wind is also taken into account.

The effective radial diffusion coefficient can be written in terms of a perpendicular diffusion mean free path

$$K_{rr} = \frac{v\lambda_{\perp}}{3}, \tag{6.9}$$

where v is the particle speed.

6.3 Stochastic Differential Equations (SDEs)

The numerical solution of Fokker-Planck equations, such as the transport equation (Parker, 1965) using SDEs is described in Yamada et al. (1998), Zhang (1999), Pei et al. (2010), Strauss et al. (2011b), Kopp et al. (2012), Strauss et al. (2013), Luo et al. (2015), and Luo et al. (2016).

For astrophysical environments such as astrospheres, little is known about the diffusion coefficients, magnetic field, and turbulence. Therefore, this work will rely much on current knowledge guided by the heliospheric example. Little is also known about the activity cycle of other stars and their stellar magnetic fields and turbulence. This work therefore limits the transport equation to one dimension, and neglecting drift effects, therefore giving a first order estimation of the CR flux, that can be found in astrospheric cavities.

The Itō-type SDEs, being equivalent to the 1D transport equation, can be written as (Gardiner, 2004)

$$\Delta r = \left(\frac{\partial K_{rr}}{\partial r} - V\right)\Delta t + \sqrt{2\kappa_{rr}}\Delta W, \tag{6.10}$$

for the time-backward case, where Δr is the change in radial distance, Δt is the time interval, and for the change in momentum

$$\Delta p = \frac{p}{3}\frac{\partial V}{\partial r}\Delta t. \tag{6.11}$$

The Wiener process is given by the standard normal distribution, η, with a mean of zero and a standard deviation of unity (e.g. Pei et al., 2010),

$$\Delta W = \eta\sqrt{\Delta t}. \tag{6.12}$$

Figure 6.2 shows the SDE solution for pseudo-particles (galactic electrons) solved in 3D in the heliospheric magnetic field, taken from Strauss et al. (2011a). Shown here is the stochastic nature of the diffusive process, as well as showing the spiral structure of the field due to the assumed diffusion coefficients discussed there.

The time constraint is chosen so that $V\Delta t_i \ll \sqrt{K_{rr}\Delta t_i}$, where $t_i = t_{i-1}+\Delta t_i$. Solving Equation 6.8 is now done by solving Equation 6.10 and Equation 6.11.

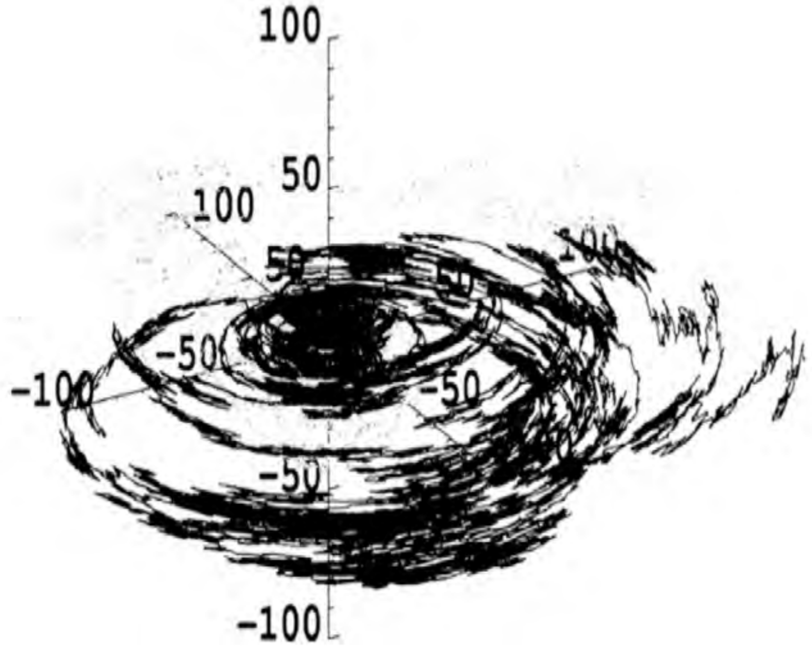

Figure 6.2: A 3D spatial representation of particle trajectories shown for the heliospheric magnetic field (from Strauss et al., 2011a).

6.4 Diffusion Coefficients

For the diffusion coefficient in Equation 6.9 it is assumed that

$$K_{rr} = \frac{C}{B}, \tag{6.13}$$

where C is some constant and B is the magnetic field of the star. This particular magnetic field dependence is roughly taken from Engelbrecht & Burger (2013) and is approximated to this simpler form since *in-situ* observations are not available. See recent work by Ferreira & Potgieter (2004), Manuel et al. (2014) and Manuel et al. (2015). The magnetic field used in the model is calculated by including the stellar magnetic field as a boundary condition in the fluid (MHD) model. Ideal MHD is then assumed, and the field is calculated by solving the induction equation (Pen et al., 2003) and ensuring $\nabla \cdot \mathbf{B} = 0$.

Results from this approach is shown in Figure 6.3 for a spherical cavity with radiative cooling not included at 40 kyrs. Here the top panel shows the computed and normalized differential intensity, at an energy of 1 GeV as a function of radial distance where the differential intensity is $j = P^2 f$ and P, is the particle rigidity. An energy dependant local interstellar spectrum is assumed, see Langner et al. (2003) and references therein. The differential intensity in Figure 6.3 shows that the galactic CRs intensities are reduced, or modulated, within the cavity at the inner boundary. The bottom panel shows the corresponding mean free path. The mean free path is smaller within the cavity compared to the value in the ISM, due to a stronger magnetic field and turbulence in this region.

Depending on the energy, a value of $10^{27} - 10^{30}$ cm^2 s^{-1} may be assumed for the diffusion coefficient in the ISM. This translates roughly to a mean free path of $0.1 - 10$ pc. Furthermore, due to limited knowledge of the magnetic field and turbulence inside the astrosphere, the heliosphere will be taken as an example to approximate a mean free path. For galactic CR protons the parallel mean free path at 1 AU is roughly $\approx$ 1 AU at 1 GeV. Assuming a magnetic field decreasing as $1/r$ will translate to a $\lambda \propto r$ dependence when assuming a $1/B$ dependence, as discussed. Therefore, at 1 pc the mean free path is estimated to be 1 pc when heliospheric values are used. Furthermore, O and B type stars, as simulated in this work, has magnetic fields $\gg$ 50 times stronger (e.g. Przybilla et al., 2016, Castro et al., 2015), leading to an estimated value of $10^3 - 10^{-2}$ pc for the mean free path at 1 pc.

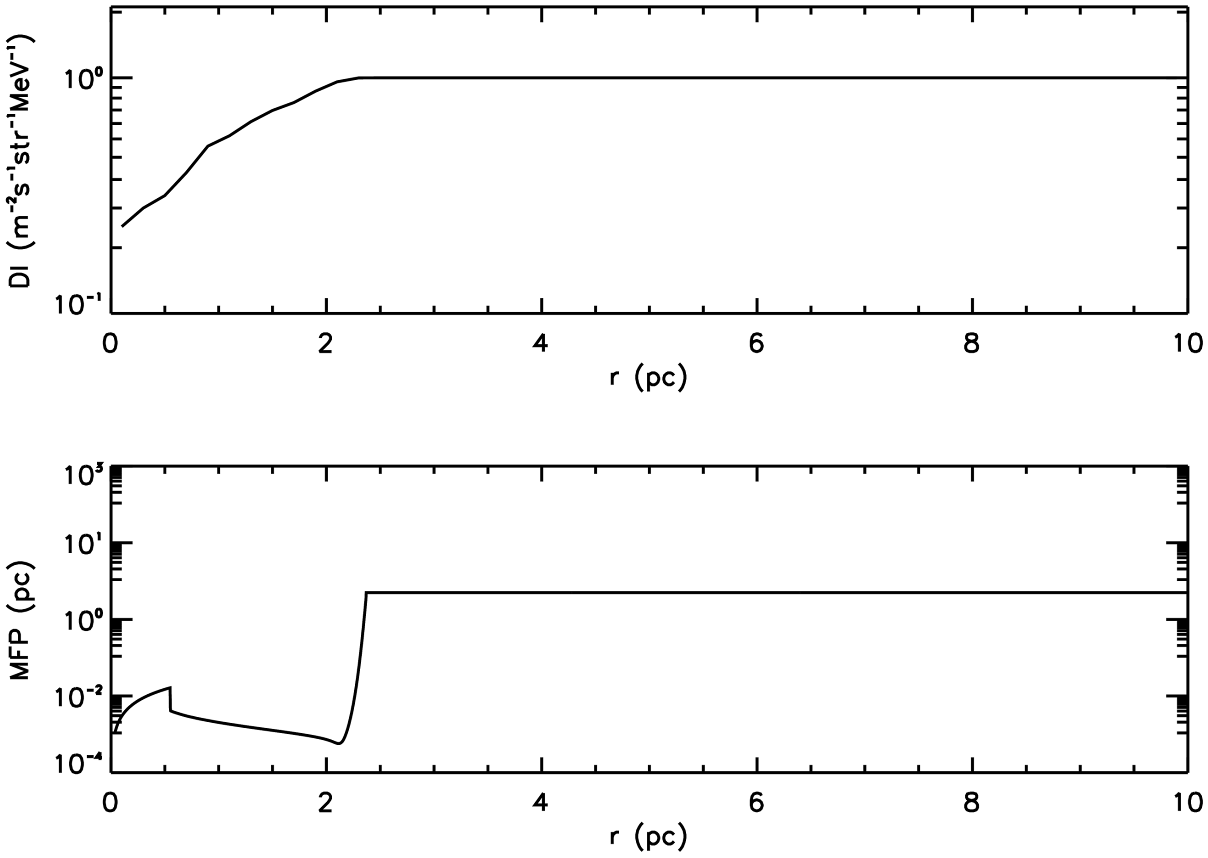

Figure 6.3: The computed and normalized differential intensity (top panel) and corresponding mean free path (bottom panel) for 1 GeV protons with an ISM magnetic field of 3 μG assumed in the astrospheric model. Radiative cooling is not taken into account.

6.5 Magnetic Field Dependence

Figure 6.4 shows the computed and normalized differential intensity (top panel) at an energy of 1 GeV and the corresponding assumed mean free path (bottom panel) for an ISM field of 3 μG (solid line), 1.5 μG (dashed line), and 0.5 μG (dot-dashed line) assumed in the astrophysical model including radiative cooling in all computations. The mean free path in the ISM is set to 5 pc and constant in all cases. Modulation is again seen to start at 2 pc, as galactic CRs cross the BS into the cavity.

In Figure 6.4 it is shown that there is not much of a difference between the three scenarios. The mean free path (bottom panel of Figure 6.4) reach the lowest values at the BS, with the smallest ISM magnetic field assumed in the astrophysical model resulting in the smallest mean free path, due to the compression that results from radiative cooling. The smaller ISM magnetic field can be more effectively compressed by the BS compared to the larger values, since the magnetic field will work against this compression. The greater compression of the ISM magnetic by the BS results in the enhancement of the magnetic field. Shown in Figure 6.4 is that there isn't much difference in the computed intensities for these energies inside the cavity for the different scenarios, because of the relative same size of the cavities.

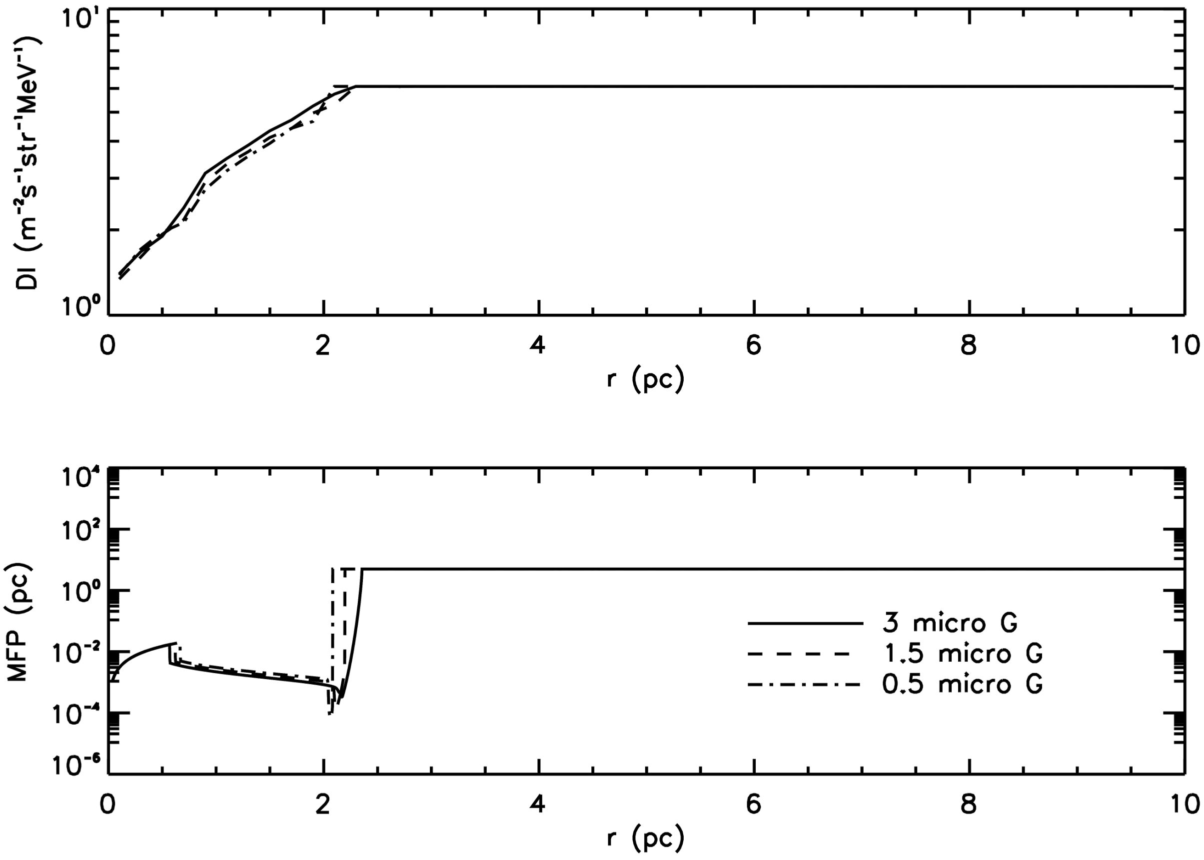

Figure 6.4: The computed and normalized differential intensity (top panel) and the corresponding mean free path (bottom panel) for 1 GeV protons. In the astrospheric model an ISM magnetic field of 3 μG (solid line), 1.5 μG (dashed line), and 0.5 μG (dot-dashed line) is assumed as different scenarios. Note that in the ISM, the mean free path is kept constant for all three scenarios. Radiative cooling is included.

6.6 The Effect of the ISM Diffusion Coefficient

The effect of the ISM mean free path on the galactic CR distribution inside an astrospheric cavity is shown in Figure 6.5, with the ISM mean free path of 50 pc shown with a dot-dashed line, and the ISM mean free path of 5 pc shown with a solid line, and an assumed ISM mean free path 0.2 pc is shown with a dashed line. The computed and normalized differential intensity is shown in the top panel, while the corresponding mean free path is again shown in the bottom panel. The computations are done for particles with energy of 1 GeV in a simulated astrosphere with radiative cooling included and an ISM magnetic field of 3 μG. Inside the astrosphere the mean free path is kept constant. The mean free path inside the cavity increases up to the TS, after which it drops due to the compression of the magnetic field in the post shock region. The mean free path at the BS falls to values of 10^{-4} pc.

Figure 6.5 shows modulation occurring inside the cavity for all scenarios. There is almost no difference between the scenarios for this set of parameters. This figure shows that the variation of the ISM mean free path or ISM magnetic field has little impact on the diffusion of galactic CRs at this energy, since the values of the differential intensity at the inner boundary in all computed cases are similar.

6.7 The Effect of Varying the Stellar Diffusion Coefficient

Figure 6.6 shows the computed results when the stellar mean free path is varied, while keeping the mean free path constant in the ISM. Results are compared to the standard result (solid line), which is the result from Figure 6.3. The dashed line shows the result of reducing the stellar mean free path by a factor of 10, compared to that of the standard result. The dot-dashed lines shows the results when the stellar mean free is increased by a factor of 10, compared to that of the standard result. Radiative cooling is included in all computations when the background astrosphere is calculated, and the galactic CR intensity is calculated at an energy of 1 GeV. The normalized differential intensity is shown in the top panel, while the corresponding mean free paths are shown in the bottom panel.

The result when the stellar diffusion coefficient is increased by a value of 10, the dashed line, shows that the mean free path increases, when compared to the standard result, up to the AP found at ≈ 2.5 pc. The differential intensity (top panel) for this result shows that the modulation is reduced when compared to the standard result.

The computations when the stellar diffusion coefficient is decreased by a factor of 10 compared to the standard result, dot-dashed line, shows that the mean free path is reduced by a factor of 10. The differential intensity shows an increase in modulation, with the value at the inner boundary decreasing by almost a factor of 100, compared to the results from Figure 6.5 (solid line) which show that the stellar diffusion coefficient has a considerable effect on the diffusion

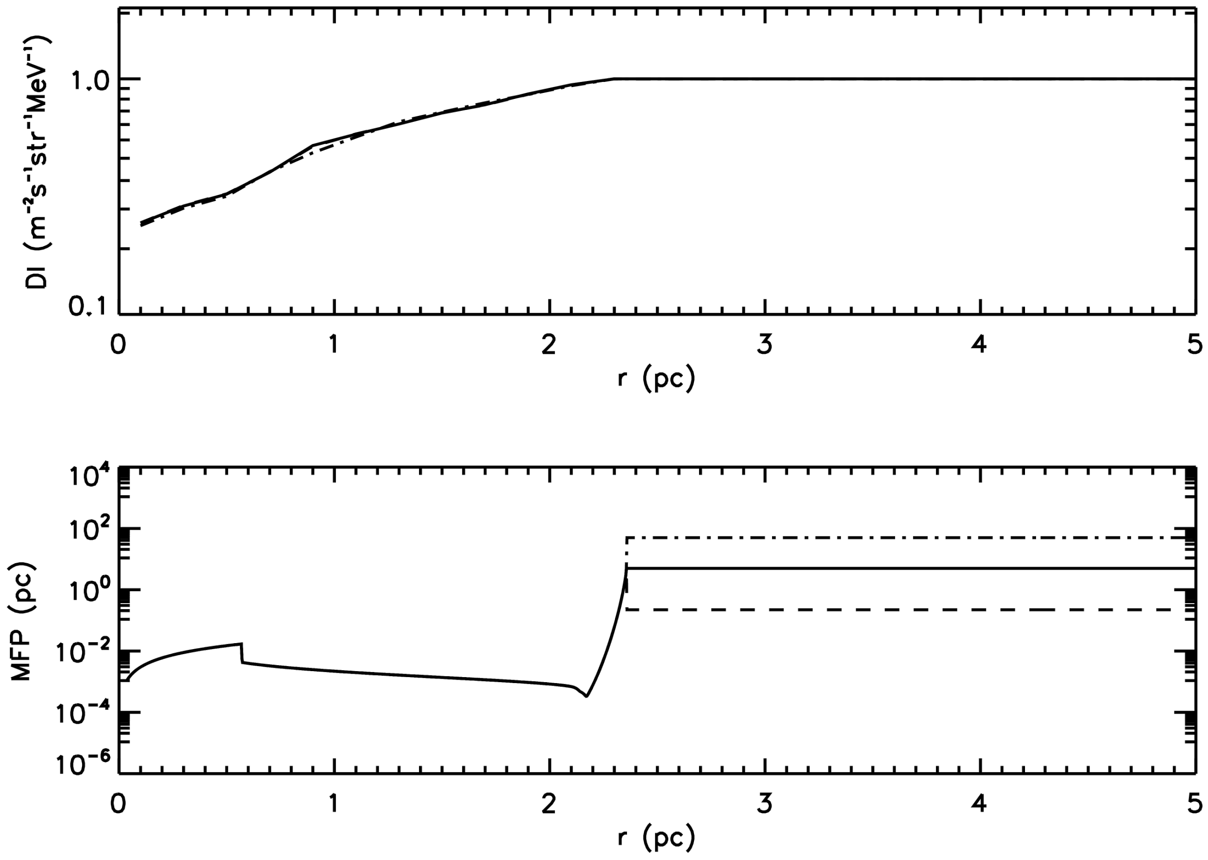

Figure 6.5: The computed and normalized differential intensity (top panel) and the corresponding mean free paths (bottom panel) for 1 GeV protons. In the astrospheric model an ISM magnetic field of 3 μG (solid line) is assumed in the astrospheric model. The ISM mean free path of 50 pc is shown with a dot-dashed line, while the scenario for an ISM mean free of 5 pc is shown with a solid line, and an ISM mean free path of 0.2 pc is shown with a dashed line. Radiative cooling is included.

of galactic CRs into the modelled astrosphere.

6.8 Galactic CR Distribution Inside Astrospheres with Radiative Cooling

The effect of radiative cooling on the distribution of GCRs inside simulated astrospheres is illustrated in Figure 6.7. The computed and normalized differential intensity shown in the top panel and the corresponding radial mean free paths are shown in the bottom panel. The dashed line shows results with radiative cooling included in the astrospheric model, while the solid line shows the results neglecting radiative cooling. An ISM magnetic field of 0.5 μG is considered in the astrosphere model and simulations are done for 40 kyrs. The particles have an energy of 10 MeV in this case.

The differential intensity when radiative cooling is included shows that modulation occurs in the cavity at $\approx$ 2.1 pc. The result without radiative cooling shows modulation in a slightly

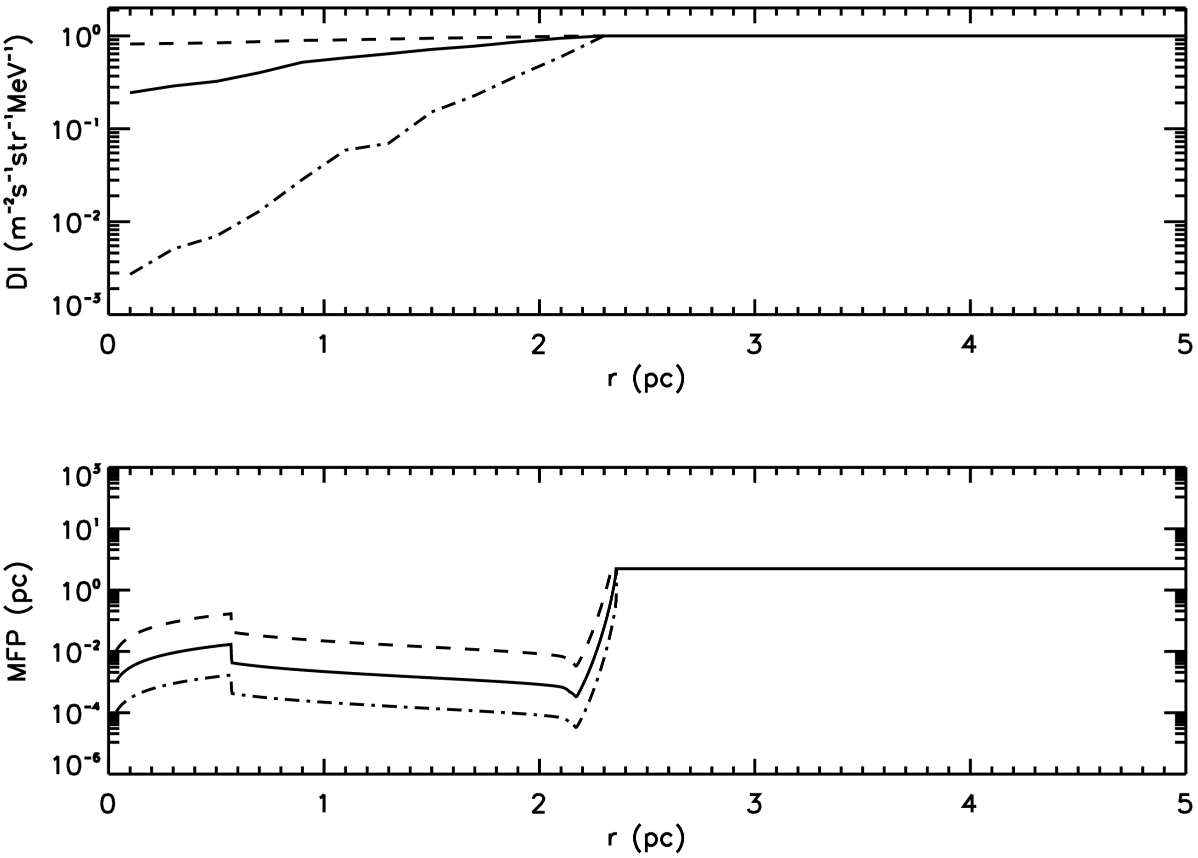

Figure 6.6: The computed and normalized differential intensity (top panel) and the corresponding mean free paths (bottom panel) for 1 GeV protons, with an ISM magnetic field of 3 μG assumed in the astrospheric model. The solid line shows the standard result, while the dashed line shows the result of reducing the stellar magnetic field by a factor of 10, compared to the standard result. The dot-dashed line shows the result when the stellar magnetic field is increased by a factor of 10, compared to the standard result of Figure 6.5 (solid line). The magnetic field was changed in the astrospheric model only. Radiative cooling is included, and results are shown for an energy of 1 GeV.

larger cavity with modulation starting at $\approx$ 2.4 pc. Furthermore, the result with radiative cooling shows slightly less modulation than the result with radiative cooling, due to the slightly larger modulation volume.

The mean free path in the IAS is also slightly larger when radiative cooling is included, while, in the supersonic wind region, before the TS (in the free expansion region), located just beyond 0.5 pc, the mean free path is the same as the result without radiative cooling. The mean free path for computations without radiative cooling assumed in the astropsheric model are reduced at the BS, located at 2.5 pc, and reaches values larger than the corresponding scenario with radiative cooling included.

In the IAS, for results with radiative cooling included, the TS is pushed further out than for the computations without radiative cooling. This then results in a lower magnetic field and density after the TS, when compared to the result without radiative cooling. The reason for

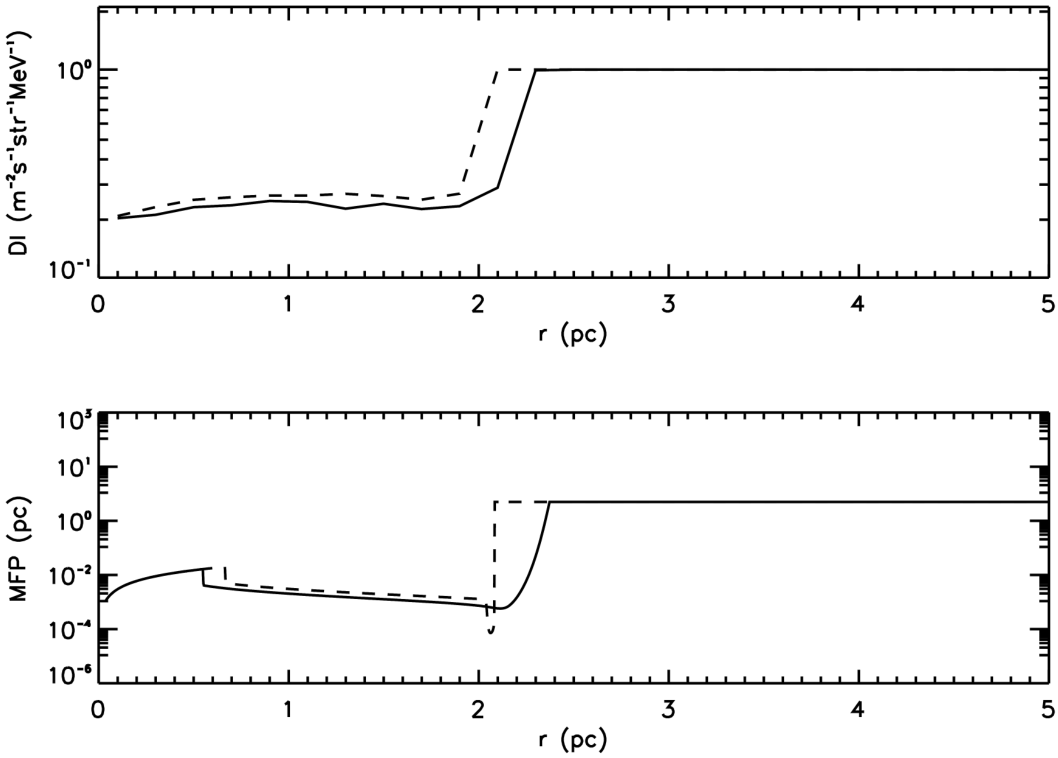

Figure 6.7: The computed and normalized differential intensity (top panel) and the corresponding mean free path (bottom panel) for 10 MeV protons, with an ISM magnetic field of 0.5 μG. The dashed line shows the computations with radiative cooling included, while solid line shows the result without considering radiative cooling.

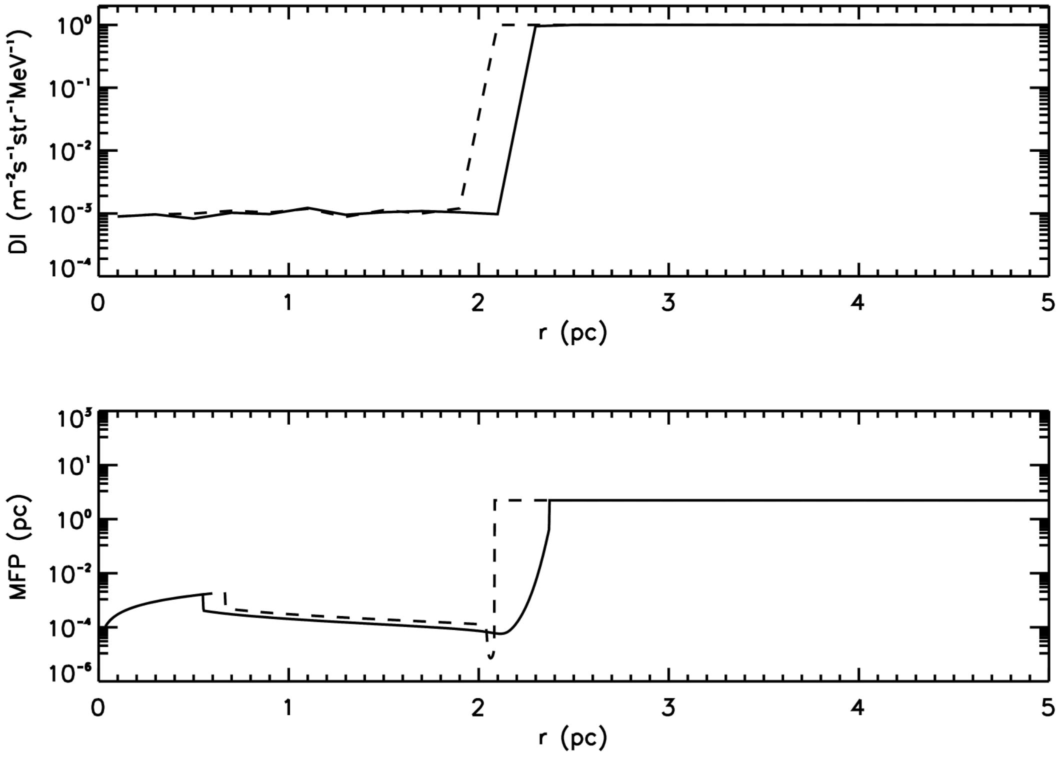

Figure 6.8: The same as in Figure 6.7, but with the stellar mean free path decreased by a factor of 10.

this is explained in earlier chapters. This lower IAS density results in a smaller enhancement of the IAS magnetic field, which in turn increases the mean free path.

The severe drop in the mean free path for the computations with radiative cooling at the BS does not result in more modulation at the BS, when compared to the results without radiative cooling at this energy. At the radiative BS, the magnetic field is significantly more enhanced when compared to results without radiative cooling. This reduces the mean free path at the BS, as noted earlier. This does not, however, result in a diffusion barrier as expected, because of the relatively large mean free paths of the galactic CRs. Also, $\nabla \cdot \mathbf{V} = 0$ implying little or no additional energy losses.

Figure 6.8 shows the same as Figure 6.7, but with the stellar mean free path decreased by a factor of 10. Correspondingly, the differential intensity at the inner boundary is reduced by a factor of more then a 100. The differential intensity in the IAS is almost exactly the same for both astropheric models. Figure 6.8 and Figure 6.7 illustrates that it is very difficult to find any signatures of radiative cooling in the CR distribution inside astrospheres.

6.9 Energy Dependence of Galactic CRs in an Expanding Astrosphere

Figure 6.9 shows the computed and normalized differential intensity at 1 TeV, as a solid line, 1 GeV, shown as a dashed line, and 10 MeV, shown as a dot-dashed line. The results were normalized to unity at the outer boundary for direct comparison. Radiative cooling is included, and an ISM magnetic field of 3 μG is assumed for the astrosphere model.

The results in Figure 6.9 show that the highest energy of 1 TeV has no modulation, while the computations for 1 GeV show modulation of a factor of ~ 4 at the inner boundary. The lowest intensities is calculated for 10 MeV, where the interstellar differential intensity is reduced by a factor of 5. This illustrates the rigidity or energy dependence of CRs modulated in an astrosphere.

Figure 6.10 shows the same as Figure 6.9, but with the stellar mean free path decreased by a factor of 10. This again results in no modulation for the results of 1 TeV protons, while the results for 1 GeV protons show an increase in modulation by a factor ~ 100 at the inner boundary. The results for 10 MeV protons show an increase of a factor of more than a 100 in modulation at the inner boundary.

Results from this work is also published by Scherer et al. (2015), using the energy dependence for the diffusion coefficients from Büsching & Potgieter (2008). Results are shown for cases where the ISM mean free path and energy of the galactic CRs are varied (Figures 6.11 and 6.12). It is found that particles with energies as high as 100 TeV are modulated, and show a similar result to what is found here namely, that higher energy galactic CRs are modulated less than those of lower energy.

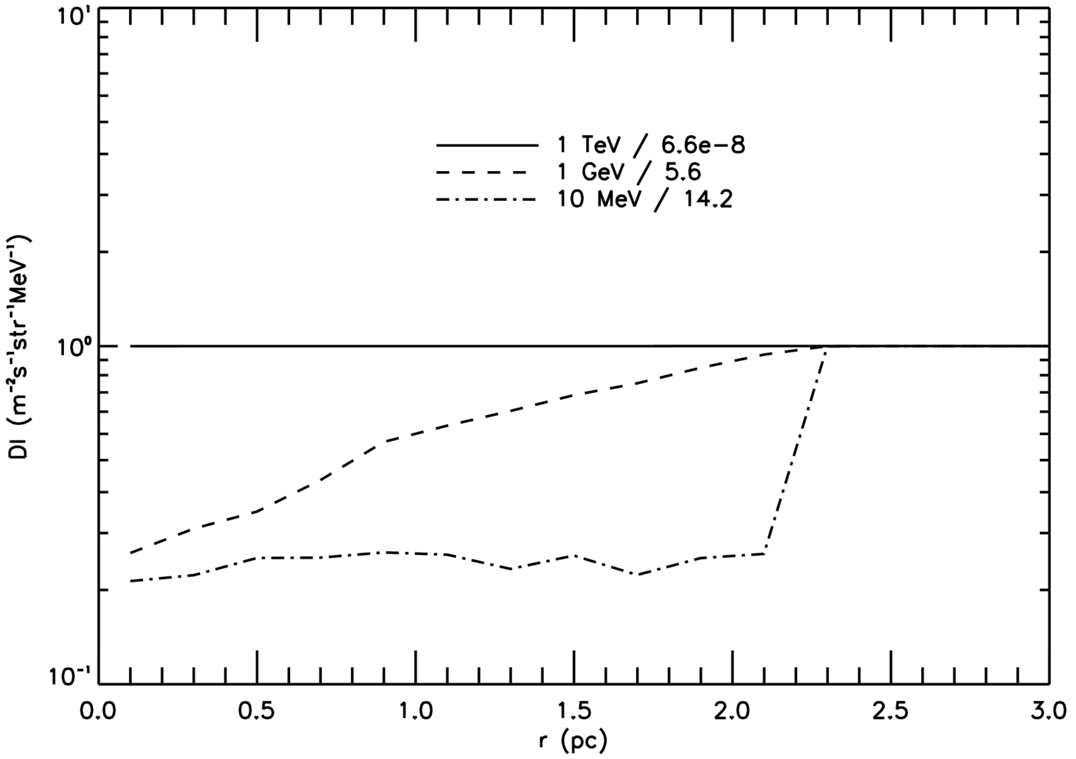

Figure 6.9: The computed and normalized differential intensity as a function of radial distance for energies of 1 TeV, 1GeV and 10 MeV. The 1 TeV result is shown with a solid line, the 1 GeV result is shown with a dashed line, and the 10 MeV result is shown with a dot-dashed line. The results are normalized so as to be able to compare the results. Radiative cooling is included while a ISM magnetic field of 3 μG is assumed in the astrospheric model.

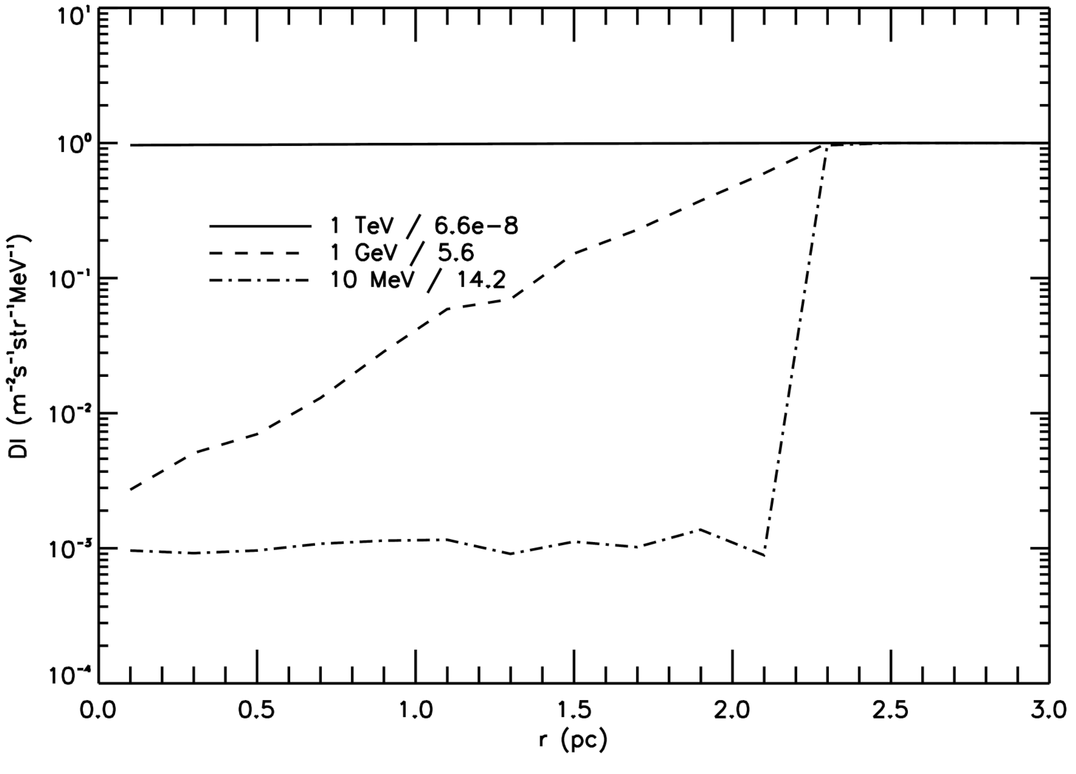

Figure 6.10: Similar to Figure 6.9, but with the stellar magnetic field increased by a factor of 10.

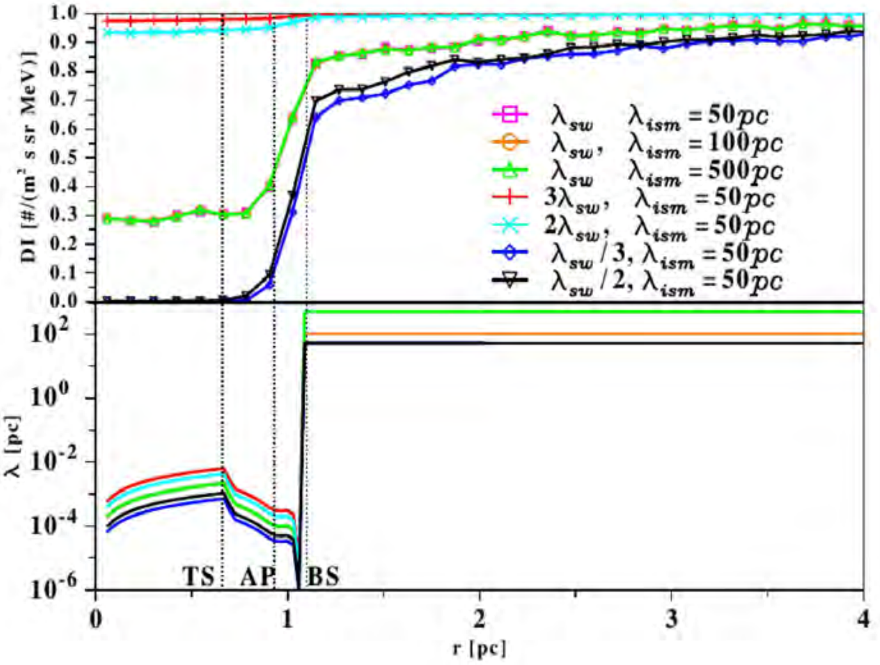

Figure 6.11: The modulation of 1 GeV galactic CRs for different ISM mean free paths (from Scherer et al., 2015). Here λ_{SW} refers to the stellar mean free path, while λ_{ISM} refers to the ISM mean free path.

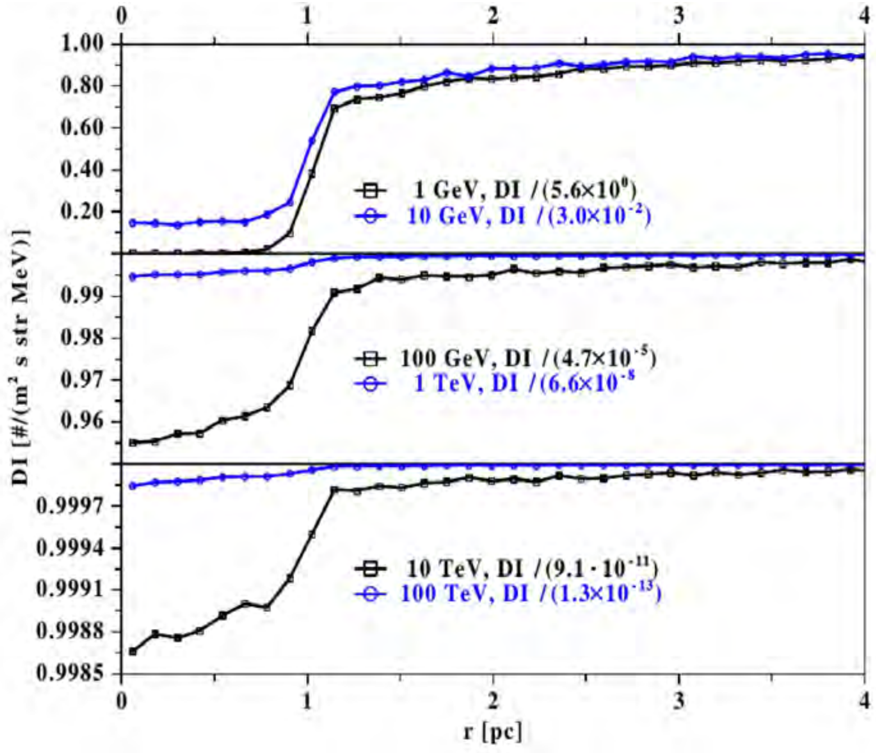

Figure 6.12: Modulation of galactic CRs with different energies (from Scherer et al., 2015).

6.10 Time Dependence of Galactic CRs in an Expanding Astrosphere

The position of the AP and TS as a function of time is shown in Figure 6.13 for two different astrospheric models, one which includes radiative cooling and one in which it is neglected. Figure 6.14 shows the computed and normalized differential intensity at 1 pc for 10 MeV protons as a function of time. In both figures, the results without radiative cooling are shown with a solid line, while results with radiative cooling are shown with a dashed line. An ISM magnetic field of 0.5 μG is included in the astrospheric computations.

The position of the AP, shown in Figure 6.13, shows that, with the inclusion of radiative cooling, the AP can move further outward as compared to the corresponding results without radiative cooling included. This is also found to be true for the TS, where the TS moves further out when radiative cooling is included than the corresponding result without radiative cooling.

The difference in the position of the AP between the results with cooling and no-cooling, explains the difference in the differential intensity at 1 pc. Since the AP moves further outward when radiative cooling is included, the modulation is slightly less than the result without radiative cooling. However, after around 30 kyrs the position of the AP seems to have little effect on the differential intensity between the two cases. This is seen in Figure 6.14.

It can be seen that both scenarios initially show little modulation, due to the small cavity. At 20 kyrs it can be seen that the result with radiative cooling is slightly less modulated than the result without radiative cooling up to about 30 kyrs. This is a result of the different positions of the AP under the influence of radiative cooling. When radiative cooling is included, the AP is further out than the corresponding result without radiative cooling.

6.11 Summary and Conclusions

The aim of this chapter was to study the transport and modulation of galactic CRs inside astrospheric cavities. This is done by varying the ISM diffusion coefficient and the stellar diffusion coefficient. The effect of radiative cooling is included, and the energy dependence of galactic CRs in an expanding astrosphere as well as the time dependence of galactic CRs is studied.

When the ISM magnetic field is varied in the astrospherical model it showed that the corresponding mean free path reaches its lowest values at the BS, as was shown in Figure 6.5. As shown in Figure 6.5, the modulation of galactic CRs was found to not be sensitive to the values of the ISM diffusion coefficients, for the parameters used here. The stellar mean free path increases inside the cavity up to the TS, where its value drops, due to the enhancement of the stellar magnetic field caused by the compression of the TS. For the parameters used in this study, it was found that the diffusion of galactic CRs into an astrosphere is sensitive to the stellar mean free path.

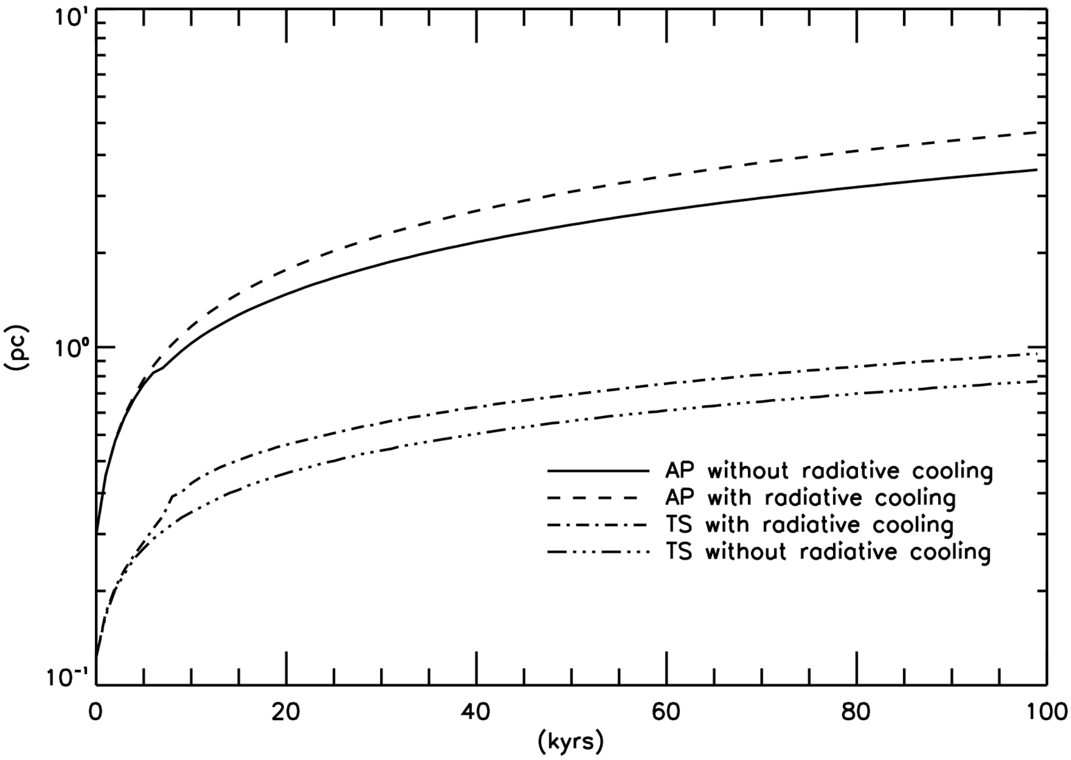

Figure 6.13: The position of the AP position as a function of time for results without radiative cooling (solid line), and results with radiative cooling (dashed line). The TS position is also shown with a dot-dot-dot-dashed line for results without radiative cooling, and a dot-dashed line for results with radiative cooling. An ISM magnetic field of 0.5 μG is included in the computations.

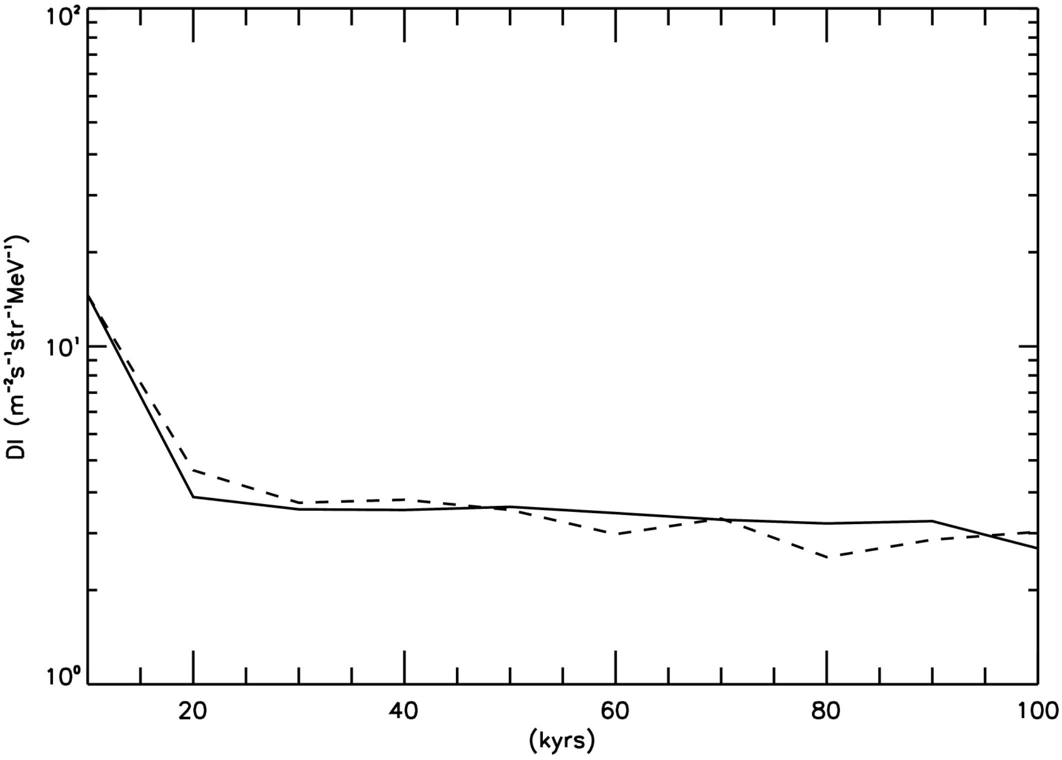

Figure 6.14: The differential intensity at 1 pc as a function of time for 10 MeV protons with an ISM magnetic field of 0.5 μG. The dashed line shows the computations with radiative cooling included, while the solid line shows the result without considering radiative cooling.

The inclusion of radiative cooling show that galactic CRs would have to diffuse into a slightly larger cavity than when radiative cooling is not included, as is shown in Figures 6.7 and 6.8. Results with radiative cooling show sightly less modulation than results without radiative cooling, due to the slightly larger modulation volume.

Modulation is seen to be dependent on the energy of the particles for the parameters used here. It is found that higher energies show little or no modulation, while lower energies show more modulation. The position of the AP is shown in Figure 6.13, and is found to be further out when radiative cooling is included, and is seen to be significant for time dependent diffusion of galactic CRs into an astrosphere. Since the AP is further out when radiative cooling is included, the modulation will be slightly reduced when compared to the result without radiative cooling as can be seen in Figure 6.14. The impact of the AP is only seen at the early stage up to about 30 kyrs. After this time, the position of the AP seems to result in little difference between results with radiative cooling and those without. This shows that the change in the structure caused by radiative cooling can affect the modulation of CRs.

Chapter 7

Summary and Conclusions

The aim of this work is to present numerical simulations of astrospheres, including radiative cooling. The effect of these pre-existing cavities on supernova remnant (SNR) evolution is also presented, as well as cosmic ray (CR) transport in these cavities.

As a first step, to illustrate the effect of radiative cooling on computed astrospheric cavities, it is assumed that the outflow is spherically symmetric and the interstellar medium (ISM) is considered uniform with no relative motion. For a pure hydrodynamical solution it is found that the effects of radiative cooling become important early in the evolution of the cavity. The choice of cooling function is shown to not be trivial, since this choice affected the geometrical extent of the cavity, e.g. the position of the termination shock, bow shock, and astropause. The compression ratio at the bow shock is also shown to vary with the choice of cooling function.

It is shown that radiative cooling does not affect the compression ratio at the termination shock (TS), since cooling is not dynamically important at this point. This is a result of the high outflow velocity and low density of the shocked wind. Both these factors result in the increase of the cooling time. Radiative cooling is found to be important at the BS, where the shock velocity is sufficiently low and results in a low cooling time. Radiative cooling is also affected by the choice of ISM density, with lower ISM densities increasing the cooling time.

It is also found that, depending on the parameters assumed, including the effects of radiative cooling results in the creation of a fine structure in the outer astrosheath. This fine structure can be described as the hot outer astrosheath and the cool outer astrosheath. The hot outer astrosheath is found directly after the bow shock (BS), while the cool outer astrosheath can be found closer to the astropause (AP). This is a result of the hot shocked plasma having sufficient time to cool radiatively resulting in a cool plasma closer to the AP.

The compression ratio is also shown to be a function of ISM density, and varied significantly with choice of cooling function. The highest maximum compression ratio is found for the lowest ISM density values. This indicates the differences in cooling times for different cooling functions, and different ISM densities.

The effect of the ISM magnetic field on the astrospheric evolution, including radiative cooling, is shown by adding a 3 μG and a 0.5 μG magnetic field to the model. The stellar magnetic field is not taken into account. It is found that the magnetic field reduces the compression of the outer astrospheath (OAS) that results from radiative cooling. This lack of compression lowers the density, making radiative cooling less effective.

The compression ratio is shown as a function of ISM density for the case of including an ISM magnetic field. The results with the magnetic field are found to be very different. Once cooling has set in, it is found that the compression ratio increases with ISM density. This is the opposite of what is found for the pure hydrodynamic solutions. This is because the magnetic pressure dominates at lower ISM densities and then resists the compression. At higher ISM densities, the thermal pressure dominates and radiative cooling becomes more effective. It is found that radiative cooling, using different cooling functions, can behave very differently when the magnetic field is included.

In conclusion, it is found that the choice of cooling functions influences the positions of the TS, AP, and BS, as well as the geometric extent of the cavity. It further influences the compression ratio that results from radiative cooling in the cold outer astrosheath. When the ISM magnetic field is included, it reduces the compression ratio of the cold outer astrosheath. It is found that the choice of cooling function is not trivial, and should be considered when including radiative cooling into hydrodynamic or MHD simulations.

The inclusion of the relative motion of a star results in a bullet shaped structure of its cavity. The additional ram pressure of relative motion pushes back the TS and AP. The ISM has to navigate past the cavity created by the stellar wind, and if it moves supersonically, it creates a BS. Including an ISM magnetic field increases the extent of the OAS, and is caused by the additional magnetic pressure. The TS is closer to the star in the nose direction, as a result of the added magnetic pressure. When radiative cooling is included, the TS moves further away from the star, and the OAS thickness is also reduced. This is again a result of the drop in the thermal pressure of the OAS, caused by radiative cooling.

Adding relative motion with the ISM magnetic field, decreases the expanding shock velocity, which decreases the cooling time, and results in more cooling and an increase of the compression ratio, when compared to the result without relative motion. When the magnetic pressure of the OAS starts to dominate, due to the compression, the OAS expands. When the ISM magnetic field is included it is found that the compression ratio is considerably less than found without the ISM magnetic field. As found previously, the magnetic field resists the compression caused by radiative cooling.

Supernova remnant (SNR) evolution in these pre-existing cavities is studied by computing the evolution of the blast wave forward shock (FS) and reverse shock (RS) for various scenarios. These include SNR evolution in the undisturbed interstellar medium, and SNR evolution in a pre-existing cavity where radiative cooling is taken into account and where it is not, as well as the effect of the interstellar magnetic field and the relative motion.

The scenario of a SNR evolving in a uniform ISM, without the inclusion of a magnetic field, showed for parameters used in this study, that radiative cooling results in a more compressed FS after 38 kyrs of simulation time. It is also found that radiative cooling results in the FS being closer to the center, compared to the result where radiative cooling is not taken into account. This is a result of the FS loosing thermal pressure, due to radiative cooling, and to balance this loss, it has to move inwards.

It is found that a SNR evolving in a pre-existing cavity evolves considerable faster compared to the result of a SNR evolving in a uniform, undisturbed ISM; meaning, without a pre-existing cavity. This is because the SNR in the pre-existing cavity has to do a lot less work, since it evolves in a lower density medium. The SNR in a uniform undisturbed ISM, however, will have to move the ISM and do more work during the process. A further consequence of the SNR evolving in an undisturbed ISM is that it will have a larger pressure gradient behind the FS. This results in the RS starting its backward motion towards the origin at an earlier stage than the SNR evolving in a pre-existing cavity.

The interaction of the FS with the AP or OAS of the scenario, including a pre-existing astrospheric cavity, results in the creation of a transmitted and a reflected shock pair. When the reflected shock interacts with the RS of the SNR the RS starts its motion back towards the origin. This backward motion is found to take place at high velocities, and is a very different mechanism compared to the backward motion of the RS for a SNR evolving in an undisturbed, uniform ISM. At much later stages, this reflected shock can collide with the BS of the pre-existing cavity, resulting in yet another reflected shock that causes the matter close to the FS to move backward. This reduces the momentum available for the outward motion of the FS, and results in a slow-down of the forward motion of the FS.

As mentioned above, when radiative cooling is included in wind blown cavities, it results in a change in the structure of the cavity. The TS is further outward, while the AP and BS are closer to the origin, compared to results where radiative cooling is not included. These structural changes in the cavity influence the way in which SNRs evolve when radiative cooling is included. For instance, at early times, the FS of SNR evolving in a pre-existing cavity interacts with the TS of this cavity at an earlier time compared to the corresponding case when radiative cooling is included. This results in the SNR evolving in a pre-existing cavity with radiative cooling included to be in the free expansion phase for longer compared to corresponding case without radiative cooling.

Since the position of the AP and the BS are closer to the origin when radiative cooling is included, it means that a reflected shock, created after the interaction of the SNR FS with the AP of the pre-existing cavity results in the RS moving to the origin at an earlier time than the corresponding case without radiative cooling included. The SNR evolving in a cavity with radiative cooling included is found to enter the Sedov-Taylor phase at an earlier time than the corresponding result without radiative cooling.

The introduction of a pre-existing cavity and an ISM magnetic field of 3 μG shows that the compression of the OAS of the pre-existing cavity by the SNR FS results in a large enhancement of the OAS magnetic field. Furthermore, the backward motion of the RS at a later stage causes the OAS magnetic field to be dragged into the cavity while being reduced to a value of 10 μG. After this, the OAS magnetic field is pushed outward by secondary shocks, and again reflected off the inner boundary.

These secondary shocks are then transmitted through the OAS. This then results in the OAS being compressed and causes the OAS magnetic field to be enhanced again. The FS will at some point be overtaken by these secondary shocks, resulting in the transmission of the secondary shocks through the FS. This then results in a further enhancement of the magnetic field.

It is also shown that the inclusion of relative motion with a pre-existing cavity results in a non-spherical SNR. It is found that the movement of the RS back toward the origin takes place first in the nose region. It then flows toward the tail. This is dependent on the relative motion. A slower relative motion is found to create a larger cavity compared to a faster relative motion. In the tail region, the return of the RS back toward the origin is not a result of an interaction with a reflected shock, as in the nose direction.

The transport of galactic CRs inside astrospheric cavities is also investigated. This is done by using the cavities, as described above, as input into the stochastic differential equation (SDE) transport code. The effect of the different parameters are shown by varying the ISM diffusion coefficient and the stellar diffusion coefficient. The effect of radiative cooling and the energy dependence of galactic CRs in an expanding astrosphere are also shown.

The modulation of galactic CRs is found to not be sensitive to the ISM diffusion coefficients for the parameters assumed. However, it is found that the diffusion of galactic CRs into an astrosphere is sensitive to the stellar mean free path. The inclusion of radiative cooling shows that galactic CRs would have to diffuse into a slightly larger cavity when radiative cooling is not included. The results with radiative cooling assumed in the model when the cavity is calculated show sightly less modulation than results without radiative cooling, due to the slightly larger modulation volume.

Modulation is seen to be dependent on the energy of the particles for the parameters used here. It is found that higher energies show little modulation, while lower energies show more modulation. The modulation is again found to be sensitive to the assumed stellar mean free path.

Parts of this work is published in Scherer et al. (2015).

Bibliography

Arthur, S. J. 2007, in Revista Mexicana de Astronomia y Astrofisica Conference Series, Vol. 30, Revista Mexicana de Astronomia y Astrofisica Conference Series, 64

Axford, W. I., Dessler, A. J., & Gottlieb, B. 1963, Termination of Solar Wind and Solar Magnetic Field., ApJ, 137, 1268

Bell, A. 2013, Cosmic ray acceleration, Astroparticle Physics, 43, 56, seeing the High-Energy Universe with the Cherenkov Telescope Array - The Science Explored with the CTA

Ben-Dor, G. 2007, Shock Wave Reflection Phenomena, Shock Wave and High Pressure Phenomena (Springer Berlin Heidelberg)

Bertschinger, E. 1986, On the structure and stability of radiative shock waves, ApJ, 304, 154

Bisschoff, D. & Potgieter, M. S. 2016, New local interstellar spectra for protons, helium and carbon derived from PAMELA and Voyager 1 observations, Astrophys. Space Sci., 361, 48

Blandford, R., Simeon, P., & Yuan, Y. 2014, Cosmic Ray Origins: An Introduction, Nuclear Physics B Proceedings Supplements, 256, 9

Broersen, S., Chiotellis, A., Vink, J., & Bamba, A. 2014, The many sides of RCW 86: a Type Ia supernova remnant evolving in its progenitor's wind bubble, M.N.R.A.S, 441, 3040

Büsching, I. & Potgieter, M. S. 2008, The variability of the proton cosmic ray flux on the Sun's way around the galactic center, Advances in Space Research, 42, 504

Castro, N., Fossati, L., Hubrig, S., Simón-Díaz, S., Schöller, M., Ilyin, I., Carrol, T. A., Langer, N., Morel, T., Schneider, F. R. N., Przybilla, N., Herrero, A., de Koter, A., Oskinova, L. M., Reisenegger, A., Sana, H., & BOB Collaboration. 2015, B fields in OB stars (BOB). Detection of a strong magnetic field in the O9.7 V star HD 54879, Astron. Astrophys., 581, A81

Chen, Y., Zhang, F., Williams, R. M., & Wang, Q. D. 2003, Supernova Remnant Crossing a Density Jump: A Thin-Shell Model, ApJ, 595, 227

Chevalier, R. A. & Imamura, J. N. 1982, Linear analysis of an oscillatory instability of radiative shock waves, ApJ, 261, 543

Chevalier, R. A. & Liang, E. P. 1989, The interaction of supernovae with circumstellar bubbles, ApJ, 344, 332

Cho, H. & Kang, H. 2008, Feedback from multiple supernova explosions inside a wind-blown bubble, New Astron, 13, 163

Chu, Y. H. 2008, in IAU Symposium, Vol. 250, Massive Stars as Cosmic Engines, ed. F. Bresolin, P. A. Crowther, & J. Puls, 341

Cioffi, D. F., McKee, C. F., & Bertschinger, E. 1988, Dynamics of radiative supernova remnants, ApJ, 334, 252

Crowther, P. A. 2001, in Astrophysics and Space Science Library, Vol. 264, The Influence of Binaries on Stellar Population Studies, ed. D. Vanbeveren, 215

Dalgarno, A. & McCray, R. A. 1972, Heating and Ionization of HI Regions, Annu. Rev. Astron. Astrophys., 10, 375

Draine, B. T. 2011, Physics of the Interstellar and Intergalactic Medium (Princeton University Press)

Dwarkadas, V. V. 2005, The Evolution of Supernovae in Circumstellar Wind-Blown Bubbles. I. Introduction and One-Dimensional Calculations, ApJ, 630, 892

Dwarkadas, V. V. 2007, The Evolution of Supernovae in Circumstellar Wind Bubbles. II. Case of a Wolf-Rayet Star, ApJ, 667, 226

Dyson, J. & Williams, D. 1997, The physics of the interstellar medium (Bristol: Institute of Physics Publishing, 1997.)

Engelbrecht, N. E. & Burger, R. A. 2013, An Ab Initio Model for Cosmic-ray Modulation, ApJ, 772, 46

Engelbrecht, N. E. & Burger, R. A. 2015, Sensitivity of Cosmic-Ray Proton Spectra to the Low-wavenumber Behavior of the 2D Turbulence Power Spectrum, ApJ, 814, 152

Fadeyev, Y. A. & Gillet, D. 2000, The structure of radiative shock waves. II. The multilevel hydrogen atom, Astron. Astrophys., 354, 349

Fahr, H. J., Kausch, T., & Scherer, H. 2000, A 5-fluid hydrodynamic approach to model the solar system-interstellar medium interaction, Astron. Astrophys., 357, 268

Fahr, H. J. & Neutsch, W. 1983, Pressure distribution at the inner boundary of an astropause caused by a compressible stellar wind, Astron. Astrophys., 118, 57

Falle, S. A. E. G. 1975a, A numerical calculation of the effect of stellar winds on the interstellar medium, Astron. Astrophys., 43, 323

Falle, S. A. E. G. 1975b, Numerical calculation of thin shell formation in supernova remnants, M.N.R.A.S, 172, 55

Falle, S. A. E. G. 1981, Catastrophic cooling in supernova remnants, M.N.R.A.S, 195, 1011

Ferreira, S. E. S. 2005, The transport of galactic and jovian cosmic ray electrons in the heliosphere, Advances in Space Research, 35, 586

Ferreira, S. E. S. & de Jager, O. C. 2008, Supernova remnant evolution in uniform and non-uniform media, Astron. Astrophys., 478, 17

Ferreira, S. E. S. & Potgieter, M. S. 2004, Galactic cosmic rays in the heliosphere, Advances in Space Research, 34, 115

Ferreira, S. E. S. & Scherer, K. 2004, Modulation of Cosmic-Ray Electrons in the Outer Heliosphere, ApJ, 616, 1215

Ferreira, S. E. S. & Scherer, K. 2006, Time Evolution of Galactic and Anomalous Cosmic-Ray Spectra in a Dynamic Heliosphere, ApJ, 642, 1256

Field, G. B. 1965, Thermal Instability., ApJ, 142, 531

Fisk, L. A., Kozlovsky, B., & Ramaty, R. 1974, An Interpretation of the Observed Oxygen and Nitrogen Enhancements in Low-Energy Cosmic Rays, ApJL, 190, L35

Florinski, V., Ferreira, S. E. S., & Pogorelov, N. V. 2013, Galactic Cosmic Rays in the Outer Heliosphere: Theory and Models, Space Sci. Rev., 176, 147

Florinski, V. & Jokipii, J. R. 2003, Cosmic-Ray Spectra at Spherical Termination Shocks, ApJ, 591, 454

Forbush, S. E. 1946, Three Unusual Cosmic-Ray Increases Possibly Due to Charged Particles from the Sun, Physical Review, 70, 771

Franco, J., Tenorio-Tagle, G., Bodenheimer, P., & Rozyczka, M. 1991, Evolution of supernova remnants inside preexisting wind-driven cavities, Publ. Astron. Soc. Pac., 103, 803

Frank, A., Noriega-Crespo, A., & Balick, B. 1992, Hydrodynamic cooling effects in ionized stellar winds, Astron. J., 104, 841

Gaetz, T. J. & Salpeter, E. E. 1983, Line radiation from a hot, optically thin plasma - Collision strengths and emissivities, ApJs, 52, 155

Gardiner, C. W. 2004, Handbook of stochastic methods. for physics, chemistry and the natural sciences, Springer Series in synergetics (Springer)

Gil, A. & Alania, M. V. 2016, Energy Spectrum of the Recurrent Variation of Galactic Cosmic Rays During the Solar Minimum of Cycles 23/24, Sol. Phys., 291, 1877

Gnat, O. & Sternberg, A. 2007, Time-dependent Ionization in Radiatively Cooling Gas, ApJS, 168, 213

Gronenschild, E. H. B. M. & Mewe, R. 1978, Calculated X-radiation from optically thin plasmas. III - Abundance effects on continuum emission, Astron Astrophys Suppl, 32, 283

Haid, S., Walch, S., Naab, T., Seifried, D., Mackey, J., & Gatto, A. 2016, Supernova blast waves in wind-blown bubbles, turbulent, and power-law ambient media, M.N.R.A.S, 460, 2962

Heber, B., Potgieter, M. S., Ferreira, S. E. S., Dalla, S., Kunow, H., Müller-Mellin, R., Wibberenz, G., Paizis, C., Sarri, G., Marsden, R. G., McKibben, R. B., & Zhang, M. 2007, An overview of Jovian electrons during the distant Ulysses Jupiter flyby, Planet. Space Sci., 55, 1

Henderson, L., Jia-Huan, M., Akira, S., & Kazuyoshi, T. 1990, Refraction of a shock wave at an air-water interface, Fluid Dynamics Research, 5, 337

Holzer, T. E. 1972, Interaction of the solar wind with the neutral component of the interstellar gas., Journal of Geophysical Research, 77, 5407

Holzer, T. E. & Axford, W. I. 1970, The Theory of Stellar Winds and Related Flows, Annual review of Astronomy and Astrophysics, 8, 31

Imamura, J. N. 1985, On the stability properties of white dwarf radiative shocks, ApJ, 296, 128

Koo, B. C. & McKee, C. F. 1992, Dynamics of wind bubbles and superbubbles. I - Slow winds and fast winds. II - Analytic theory, ApJ, 388, 93

Kopp, A., Busching, I., Strauss, R., & Potgieter, M. 2012, A stochastic differential equation code for multidimensional Fokker-Planck type problems, Computer Physics Communications, 183, 530

Kóta, J. 2013, Theory and Modeling of Galactic Cosmic Rays: Trends and Prospects, Space Sci. Rev., 176, 391

Lamers, H. & Cassinelli, J. 1999, Introduction to Stellar Winds (Cambridge University Press)

Landau, L. & Lifshitz, E. 1984, Electrodynamics of Continuous Media, Course of theoretical physics (Butterworth-Heinemann)

Langer, S. H., Chanmugam, G., & Shaviv, G. 1981, Thermal instability in accretion flows onto degenerate stars, ApJL, 245, L23

Langner, U. W., Potgieter, M. S., & Webber, W. R. 2003, Modulation of cosmic ray protons in the heliosheath, J GEOPHYS RES-SPACE, 108, 8039

LeVeque, R. 2002, Finite Volume Methods for Hyperbolic Problems, Cambridge Texts in Applied Mathematics (Cambridge University Press)

Liepmann, H. & Roshko, A. 1957, Elements of Gasdynamics, Dover Books on Aeronautical Engineering Series (Dover Publications)

Luo, X., Potgieter, M. S., Zhang, M., Pogorelov, N. V., Feng, X., & du Toit Strauss, R. 2016, A Numerical Simulation of Cosmic Ray Modulation Near the Heliopause. II. Some Physical Insights, ApJ, 826, 182

Luo, X., Zhang, M., Potgieter, M., Feng, X., & Pogorelov, N. V. 2015, A Numerical Simulation of Cosmic-Ray Modulation Near the Heliopause, ApJ, 808, 82

Mackey, J., Langer, N., & Gvaramadze, V. V. 2013, Dynamics of H II regions around exiled O stars, M.N.R.A.S, 436, 859

Mackey, J., Langer, N., Meyer, D. M.-A., Gvaramadze, V. V., Mohamed, S., Neilson, H. R., & Mignone, A. 2014, in NIC Symposium 2014-Proceedings: 12–13 February 2014— Jülich, Germany, Forschungszentrum Jülich, 77

Mackey, J., Langer, N., Mohamed, S., Gvaramadze, V. V., Neilson, H. R., & Meyer, D. M.-A. 2014, Effects of stellar evolution and ionizing radiation on the environments of massive stars, ASTRA Proceedings, 1, 61

Manuel, R., Ferreira, S. E. S., & Potgieter, M. S. 2014, Time-Dependent Modulation of Cosmic Rays in the Heliosphere, Sol. Phys., 289, 2207

Manuel, R., Ferreira, S. E. S., & Potgieter, M. S. 2015, The Effect of a Dynamic Inner Heliosheath Thickness on Cosmic-Ray Modulation, ApJ, 799, 223

Marsden, R. G., Smith, E. J., Cooper, J. F., & Tranquille, C. 1996, ULYSSES at high heliographic latitudes: an introduction., Astron. Astrophys., 316, 279

McComas, D. J., Alexashov, D., Bzowski, M., Fahr, H., Heerikhuisen, J., Izmodenov, V., Lee, M. A., Möbius, E., Pogorelov, N., Schwadron, N. A., & Zank, G. P. 2012, The Heliosphere's Interstellar Interaction: No Bow Shock, Science, 336, 1291

McKee, C. F. 1974, X-Ray Emission from an Inward-Propagating Shock in Young Supernova Remnants, ApJ, 188, 335

McKee, C. F. & Truelove, J. K. 1995, Explosions in the interstellar medium., Phys. Rep, 256, 157

Mellema, G. & Lundqvist, P. 2002, Stellar wind bubbles around WR and [WR] stars, Astron. Astrophys., 394, 901

Mignone, A. 2005, The Dynamics of Radiative Shock Waves: Linear and Nonlinear Evolution, ApJ, 626, 373

Moraal, H. 2013, Cosmic-Ray Modulation Equations, Space Sci. Rev., 176, 299

Moraal, H. 2014, Cosmic rays in the heliosphere: Observations, Astroparticle Physics, 53, 175

Moskalenko, I. V., Strong, A. W., Ormes, J. F., & Potgieter, M. S. 2002, Secondary Antiprotons and Propagation of Cosmic Rays in the Galaxy and Heliosphere, ApJ, 565, 280

Nickeler, D. H., Goedbloed, J. P., & Fahr, H. J. 2006, Stationary field-aligned MHD flows at astropauses and in astrotails. Principles of a counterflow configuration between a stellar wind and its interstellar medium wind, Astron. Astrophys., 454, 797

Opher, M., Drake, J. F., Swisdak, M., Schoeffler, K. M., Richardson, J. D., Decker, R. B., & Toth, G. 2011, Is the Magnetic Field in the Heliosheath Laminar or a Turbulent Sea of Bubbles?, ApJ, 734, 7

Opher, M., Drake, J. F., Zieger, B., & Gombosi, T. I. 2015, Magnetized Jets Driven By the Sun: the Structure of the Heliosphere Revisited, ApJL, 800, L28

Ostriker, J. P. & McKee, C. F. 1988, Astrophysical blastwaves, Reviews of Modern Physics, 60, 1

Parker, E. N. 1958, Dynamics of the Interplanetary Gas and Magnetic Fields., ApJ, 128, 664

Parker, E. N. 1961, The Stellar-Wind Regions., ApJ, 134, 20

Parker, E. N. 1965, The passage of energetic charged particles through interplanetary space, planss, 13, 9

Pauls, H. L. & Zank, G. P. 1996, Interaction of a nonuniform solar wind with the local interstellar medium, Journal of Geophysical Research, 101, 17081

Pei, C., Bieber, J. W., Burger, R. A., & Clem, J. 2010, A general time-dependent stochastic method for solving Parker's transport equation in spherical coordinates, Journal of Geophysical Research (Space Physics), 115, A12107

Pen, U. L., Arras, P., & Wong, S. 2003, A Free, Fast, Simple, and Efficient Total Variation Diminishing Magnetohydrodynamic Code, ApJS, 149, 447

Pérez-Rendón, B., García-Segura, G., & Langer, N. 2009, Supernova progenitor stars in the initial range of 23 to 33 solar masses and their relation with the SNR Cassiopeia A, Astron. Astrophys., 506, 1249

Pogorelov, N. V., Bedford, M. C., Kryukov, I. A., & Zank, G. P. 2016, in Journal of Physics Conference Series, Vol. 767, Journal of Physics Conference Series, 012020

Pogorelov, N. V., Heerikhuisen, J., & Zank, G. P. 2008, Probing Heliospheric Asymmetries with an MHD-Kinetic model, ApJL, 675, L41

Pogorelov, N. V., Heerikhuisen, J., Zank, G. P., Mitchell, J. J., & Cairns, I. H. 2009a, Heliospheric asymmetries due to the action of the interstellar magnetic field, Advances in Space Research, 44, 1337

Pogorelov, N. V., Heerikhuisen, J., Zank, G. P., Mitchell, J. J., & Cairns, I. H. 2009b, Heliospheric asymmetries due to the action of the interstellar magnetic field, Advances in Space Research, 44, 1337

Potgieter, M. 2013, Solar Modulation of Cosmic Rays, Living Reviews in Solar Physics, 10

Potgieter, M. S. 1998, The Modulation of Galactic Cosmic Rays in the Heliosphere: Theory and Models, Space Sci. Rev., 83, 147

Povich, M. S. 2012, in Frank N. Bash Symposium 2011: New Horizons in Astronomy

Preusse, S., Kopp, A., Buchner, J., & Motschmann, U. 2007, MHD simulation scenarios of the stellar wind interaction with Hot Jupiter magnetospheres, Planetary and Space Science, 55, 589

Przybilla, N., Fossati, L., Hubrig, S., Nieva, M. F., Järvinen, S. P., Castro, N., Schöller, M., Ilyin, I., Butler, K., Schneider, F. R. N., Oskinova, L. M., Morel, T., Langer, N., de Koter, A., & BOB Collaboration. 2016, B fields in OB stars (BOB): Detection of a magnetic field in the He-strong star CPD -57^0 3509, Astron. Astrophys., 587, A7

Raath, J. L., Potgieter, M. S., Strauss, R. D., & Kopp, A. 2016, The effects of magnetic field modifications on the solar modulation of cosmic rays with a SDE-based model, Advances in Space Research, 57, 1965

Richardson, J. D., Kasper, J. C., Wang, C., Belcher, J. W., & Lazarus, A. J. 2008, Cool heliosheath plasma and deceleration of the upstream solar wind at the termination shock, Nature, 454, 63

Richardson, J. D. & Smith, C. W. 2003, The radial temperature profile of the solar wind, Geophys. Res. Lett., 30, 10

Scherer, K. & Fahr, H. J. 2003, Solar cycle induced variations of the outer heliospheric structures, Geophys. Res. Lett., 30, 1

Scherer, K. & Ferreira, S. E. S. 2005, A heliospheric hybrid model: hydrodynamic plasma flow and kinetic cosmic ray transport, Astrophysics and Space Sciences Transactions, 1, 17

Scherer, K., Fichtner, H., Kleimann, J., Wiengarten, T., Bomans, D. J., & Weis, K. 2016, Shock structures of astrospheres, Astron. Astrophys., 586, A111

Scherer, K., van der Schyff, A., Bomans, D. J., Ferreira, S. E. S., Fichtner, H., Kleimann, J., Strauss, R. D., Weis, K., Wiengarten, T., & Wodzinski, T. 2015, Cosmic rays in astrospheres, Astron. Astrophys., 576, A97

Schure, K. M., Kosenko, D., Kaastra, J. S., Keppens, R., & Vink, J. 2009, A new radiative cooling curve based on an up-to-date plasma emission code, Astron. Astrophys., 508, 751

Schwarz, J., McCray, R., & Stein, R. F. 1972, Formation of Clouds in a Cooling Interstellar Medium, ApJ, 175, 673

Sedov, L. I. 1977, Similarity methods and dimensional analysis in mechanics (8th revised edition), Moscow Izdatel Nauka

Shepherd, D. 2005, in IAU Symposium, Vol. 227, Massive Star Birth: A Crossroads of Astrophysics, ed. R. Cesaroni, M. Felli, E. Churchwell, & M. Walmsley, 237

Siewert, M., Pohl, M., & Schlickeiser, R. 2004, The impact of thermal gas in AGN jets on the low-frequency emission, Astron. Astrophys., 425, 405

Simpson, J. A., Hamilton, D., Lentz, G., McKibben, R. B., Mogro-Campero, A., Perkins, M., Pyle, K. R., Tuzzolino, A. J., & O'Gallagher, J. J. 1974, Protons and Electrons in Jupiter's Magnetic Field: Results from the University of Chicago Experiment on Pioneer 10, Science, 183, 306

Stevens, I. R., Blondin, J. M., & Pollock, A. M. T. 1992, Colliding winds from early-type stars in binary systems, ApJ, 386, 265

Strauss, R. D. & Potgieter, M. S. 2014, Where does the heliospheric modulation of galactic cosmic rays start?, Advances in Space Research, 53, 1015

Strauss, R. D., Potgieter, M. S., Büsching, I., & Kopp, A. 2011a, Modeling the Modulation of Galactic and Jovian Electrons by Stochastic Processes, ApJ, 735, 83

Strauss, R. D., Potgieter, M. S., Ferreira, S. E. S., Fichtner, H., & Scherer, K. 2013, Cosmic Ray Modulation Beyond the Heliopause: A Hybrid Modeling Approach, ApJL, 765, L18

Strauss, R. D., Potgieter, M. S., Kopp, A., & Busching, I. 2011b, On the propagation times and energy losses of cosmic rays in the heliosphere, Journal of Geophysical Research (Space Physics), 116, 12105

Strickland, R. & Blondin, J. M. 1995, Numerical Analysis of the Dynamic Stability of Radiative Shocks, ApJ, 449, 727

Sutherland, R. S., Bicknell, G. V., & Dopita, M. A. 2003, The Numerical Simulation of Radiative Shocks. II. Thermal Instabilities in Two-dimensional Models, ApJ, 591, 238

Sutherland, R. S. & Dopita, M. A. 1993, Cooling functions for low-density astrophysical plasmas, ApJS, 88, 253

Suzuki, T. K. 2011, Self-consistent Simulations of Alfen Wave Driven Winds from the Sun and Stars, Space Sci. Rev., 4

Tang, S. & Wang, Q. D. 2005, Supernova Blast Waves in Low-Density Hot Media: A Mechanism for Spatially Distributed Heating, ApJ, 628, 205

Tenorio-Tagle, G., Bodenheimer, P., Franco, J., & Rozyczka, M. 1990a, On the evolution of supernova remnants. I - Explosions inside pre-existing wind-driven bubbles, M.N.R.A.S, 244, 563

Tenorio-Tagle, G., Rozyczka, M., & Bodenheimer, P. 1990b, The hydrodynamics of superstructures produced by multi-supernova explosions, Astron. Astrophys., 237, 207

Tenorio-Tagle, G., Rozyczka, M., Franco, J., & Bodenheimer, P. 1991, On the evolution of supernova remnants. II - Two-dimensional calculations of explosions inside pre-existing wind-driven bubbles, M.N.R.A.S, 251, 318

Toalá, J. A., Oskinova, L. M., González-Galán, A., Guerrero, M. A., Ignace, R., & Pohl, M. 2016, X-Ray Observations of Bow Shocks around Runaway O Stars. The Case of ζ Oph and BD+$43^0$3654, ApJ, 821, 79

van der Swaluw, E., Achterberg, A., Gallant, Y. A., & Tóth, G. 2001, Pulsar wind nebulae in supernova remnants. Spherically symmetric hydrodynamical simulations, Astron. Astrophys., 380, 309

Van Marle, A. J. & Keppens, R. 2011, Radiative cooling in numerical astrophysics: The need for adaptive mesh refinement, Computers & Fluids, 42, 44

van Marle, A. J., Meliani, Z., & Marcowith, A. 2015, Shape and evolution of wind-blown bubbles of massive stars: on the effect of the interstellar magnetic field, Astron. Astrophys., 584, A49

Vidotto, A. A., Jardine, M., Opher, M., Donati, J. F., & Gombosi, T. I. 2011, Powerful winds from low-mass stars: V374 Peg, M.N.R.A.S., 412, 351

Vidotto, A. A., Opher, M., Jatenco-Pereira, V., & Gombosi, T. I. 2010, Simulations of Winds of Weak-lined T Tauri Stars. II. The Effects of a Tilted Magnetosphere and Planetary Interactions, ApJ, 720, 1262

Vos, E. E. & Potgieter, M. S. 2016, Global Gradients for Cosmic-Ray Protons in the Heliosphere During the Solar Minimum of Cycle 23/24, Sol. Phys., 291, 2181

Wallis, M. K. & Dryer, M. 1976, Sun and comets as sources in an external flow, ApJ, 205, 895

Weaver, R., McCray, R., Castor, J., Shapiro, P., & Moore, R. 1977, Interstellar bubbles. II - Structure and evolution, ApJ, 218, 377

Williams, B. J., Blair, W. P., Blondin, J. M., Borkowski, K. J., Ghavamian, P., Long, K. S., Raymond, J. C., Reynolds, S. P., Rho, J., & Winkler, P. F. 2011, RCW 86: A Type Ia Supernova in a Wind-blown Bubble, ApJ, 741, 96

Woltjer, L. 1972, Supernova Remnants, Annu. Rev. Astron. Astrophys., 10, 129

Yamada, Y., Yanagita, S., & Yoshida, T. 1998, A stochastic view of the solar modulation phenomena of cosmic rays, Geophys. Res. Lett., 25, 2353

Zank, G. P. & Pauls, H. L. 1996, Modelling the Heliosphere, Space Sci. Rev., 78, 95

Zank, G. P., Pogorelov, N. V., Heerikhuisen, J., Washimi, H., Florinski, V., Borovikov, S., Kryukov, I., & Müller, H. R. 2009, Physics of the Solar Wind-Local Interstellar Medium Interaction: Role of Magnetic Fields, Space Sci. Rev., 146, 295

Zel'dovich, Y. B. & Raizer, Y. P. 1967, Physics of shock waves and high-temperature hydrodynamic phenomena (New York: Academic Press, 1966/1967)

Zhang, B. T. & Li, Z. 2016, Cosmic ray loading and PeV neutrino production in blazars, ArXiv e-prints

Zhang, M. 1999, A Markov Stochastic Process Theory of Cosmic-Ray Modulation, ApJ, 513, 409